AD-757 264

Lifting Surface Theory for Statically Operating Propellers

United Aircraft Research Laboratories

prepared for

Air Force Aero Propulsion Laboratory

DECEMBER 1972

Distributed By:

NTIS

National Technical Information Service
U. S. DEPARTMENT OF COMMERCE

AFAPL-TR-72-100

LIFTING SURFACE THEORY FOR STATICALLY OPERATING PROPELLERS

JAMES C. MURRAY

FRANKLIN O. CARTA

UNITED AIRCRAFT RESEARCH LABORATORIES

EAST HARTFORD, CONNECTICUT 06108

TECHNICAL REPORT AFAPL–TR–72–100

DECEMBER 1972

AIR FORCE AERO PROPULSION LABORATORY

WRIGHT–PATTERSON AIR FORCE BASE, OHIO 45433

NOTICE

When Government drawings, specifications, or other data are used for any purpose other than in connection with a definitely related Government procurement operation, the United States Government thereby incurs no responsibility nor any obligation whatsoever; and the fact that the government may have formulated, furnished, or in any way supplied the said drawings, specifications, or other data, is not to be regarded by implication or otherwise as in any manner licensing the holder or any other person or corporation, or conveying any rights or permission to manufacture, use, or sell any patented invention that may in any way be related thereto.

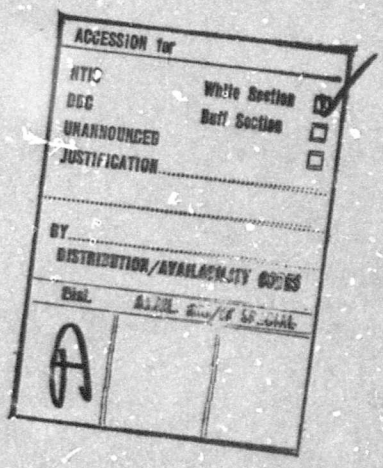

Copies of this report should not be returned unless return is required by security considerations, contractual obligations, or notice on a specific document.

LIFTING SURFACE THEORY FOR STATICALLY OPERATING PROPELLERS

JAMES C. MURRAY

FRANKLIN O. CARTA

UNITED AIRCRAFT RESEARCH LABORATORIES

EAST HARTFORD, CONNECTICUT 06108

TECHNICAL REPORT AFAPL–TR–72–100

DECEMBER 1972

AIR FORCE AERO PROPULSION LABORATORY

WRIGHT–PATTERSON AIR FORCE BASE, OHIO 45433

FOREWORD

This report was prepared by the United Aircraft Corporation Research Laboratories, East Hartford, Connecticut for the Air Force Aero Propulsion Laboratory, Aeronautical Systems Division, Wright-Patterson Air Force Base, Ohio, under Contract F33615-71-C-1430, Project number FY 1455-71-00350/3066. This report covers work conducted from May 1971 to September 1972. Captain Donald P. McErlean and Mr. Marvin Wannemacher were Project Engineers for the Aero Propulsion Laboratory.

The computer program and the accompanying users manual were prepared by Mr. Robert E. Ackerman of the United Aircraft Research Laboratories. This report was submitted by the authors in October 1972.

Publication of this report does not constitute Air Force approval of the report's findings or conclusions. It is published only for the exchange and stimulation of ideas.

Ernest C. Simpson
Director
Turbine Engine Division
Air Force Aero Propulsion Laboratory

UNCLASSIFIED

Security Classification

DOCUMENT CONTROL DATA - R & D

(Security classification of title, body of abstract and indexing annotation must be entered when the overall report is classified)

1 ORIGINATING ACTIVITY *(Corporate author)*
United Aircraft Research Laboratories
United Aircraft Corporation
East Hartford, Connecticut

2a. REPORT SECURITY CLASSIFICATION
Unclassified

2b. GROUP

3 REPORT TITLE

Lifting Surface Theory for Statically Operating Propellers

4 DESCRIPTIVE NOTES *(Type of report and inclusive dates)*
Final Report

5 AUTHOR(S) *(First name, middle initial, last name)*
James C. Murray
Franklin O. Carta

6 REPORT DATE	7a. TOTAL NO. OF PAGES	7b. NO. OF REFS
December 1972	123	25

8a. CONTRACT OR GRANT NO	9a. ORIGINATOR'S REPORT NUMBER(S)
F33615-71-C-1430	
b. PROJECT NO.	
c. FY 1455-71-00350/3066	9b. OTHER REPORT NO(S) *(Any other numbers that may be assigned this report)*
d.	AFAPL-TR-72-100

10. DISTRIBUTION STATEMENT

Approved for public release;
distribution unlimited

11. SUPPLEMENTARY NOTES	12 SPONSORING MILITARY ACTIVITY
	Air Force Aero Propulsion Laboratory Air Force Systems Command Wright Patterson Air Force Base, Ohio

13 ABSTRACT

A method was derived and a computer program formulated which utilizes a vortex-lattice lifting surface representation to model a statically operating propeller and to compute its performance. The computer program has been written to yield propeller performance characteristics for a prescribed blade geometry (the direct problem) or to yield blade camber distribution (the indirect problem). All of the results described herein were obtained for the direct problem.

Performance characteristics, including propeller thrust and torque coefficients, were computed for three propeller configurations and were compared with test data and with results computed using lifting line theory. Generally good agreement with experimental results was obtained; however, no improvement over the lifting line results for the cases examined was obtained. Direct comparisons of lifting surface effects were possible in the case of one blade on which surface pressure measurements had been made, and here good agreement between theory and experiment was achieved.

Peripheral studies were also conducted on the sensitivity of the procedure to variations in grid size, and on the ability of an extended version of the procedure to predict the noise generated by a statically operating propeller. Brief descriptions of these studies together with a completely documented User's Manual are included in this report.

DD FORM 1 NOV 65 1473

S/N 0101-807-6801

UNCLASSIFIED

Security Classification

14 KEY WORDS	LINK A		LINK B		LINK C	
	ROLE	WT	ROLE	WT	ROLE	WT
Static Propeller Performance						
Lifting Surface Theory						
Rotor Blade Aerodynamics						
Vortex-Lattice Lifting Surface Method						
Numerical Methods						

TABLE OF CONTENTS

LIST OF ILLUSTRATIONS

LIST OF ILLUSTRATIONS (Continued)

LIST OF ILLUSTRATIONS (Concluded)

LIST OF SYMBOLS

(Note: Equation, figure or table numbers refer to symbol definition or first use of symbol.)

a	Lift curve slope, Table I and Fig. 13
A	Magnitude of periodic force, lb/ft, Eq. (82)
A_m, $\bar{A}_m$	Coefficients in Fourier series, lb/ft^2, Eqs. (78), (80)
$A_{i,j}$	Area associated with pressure loading calculation, ft^2, Eq. (38)
B	Magnitude of periodic force, lb/ft, Eq. (83)
B_m, $\bar{B}_m$	Coefficients in Fourier Series, lb/ft^2, Eqs. (79), (81)
$B(x,r,\theta;\xi,\eta,\phi)$	Dimensionless normal velocity induced at (x,r,θ) by N_B unit vortices located at the points $(\xi,\eta, \delta_k+\phi)$ k = 1, 2,...N_B, Eq. (20)
c	Speed of sound, ft/sec, Eq. (71)
$c(s,r)$	Mean line ordinate, ft, Fig. 7
C_D	Drag coefficient, Eq. (44)
C_m, $\bar{C}_m$	Coefficients in Fourier series, lb/ft^2, Eqs. (89), (90)
ΔC_p	Pressure coefficient difference at a blade section, Eq. (39)
C_P	Coefficient of power, Eq. (42)
C_{QI}	Coefficient of induced torque, Eq. (41)
$C_r^{(\ell,m)}$	Geometric coefficient for radial vortex filaments, ft^{-1}, Eq. (29)
$C_s^{(\ell,m)}$	Geometric coefficient for chordwise vortex filaments, ft^{-1}, Eq. (29)
$C_t^{(m)}$	Geometric coefficient for trailing vortex filaments, ft^{-1}, Eq. (29)
C_T	Thrust coefficient, Eq. (40)
$(dn/ds)_{ML}$	Section mean line slope, Eq. (23)

LIST OF SYMBOLS (Continued)

D	Propeller diameter, ft, Eq. (40)
f_1, f_2	Pressures at a field point, lb/ft^2, Eqs. (82), (83)
F_1	Force acting on a disk element, lb/ft^2, Eq. (74)
F_2	Force acting on a disk element, lb/ft^2, Eq. (75)
$f(\eta,\phi)$	Jacobian in the transformation from s to ϕ, ft, Eq. (10)
$f' = f/R$	Dimensionless Jacobian, Eq. (19)
F/M	Figure of merit, Eq. (43)
h	Distance of vortex filament from typical field point 0, ft, Fig. 28 and Eq. (47)
h_r	Distance of radial vortex filament from field point, ft, Eq. (49)
h_s	Distance of chordwise vortex filament from field point, ft, Eq. (60)
$\vec{i}_r$	Unit vector, Eq. (55)
$\vec{i}_s$	Unit vector, Eq. (57)
k	Blade number index, Eq. (1)
k_1, k_2	Wake velocity parameters, Table IV
K	Vortex filament strength, ft^2/sec, Fig. (28) and Eq. (47)
$l(r)$	Chord length, ft, Eq. (7)
m	Harmonic index, Eq. (71)
M	Number of lattice segments in the chordwise direction, Fig. 8
n	Coordinate normal to the chordwise and radial directions, ft, Eq. (6)
N	Number of lattice segments in radial direction, Fig. 8

N_B	Number of blades, Eq. (1)
p	Pressure, lb/ft^2 or $lb/in.^2$, Eq. (8)
Δp	Pressure difference across airfoil, lb/ft^2 or $lb/in.^2$, Eq. (8)
p_T	Pressure due to thrust, lb/ft^2, Eq. (71)
p_Q	Pressure due to torque, lb/ft^2, Eq. (72)
P	Power, $= \Omega Q$
P_{1r}	Symbol defining difference in x coordinate between filament tips, ft, Eq. (52a)
P_{2r}, P_{3r}	Symbols defining difference in x coordinate between field points and filament tip, ft, Eqs. (52b), (52c)
P_{1s}	Symbol defining difference in x coordinate between filament tips, ft, Eq. (61a)
P_{2s}, P_{3s}	Symbols defining difference in x coordinate between field points and filament tip, ft, Eqs. (61b), (61c)
Q	Torque, ft-lb, Eq. (72)
Q_I	Induced torque, ft-lb, Eq. (35)
Q_P	Profile torque, ft-lb, Eq. (44)
Q_{1r}	Symbol defining difference in y coordinate between filament tips, ft, Eq. (53a)
Q_{2r}, Q_{3r}	Symbols defining difference in y coordinate between field points and filament tip, ft, Eqs. (53b), (53c)
Q_{1s}	Symbol defining difference in y coordinate between filament tips, ft, Eq. (62a)
Q_{2s}, Q_{3s}	Symbols defining difference in y coordinate between field points and filament tip, ft, Eqs. (62b), (62c)

r	Radial coordinate, ft, Eq. (2)
$r_j^{(g)}$	Radial coordinate of the point (i,j) in computation grid, ft, Eq. (33)
$r_{i,j}^{(f)}$	Radial coordinate of field point (i,j), ft, following Eq. (65)
R	Blade radius, Table I
r/R	Dimensionless radial coordinate, Table I
R_{1r}	Symbol defining difference in z coordinate between filament tips, ft, Eq. (54a)
R_{2r}, R_{3r}	Symbols defining difference in z coordinate between field points and filament tip, ft, Eqs. (54b), (54c)
R_{1s}	Symbol defining difference in z coordinate between filament tips, ft, Eq. (63a)
R_{2s}, R_{3s}	Symbols defining difference in z coordinate between field points and filament tip, ft, Eqs. (63b), (63c)
s	Coordinate in chordwise direction, ft, Eq. (6)
$\bar{s}$	Distance between (x,y,z) and (x_1,y_1,z_1), ft, Eq. (84)
$s_i^{(g)}$	s-Coordinate of the point (i,j) in computation grid, ft, Eq. (33)
$s_L(r)$	s-Coordinate of leading edge, ft, Eq. (7)
$s_T(r)$	s-Coordinate of trailing edge, ft, Eq. (7)
s/ℓ	Dimensionless S-coordinate
t	Time, sec, Eq. (4)
$t(s,r)$	Thickness form, ft, Fig. 7
T	Thrust, lb, Eq. (31)

$T(x,r,\theta;\xi,\eta,\phi)$	Dimensionless normal velocity induced at (x,r,θ) by N_B unit trailing vortices starting at $\delta_k + \phi$, $k = 1,2,\ldots N_B$, Eq. (21)
$T_{i,j}$	Thrust over area $A_{i,j}$, Eq. (39)
u_n	Total normal velocity induced by vorticity distribution, ft/sec, Eq. (22)
u_r	Radial component of the velocity induced by the distributed blade bound vorticity, ft/sec, Eq. (32)
u_s	Chordwise component of the velocity induced by the distributed blade bound vorticity, ft/sec, Eq. (32)
$u_n^{(b)}$	Normal component of velocity induced by blade bound vortex filaments at a field point, ft/sec, Eq. (66)
$u_n^{(t)}$	Total normal velocity induced by the trailing vortex system at a field point, ft/sec, Eq. (67)
$u_r^{(b)}$	Radial component of velocity induced by blade bound vortex filaments at a field point, ft/sec, Eq.(65)
$u_x^{(b)}$	Radial component of velocity induced by blade bound vortex filaments at a field point, ft/sec, Eq. (64)
$u_y^{(b)}$	y component of velocity induced by blade bound vortex filaments at a field point, ft/sec, Eq. (64)
$u_z^{(b)}$	z component of velocity induced by blade bound vortex filaments at a field point, ft/sec, Eq. (64)
$u_\theta^{(b)}$	Azimuthal component of velocity induced by blade bound vortex filaments at a field point, ft/sec, Eq. (65)
$u_n^{(rb)}$	Total normal velocity induced by radial bound vorticity at a field point, ft/sec, Eq. (19)
$u_n^{(sb)}$	Total normal velocity induced at a field point by chordwise bound vorticity, ft/sec, Eq. (21)
$u_{kn}^{(rb)}$	Normal velocity induced at a field point by the radial bound vorticity located on the kth blade, ft/sec, Eq. (20)

$u_{kx}^{(rb)}$	Axial component of velocity induced at a field point by the radial vortex filaments located on the kth blade, ft/sec, Eq. (56)
$u_{ky}^{(rb)}$	y-component of velocity induced at a field point by the radial vortex filaments located on the kth blade, ft/sec, Eq. (56)
$u_{kz}^{(rb)}$	z-component of velocity induced at a field point by the radial vortex filaments located on the kth blade, ft/sec, Eq. (56)
$u_{kx}^{(sb)}$	Axial component of velocity induced at a field point by the chordwise vortex filaments location on the kth blade, ft/sec, Eq. (57)
$u_{ky}^{(sb)}$	y-component of velocity induced at a field point by the chordwise vortex filaments located on the kth blade, ft/sec, Eq. (57)
$u_{kz}^{(sb)}$	z-component of velocity induced at a field point by the chordwise vortex filaments located on the kth blade, ft/sec, Eq. (57)
v	Normal velocity, ft/sec, Eq. (47)
V	Total velocity from UARL lifting line theory, ft/sec, = $(V_A^2 + V_R^2 + V_T^2)^{\frac{1}{2}}$, Eq. (14)
V_A	Induced axial velocity from UARL lifting line program, ft/sec, Eq. (3)
V_R	Induced radial velocity from UARL lifting line program, ft/sec, Eq. (4)
V_S	Total velocity in chordwise direction from UARL lifting line theory, ft/sec, = $(V_A^2 + V_T^2)^{\frac{1}{2}}$, Eq. (8)
V_T	Total circumferential velocity from UARL lifting line program, ft/sec, Eq. (3)
x	Coordinate in direction of propeller axis, ft, Fig. 5(a)
$x_{i,j}^{(f)}$	x-coordinate of field point (i,j), ft, Fig. 29 and Eq. (48)

$x_{\ell,m,k}^{(g)}$	x-coordinate of computation grid point (ℓ,m,k), ft, Fig. 29 and Eq. (48)
y	Coordinate passing through tip of first blade, ft, Eq. (2)
$y_{i,j}^{(f)}$	y-coordinate of field point (i,j), Fig. 29
$y_{\ell,m,k}^{(g)}$	y-coordinate of computation grid point (ℓ,m,k), Fig. 29
z	Axial coordinate, ft, Eq. (2)
$z_{i,j}^{(f)}$	z-coordinate of field point (i,j), Fig. 29
$z_{\ell,m,k}^{(g)}$	z-coordinate of computation grid point (ℓ,m,k), Fig. 29
$\alpha(r)$	Blade pitch angle, Fig. 7 and Eq. (29)
$\alpha_i(r)$	Angle of incidence, Fig. 7 and Eq. (23)
α_{OL}	Angle of zero lift, Eq. (45)
α_{75}	Collective pitch at 3/4 radius, Eq. (45)
$\Delta\alpha$	Blade pitch increment, Eq. (45)
β	Angle of reference surfaces, Eq. (6)
β_j	Value of β at $r = r_{i,j}^{(f)}$, Eq. (66)
γ	Strength of radial bound vorticity, ft/sec, Eq. (8)
γ_s	Srength of chordwise bound vorticity, ft/sec, Eq. (11)
γ_T	Strength of trailing vortices, ft/sec, Eq. (13)
$\Gamma(\eta)$	Total bound circulation calculated from radial bound vorticity, ft^2/sec, Eq. (9)
Γ_r	Radial vortex filament strength, ft^2/sec, Fig. 8
Γ_s	Chordwise vortex filament strength, ft^2/sec, Fig. 8
Γ_t	Trailing vortex filament strength, ft^2/sec, Fig. 8
$\Gamma_{r_{i,j-1}}^{i,j}$	Radial vortex filament strength between points (i,j-1) and (i,j) of vortex lattice, ft^2/sec, Fig. 9 and Eq. (25)

$\Gamma_{S_{i-1,j}}^{i,j}$	Chordwise vortex filament strength between points (i-1,j) and (i,j) of vortex lattice, ft^2/sec, Fig. 9 and Eq. (25)
δ	Angle that mean line makes with the chord in the (s,n) plane, Fig. 7 and Eq. (29)
$\delta(\ )$	Dirac delta function, Eq. (33)
δ_k	Angular coordinate of kth blade tip, Eq. (1)
η	Radial coordinate, ft, Eq. (9)
$\eta' = \eta/R$	Dimensionless radial coordinate, Eq. (19)
θ	Angular coordinate in the rotor-fixed frame of reference, Eq. (2)
$\theta_{i,j}^{(f)}$	Angular coordinate of field point (i,j), Eq. (65)
$\theta_L(r)$	Angular coordinate of the leading edge, Eq. (11)
$\theta_T(r)$	Angular coordinate of the trailing edge, Eq. (11)
θ_1, θ_2	Angles associated with vortex filaments, Fig. 28 and Eq. (47)
θ_{1r}	Angle defined by Eq. (50)
θ_{2r}	Angle defined by Eq. (51)
θ_{1s}	Angle defined by Eq. (58)
θ_{2s}	Angle defined by Eq. (59)
ξ	Dimensionless coordinate in direction of propeller axis, Eq. (19)
ρ	Fluid density, lb sec^2/ft^4, Eq. (8)
σ	Distance between blade and external field point, ft, Eq. (71)
τ_1	Time interval, sec, Eq. (73)
τ_2	Eclipse time, sec, $= 2\pi/N_B\Omega$, following Eq. (73)

ϕ	Angular coordinate, Eq. (10)
Ω	Propeller blade angular velocity, sec^{-1}, Eq. (40)

Subscripts

A	Axial
i	Incidence, also first index for a point in vortex lattice
j	Second index for a point in vortex lattice
k	Blade number index
k_n	kth blade
L	Leading or lower
ML	Mean line
n	Normal
r	Radial
$r_{i,j}$	Radial (at point (i,j) of vortex lattice)
R	Radial (lifting line theory)
s	Chordwise
$s_{i,j}$	Chordwise (at point (i,j) of vortex lattice)
t	Trailing
T	Trailing or circumferential
u	Upper

Superscripts

i	First index for a point in vortex lattice
j	Second index for a point in vortex lattice

rb	Radial bound
sb	Chordwise bound
t	Wake

Special Symbols

$\neq\!\!\!\int\!\!\!\int$	Integral sign denoting Mangler type singular integral, Eq. (19)

SECTION I

INTRODUCTION

The prediction of the detailed aerodynamic performance of propeller and helicopter blades is a more difficult problem than the prediction of the aerodynamic performance of a fixed wing. In the latter the wake trails back from the wing in a relatively straight path to downstream infinity and its effect diminishes rapidly with distance. However, in the case of a propeller or helicopter rotor the blades pass directly over their own wakes and those of other blades as they rotate. Furthermore, a given vortex element has a longer residence time in the immediate vicinity of the rotor plane compared with that of a fixed wing vortex element. Hence, we would expect the blade-wake interaction to be stronger in the rotor than in the fixed wing case. This type of blade-wake interaction is even more evident when a propeller (or rotor) operates in the static regime. The absence of a free-stream velocity requires that the wake geometry be determined from the induced velocity field of the propeller and its wake system. As a result of the fact that there is no free-stream velocity, greater wake distortion will occur and the wake vorticity will be located in the immediate vicinity of the blades. Therefore any rigorous analysis of the static performance problem must fully account for wake distortion and the proximity of the wake vortex elements to the rotating blade surfaces.

Existing classical performance methods (Refs. 1 and 2), when applied to the static case, have been shown to be incapable of predicting accurately the performance of propellers which have high solidities, high blade loadings and high tip Mach numbers (see Fig. 1, taken from Ref. 3). The main assumptions in these theories when applied to the static case are:

1. The wake is an undeformed helicoidal surface defined by the blade rotational velocity and average velocity through the disk, and

2. The blades can be represented by lifting lines.

The first assumption is not valid for the static case because the wake deforms and contracts rapidly in the vicinity of the rotating blades as discussed above. Further, evidence of wake contraction (particularly in the tip region) for a statically operating propeller can be seen from Fig. 2 which was taken from Ref. 4. This contraction was shown to alter significantly the wake-induced velocities and therefore the blade loading (see Fig. 3, taken from Ref. 3). To achieve a major improvement in the state of the art it was necessary to develop a more realistic representation of the wake. Analytical methods to provide this improved wake representation were recently developed at UARL (Ref. 5). These methods were based on a lifting line representation of the rotating blades and a contracted wake geometry. Although

significantly improved performance prediction methods resulted from these lifting line-contracted wake analyses, the effects of distributed vorticity were not accounted for.

In fixed wing theory a major improvement in the prediction of the aerodynamics occurred with the advent of lifting surface theory in which the effects of a chordwise and spanwise vorticity distribution were incorporated (Ref. 6). Comparable developments in rotating blade theory have not progressed as far as the theories for fixed wings, particularly for the case of static operation. The lifting surface theories developed recently for propellers having nonzero advance ratio may be classified into two categories:

1. Continuous Vortex Sheet Representation - In this case the blade is represented by a system of continuous vortex sheets and the velocity field is computed using Biot-Savart law (e.g., Refs. 7 and 8).

2. Lattice Representation - Here the blade is represented by a set of concentrated radial and helical vortex lines. This method has been developed by Strecheletzky (Ref. 9) and Guilloton (Ref. 10). Kerwin (Ref. 11) has developed the theory further and investigated how the accuracy of the results depended on the lattice spacing chosen for the computation. However, none of these approaches as described in these references is valid for the static operation of a propeller because of the assumption of an uncontracted and undistorted helicoidal wake.

In the static case the lifting surface method has not been applied and existing theories for performance prediction are based on the lifting line assumptions (e.g., Ref. 12). Jones (Ref. 13) and Peracchio (Ref. 14) reviewed conditions under which a lifting surface such as a blade may be approximated by a lifting line. These are: (1) the existence of flow substantially parallel to the blade chord and (2) the constancy of wake-induced velocities over the blade chord. The presence in a contracted wake of strong vortices immediately below the blades strongly suggests that both of these assumptions are violated. In the tip region it is expected that large radial velocities will be induced due to the presence of tip vortices. In Fig. 4 (taken from Ref. 15) a plot of wake-induced axial velocity versus azimuthal angle for a tip station of a statically operating propeller is shown for two typical circulation distributions (see also Ref. 16 for further details). The axial velocity is seen to vary rapidly over distances on the order of chord length.

It appears, then, that there exists significant evidence suggesting the need for a lifting surface theory for predicting the flow field and performance of a statically operating rotor or propeller. The objectives of such a theory are to investigate the possibility of improving the existing performance prediction methods and to study and compare the effects of three-dimensional tip

flow with existing lifting line theories and experimental data. The present formulation is based on an extension into the static regime of the lifting surface theory of Kerwin (Refs. 11 and 17).

SECTION II

DERIVATION OF BASIC EQUATIONS

1. GEOMETRICAL CONSIDERATIONS - DEFINITION OF COORDINATE SYSTEMS AND BLADE GEOMETRY

In developing the lifting surface formulation for statically operating propellers it is necessary to introduce several coordinate systems for the purpose of accurately defining the blade and vortex geometry. The basic reference system is a Cartesian coordinate system which is fixed on the propeller (see Fig. 5(a)). The x-axis is coincident with the axis of revolution and positive distances are measured in the direction of the wake. The y-axis is chosen to lie in the plane of the propeller along a radial line passing through the tip of one blade, while the z-axis is another radial line, also in the plane of the rotor disc, which completes the right-hand system. (The z-axis need not intersect any portion of any blade whereas the y-axis is fixed in one of the blades.) A cylindrical coordinate system (x,r,θ) is also defined where the x-axis, as before, is the axis of revolution. The radial coordinate is denoted by r, and the angular coordinate (measured clockwise starting from the y-axis while facing aft) is denoted by θ.

In order to relate corresponding points on each of the N_B blades, we define δ_k as the θ-coordinate of the point at the tip of the kth blade (see Fig. 5(b)). Assuming that the blades are symmetrically oriented we have

$$\delta_k = \frac{2\pi}{N_B}(k-1);\ k = 1,2,\ldots,N_B \tag{1}$$

The relations between the coordinate systems are

$$\begin{aligned} y &= r\cos\theta \\ z &= r\sin\theta \\ r &= \sqrt{y^2+z^2} \\ \theta &= \tan^{-1}(z/y) \end{aligned} \tag{2}$$

We consider a basic flow field which is defined by the UARL lifting-line theory (Ref. 12) for statically operating rotors. This flow field is prescribed and is composed of axial, radial and circumferential velocity components V_A, V_R and V_T. The circumferential component V_T will include the rotational blade velocity Ωr where Ω is the propeller angular velocity. We define an angle β with respect to the prescribed flow field by the relation

$$\tan\beta = V_A / V_T \tag{3}$$

This angle will be used below in connection with a system of reference surfaces.

Before the blade surfaces can be properly defined it is necessary to define a set of reference surfaces. These reference surfaces are defined by using the prescribed flow field obtained from the UARL lifting-line program (Ref. 12) for statically operating rotors. The fluid velocity in the prescribed flow field at any point has the components V_A, V_R and V_T. The kth reference surface will be chosen to pass through the kth radial line oriented at an angle δ_k (see Fig. 5(b)). This reference surface will coincide with the stream surface passing through the kth radial line which has a local tangential velocity at every point equal to the vector sum of V_A, V_R, and V_T. The system of equations governing the coordinates of the reference surface will have the form

$$\begin{aligned} \frac{dx}{dt} &= V_A \\ r\frac{d\theta}{dt} &= V_T \\ \frac{dr}{dt} &= V_R \end{aligned} \tag{4}$$

subject to the conditions

$$\theta = \delta_k \tag{5}$$

when $x = 0$; $\quad 0 \le r \le 1$; $\quad k = 1,2,\ldots,N_B$

The kth propeller blade will be assumed to be approximately coincident with the kth reference surface in that part of the kth reference surface which forms the projection of the kth blade planform. This is analogous to linearized fixed wing theory in which the corresponding reference surface is a horizontal plane and all points of the wing are in the proximity of this plane.

An orthogonal curvilinear coordinate system (s,n,r) is defined on each of the N_B reference surfaces (see Figs. 5 and 6). The s coordinate is formed by the intersection of an axial cylinder and the particular kth surface. The r coordinate is radial as before and the n coordinate is perpendicular to both r and s. The s coordinate is directed in such a way that it has a positive axial component. From Fig. 6 the relationship between the (s,n,r) and (x,r,θ) systems is given by

$$ds = dx \sin\beta + rd\theta \cos\beta$$
$$dn = dx \cos\beta - rd\theta \sin\beta \qquad (6)$$

In order to facilitate the description of the blade sections it will be assumed that the blade surface has a normal at every point that is almost parallel to the (s,n) plane through that point. The blade outline and shape of the blade sections can now be defined in the (s,n,r) system (Fig. 7). The s coordinates of the leading and trailing edges are $S_L(r)$ and $S_T(r)$, respectively, at a blade section which is at a distance r from the x-axis. The angular coordinates are designated by $\theta_L(r)$ and $\theta_T(r)$ and the chord length is given by

$$l(r) = S_T(r) - S_L(r) \qquad (7)$$

On the assumption of a thin blade, the blade section can be decomposed into a symmetrical thickness form t(s,r), a mean line ordinate c(s,r) and an angle of incidence $\alpha_i(r)$ as shown in Fig. 7. In this investigation we set $t(s,r) = 0$ as thickness effects are not being included in the formulation.

2. DISTRIBUTION OF BOUND AND TRAILING VORTICES

The assumption of thin blades implies small values in the perturbation velocities so the usual linearized approximations of thin wing theory are applicable. Consistent with the linearized theory the pressure loading on the blades can be represented by a distribution of bound vortices not on the blade surface itself but on its projection on the corresponding reference surface. The radial strength of the bound vortex sheet per unit of length along a line parallel to the radial direction is denoted by γ and the strength of the bound vorticity in the chordwise direction is denoted by γ_s. (We remark here that in this part of the formulation we use the concept of a continuously

distributed vorticity. Later, in the theoretical numerical model we replace the distributed vorticity by a discrete set of vortex filaments.) The pressure difference across a blade surface, correct to first order in small quantities, is given in Ref.17 by

$$\Delta p = \rho V_S \gamma \tag{8}$$

where $V_S = \sqrt{V_A^2 + V_T^2}$ and ρ denotes the fluid density. The total circulation around a blade at radius η due to radially oriented vorticity is given by

$$\Gamma(\eta) = \int_{S_L(\eta)}^{S_T(\eta)} \gamma(\eta, s)\, ds \tag{9}$$

The integration variable in Eq. (9) can be transformed to an azimuthal integration variable ϕ so that Eq. (9) becomes

$$\Gamma(\eta) = \int_{S_L(\eta)}^{S_T(\eta)} \gamma(\eta,\phi) f(\eta,\phi)\, d\phi \tag{10}$$

where the function $f(\eta,\phi)$ is the Jacobian of the transformation from s to ϕ.

By virtue of the finite dimensions of a given blade as well as a radial and chordwise variation in velocity over the blade the radial and chordwise components of vorticity must vary subject to a continuity relationship over the given blade surface. In addition, conservation of vorticity demands that there must appear a wake in the form of a vortex sheet. The continuity equations expressing the conservation of vorticity have been derived in Ref. 18 and assume the form:

$$\frac{\partial}{\partial \eta}\left[\gamma(\eta,\phi) f(\eta,\phi)\right] + \frac{\partial \gamma_s}{\partial \phi} = 0 \tag{11}$$

$$\theta_L(\eta) < \phi < \theta_T(\eta)$$

$$\gamma_s(\eta,\theta_L) = \gamma(\eta,\theta_L) f(\eta,\theta_L) \frac{\partial \theta_L}{\partial \eta} \tag{12}$$

$$\gamma_T(\eta,\theta_T) = \frac{V\left[\gamma_s(\eta,\theta_T) - \gamma(\eta,\theta_T) f(\eta,\theta_T) \frac{\partial \theta_T}{\partial \eta}\right]}{V_S - V_R f(\eta,\theta_T) \frac{\partial \theta_T}{\partial \eta}} \tag{13}$$

where $\gamma_T(\eta,\theta_T)$ denotes the strength of a trailing vortex which begins at (η, θ_T) on the trailing edge and V is given by

$$V^2 = V_A^2 + V_R^2 + V_T^2 \tag{14}$$

The relation between γ and γ_s expressed in Eq. (11) is a continuity equation which is valid at interior points of the blade whereas Eqs. (12) and (13) are valid at the leading and trailing edges, respectively. A further relation between γ and γ_s which is valid at all points except the trailing edge can be found by integrating Eq. (11) and using Eq. (12). This relation has the form

$$\gamma_s(\eta,\phi) = \gamma(\eta,\theta_L) f(\eta,\theta_L) \frac{\partial \theta_L}{\partial \eta} - \int_{\theta_L(\eta)}^{\phi} \frac{\partial}{\partial \eta} \left[\gamma(\eta,\phi) f(\eta,\phi)\right] d\phi \tag{15}$$

Some simplification of Eq. (13) is afforded if it is borne in mind that $V_R \ll V_S$ and $f(\eta,\theta_T)$ is at most of order 1. The derivative $\partial\theta_T/\partial\eta$ is small at all points of the trailing edge except in the region of the tip. Equation (13) therefore has the following simplified form almost everywhere on the trailing edge.

$$\gamma_T(\eta,\theta_T) = \gamma_s(\eta,\theta_T) - \gamma(\eta,\theta_T) f(\eta,\theta_T) \frac{\partial \theta_T}{\partial \eta} \tag{16}$$

Finally, the linearized form of the Kutta-Joukowsky condition at the trailing edge is given by

$$\Delta p\left(\eta,\theta_T\right) = 0 \tag{17}$$

or

$$\gamma\left(\eta,\theta_T\right) = 0 \tag{18}$$

3. NORMAL VELOCITY INDUCED BY VORTICITY DISTRIBUTION

The perturbation velocity component induced by the radial bound vorticity at the point (x,r,θ) in the direction of the normal to the first reference surface is given by (Ref. 18)

$$u_n^{(rb)} = \oint\!\!\!\!\!\!\int \gamma\left(\eta,\phi\right) B\left(x,r,\theta;\xi,\eta',\phi\right) f'\left(\eta',\phi\right) d\phi\, d\eta' \tag{19}$$

where $\eta' = \eta/R, f' = f/R$, where

$$B\left(x,r,\theta;\xi,\eta',\phi\right) = \sum_{k=1}^{N_B} u_{kn}^{(rb)} \tag{20}$$

is the dimensionless normal velocity induced at (x,r,θ) by N_B unit vortices located at $(\xi, \eta', \delta_k + \phi)$, and where $u_{kn}^{(rb)}$ represents the dimensionless normal velocity induced at the point (x,r,θ) by a radial bound vortex element of unit strength located on the kth blade at the point $(\xi, \eta', \delta_k + \phi)$ for $k = 1,2,\ldots, N_B$. The integral in Eq. (19) has a singular integrand of the Mangler type as indicated by the symbol $\oint\!\!\!\!\!\!\int$ (e.g., see Ref. 19). The singularity arises when the points (x,r,θ) and $(\xi, \eta', \delta_k + \phi)$ coincide on the first blade reference surface.

In order to compute the induced effects of the chordwise bound and trailing vorticity we will make the assumption that for every chordwise bound vortex there exists a trailing vortex extending to infinity. It can then be shown (Ref. 18) that the total normal velocity induced by these two vortex

systems is given by

$$u_n^{(sb)} + u_n^{(t)} = -\oint\int_{\substack{\text{BLADE REFERENCE}\\ \text{SURFACE}}} \frac{\partial}{\partial \eta'}\left[\gamma(\eta',\phi) f'(\eta',\phi)\right] T(x,r,\theta;\xi,\eta',\phi)\, d\phi\, d\eta'$$

$$+ \oint_{\text{LEADING EDGE}} \gamma(\eta'\theta_L)\, T(x,r,\theta;\xi,\eta',\theta_L) f'(\eta',\theta_L) \frac{\partial \theta_L}{\partial \eta'}\, d\eta' \qquad (21)$$

$$- \oint_{\text{TRAILING EDGE}} \gamma(\eta',\theta_L)\, T(x,r,\theta;\xi,\eta',\theta_T) f'(\eta',\theta_T) \frac{\partial \theta_T}{\partial \eta'}\, d\eta'$$

where $u_n^{(sb)}$ denotes the contribution from the chordwise bound vorticity distribution, $T(x,r,\theta;\xi,\eta,\phi)$ is the velocity induced at (x,r,θ) by N_B unit trailing vortices starting at $\delta_k + \phi$. The total contribution from the wake and chordwise bound vorticity is denoted by $u_n^{(t)}$.

4. LIFTING SURFACE THEORY EQUATIONS

The total perturbation velocity induced normal to the first blade reference surface by the vortex system is given by

$$u_n = u_n^{(rb)} + u_n^{(sb)} + u_n^{(t)} \qquad (22)$$

To derive the fundamental integral equation of lifting surface theory we express the fact that the fluid does not penetrate the blade surface. The assumption of small perturbation velocities permits us to write this condition in the form (Ref. 20)

$$\frac{u_n - V_A \cos\beta}{V_s} = \left(\frac{dn}{ds}\right)_{ML} + \alpha_i \qquad (23)$$

where V_A is the axial velocity induced by the prescribed wake (computed using the UARL lifting line program for statically operating rotors, Ref. 12), $(dn/ds)_{ML}$ is the slope of a section mean line measured in the (s,n) coordinate

system and α_i is the incidence angle shown in Fig. 7. Since $V_A \cos\beta/V_S = \beta$ when second order terms are neglected, and $\alpha_i = \alpha - \beta$, where α is the blade angle, Eq. (23) becomes

$$\frac{u_n}{V_s} = \alpha + \left(\frac{dn}{ds}\right)_{ML} \tag{24}$$

Equation (24) together with the continuity equations and the Kutta-Joukowsky condition form the fundamental system of equations in the lifting surface analysis. The two fundamental problems of interest are the direct and indirect problems. In the direct problem the blade geometry is completely prescribed and the vorticity distribution is found. In the indirect problem a geometry is found which corresponds to a prescribed vorticity distribution. In the next section the numerical procedure for solving these problems will be discussed.

SECTION III

METHOD FOR SOLVING LIFTING SURFACE EQUATIONS

A numerical method for solving the lifting surface equations is developed by first replacing the continuous vortex system on the blades and in the wake by a system of vortex filaments as shown in Fig. 8. The circulation strength of the radial bound vortex filaments is denoted by Γ_r, and Γ_s denotes the circulation strength of the chordwise bound filaments. The strength Γ_t of the trailing vortex filaments will be determined from an appropriate continuity equation. This equation and the remaining vortex lattice theory equations are derived in the next section.

1. VORTEX LATTICE THEORY EQUATIONS

In the discrete vortex lattice model under investigation a typical lattice point on the kth blade reference surface is denoted by (i,j,k) $i = 1,2,\ldots,M+1$, $j = 1,2,\ldots,N+1$, $k = 1,2,\ldots,N_B$, where M and N denote the number of segments in the chordwise and radial directions, respectively (see Fig. 9). The vortex filament lying between (i,j-1,k) and (i,j,k) has a strength denoted by $\Gamma_{r_{i,j-1}}^{i,j}$. In a similar manner the strength of a vortex filament lying between (i-1,j,k) and (i,j,k) is denoted by $\Gamma_{s_{i-1,j}}^{i,j}$. We note that because the blades are symmetrically oriented $\Gamma_{r_{j,j-1}}^{i,j}$ and $\Gamma_{s_{i-1,j}}^{i,j}$ are independent of k. The laws of conservation of vorticity, which were expressed by Eqs. (11), (12) and (13) in the case of a continuous distribution of vorticity, must now be restated in the form

$$\Gamma_{r_{i,j}}^{i,j+1} - \Gamma_{r_{i,j-1}}^{i,j} + \Gamma_{s_{i,j}}^{i+1,j} - \Gamma_{s_{i-1,j}}^{i,j} = 0 \qquad \begin{matrix} i = 1,2,\ldots,M+1 \\ j = 1,2,\ldots,N+1 \end{matrix} \tag{25}$$

$$\Gamma_{s_{0,j}}^{i,j} = 0\,, \quad j = 1,2,\ldots,N+1 \tag{26}$$

$$\Gamma_{r_{i,j}}^{i,j+1} = 0, \qquad \begin{matrix} i = 1,2,\ldots,M+1 \\ j = N+1 \end{matrix} \tag{27}$$

$$\Gamma_{r_{i,o}}^{i,1} = 0, \quad i = 1,2,\ldots,M+1 \tag{28}$$

Equation (25) applies at all points of the lattice including boundary points. Equations (26), (27) and (28) apply at the boundary points on the leading edge, tip region, and hub, respectively. The equations express the fact that vorticity does not enter or leave through any closed curve surrounding a lattice point.

The Biot-Savart law for a straight line vortex filament has a particularly simple form and the velocity induced at a field point (which is placed at the centroid of each elemental area of the lattice, as shown in Fig. 8) due to all vortex filaments (including wake filaments) can be computed without integrating over singularities. At each field point the linearized surface condition of Eq. (24), which expresses the condition of zero through-flow over the blade surface, will now have the form

$$\sum_{\ell=1}^{M+1} \sum_{m=1}^{N} C_r^{(\ell,m)} \Gamma_{r_{\ell,m}}^{\ell,m+1} + \sum_{\ell=1}^{M} \sum_{m=1}^{N+1} C_s^{(\ell,m)} \Gamma_{s_{\ell,m}}^{\ell+1,m} + \sum_{m=1}^{N+1} C_t^{(m)} \Gamma_t^{(m)} = V_s(\alpha+\delta) \tag{29}$$

where δ is the angle that the mean line makes with the chord in the (s,n) plane (see Fig. 7). The coefficients $C_s^{(\ell,m)}$, $C_r^{(\ell,m)}$ and $C_t^{(m)}$ arise in the application of the Biot-Savart law and depend on vortex geometry only. A derivation of Eq. (29) is given in Appendix I. The total number of vortex filament strengths is (M+1)(2N+1). We have (M+1)(N+1) continuity relations of the form given in Eqs. (25), (26), (27), and (28) and MN relations of the form given in Eq. (29). We therefore need an additional N equations. These equations are furnished by restating the Kutta-Joukowsky condition in Eq. (18), which is imposed on the distributed vorticity, in an approximate form which sets the spanwise circulation equal to zero along the airfoil trailing edge,

$$\Gamma_{r_{M+1,j}}^{M+1,j+1} = 0 \quad \text{for} \quad j = 1,2,\ldots,N+1 \tag{30}$$

We now have a consistent system of equations which is suitable for the solution of the direct or indirect aerodynamic problem.

2. THE COMPUTER PROGRAM

The lifting surface theory for a statically operating propeller, formulated in the foregoing sections, was programmed for both the UNIVAC 1108 and the CDC 6600 digital computers. A flow diagram showing the required input,

sequence of major operations, and output of the program is presented in Fig. 10.

In the input part of the program the wake geometry, airfoil data, tip speed, number of blades, and speed of sound are prescribed in the same manner as that in the UARL prescribed wake hover performance computer program for helicopter rotors (Ref. 5). The appropriate input variables are described in the accompanying operator's manual (see Appendix II). In prescribing the blade twist distribution an allowance is made for non-symmetric airfoil sections. This appears in the input array of variables as a correction to the variable DTHETA which defines the pitch increment with respect to the pitch at the seventy-five percent radial position on the blade.

The blade planform and blade grid mesh size are prescribed with respect to a reference line. This reference line is equidistant from the leading and trailing edges of the blade and points on the blade (or the blade reference surface) are located in terms of their distance from the reference line. In Appendix II the input variables for specifying blade planform geometry both for continuous and discontinuous blades are listed. The parameters describing the blade grid mesh size are also listed.

In the output part of the program the local blade angle of attack distribution is printed out in the case of the indirect problem and the vortex filament strengths are printed out in the direct problem. The propeller performance and blade pressure loading are computed in the manner indicated below.

a. Thrust

For a distributed vorticity distribution having components γ and γ_s the thrust per blade is given by

$$T = \iint_{\substack{\text{BLADE REFERENCE} \\ \text{SURFACE}}} \Delta p \cos\beta \, ds \, dr \tag{31}$$

or equivalently by

$$T = \iint_{\substack{\text{BLADE REFERENCE} \\ \text{SURFACE}}} \rho\gamma \left(V_s + u_s\right) \cos\beta \, ds \, dr + \iint_{\substack{\text{BLADE REFERENCE} \\ \text{SURFACE}}} \rho\gamma_s \left(V_r + u_r\right) \cos\beta \, ds \, dr \tag{32}$$

where u_r and u_s are the radial and chordwise velocity components induced by the distributed blade bound vorticity and ρ, β, γ, γ_s, V_R and V_S are defined as before. In the discrete vortex lattice representation of the bound vorticity the components of vorticity γ and γ_s have the form

$$\gamma = \delta\left(s - s_i^{(g)}\right)\Gamma_{r_j}$$

$$\gamma_s = -\delta\left(r - r_j^{(g)}\right)\Gamma_{s_i} \tag{33}$$

where $\delta(\ )$ denotes the Dirac delta function. Using the properties of the delta function it can be shown, after some algebra, that the expression for T has the form

$$T = \rho \sum_{j=1}^{N} \sum_{i=1}^{M+1} \Gamma_{r_{i,j}}^{i,j+1} \int_{r_j^{(g)}}^{r_{j+1}^{(g)}} \left[V_s\left(r\right) + u_s\left(r, s_i^{(g)}\right) \right] \cos\beta\left(r\right) dr$$

$$-\rho \sum_{j=1}^{N+1} \sum_{i=1}^{M} \Gamma_{s_{i,j}}^{i+1,j} \cos\beta\left(r_j^{(g)}\right) \int_{s_1^{(g)}}^{s_{i+1}^{(g)}} \left[V_R\left(r_j^{(g)}\right) + u_r\left(r_j^{(g)}, s\right) \right] ds \tag{34}$$

b. Torque

The induced torque per blade is given by

$$Q_I = \iint_{\substack{\text{BLADE REFERENCE} \\ \text{SURFACE}}} r\,\Delta\rho\,\sin\beta\,ds\,dr \tag{35}$$

Again, proceeding as in the thrust computation above, we find

$$Q_I = \rho \sum_{j=1}^{N} \sum_{i=1}^{M+1} \Gamma_{r_{i,j}}^{i,j+1} \int_{r_j^{(g)}}^{r_{j+1}^{(g)}} \left[V_s\left(r\right) + u_s\left(r, s_i^{(g)}\right) \right] r\,\sin\beta\left(r\right) dr$$

$$-\rho \sum_{j=1}^{N+1} \sum_{i=1}^{M} \Gamma_{s_{i,j}}^{i+1,j}\, r_j^{(g)} \sin\beta\left(r_j^{(g)}\right) \int_{s_1^{(g)}}^{s_{i+1}^{(g)}} \left[V_R\left(r_j^{(g)}\right) + u_r\left(r_j^{(g)}, s\right) \right] ds \tag{36}$$

c. Pressure Loading

The pressure difference across the blade in coefficient form is defined as

$$\Delta C_p = \frac{p_L - p_u}{\frac{1}{2}\rho V_T^2} \tag{37}$$

where p_L is the pressure on the lower surface of the blade and p_u is the pressure on the upper surface of the blade. The quantity ΔC_p is computed by considering an interior lattice point (i,j,1) (see Fig. 11) on the first blade and an associated area $A_{i,j}$. The area $A_{i,j}$ is given by

$$A_{i,j} = \frac{1}{4}\left(r_{j+1}^{(g)} - r_{j-1}^{(g)}\right)\left(s_{i+1}^{(g)} - s_{i-1}^{(g)}\right) \tag{38}$$

The pressure loading is then found from the formula

$$\Delta C_p = \frac{T_{i,j} \sec\beta\,(r_j^{(g)})}{\frac{1}{2}\rho V_T^2 A_{i,j}} \tag{39}$$

where $T_{i,j}$ is the thrust on the area $A_{i,j}$. The coefficients of thrust, torque and power are given respectively by

$$C_T = \frac{4\pi^2 N_B T}{\rho\Omega^2 D^4} \tag{40}$$

$$C_{QI} = \frac{4\pi^2 N_B Q_I}{\rho\Omega^2 D^5} \tag{41}$$

$$C_p = 2\pi C_Q \tag{42}$$

where D is the propeller diameter. The figure of merit is given by

$$F/M = \frac{T}{\Omega Q}\sqrt{\frac{T}{2\pi\rho R^2}} \tag{43}$$

The profile torque per [illegible]en by

$$\int_T^2 C_D\,(\text{chord})\,r\,dr \tag{44}$$

where C_D is the (viscous) drag coefficient. The total torque per blade is given by the sum of Eqs. (36) and (44).

SECTION IV

INTERPRETATION OF NUMERICAL RESULTS

1. DESCRIPTION OF PROPELLER GEOMETRIES

The three propellers chosen for this study are listed below, together with the source of data for each:

1. Canadair Propeller RAA-240-108, Ref. 21 (Hartzell Model 10178)

2. Canadair Propeller 240-3A5, Ref. 4

3. Hamilton Standard Propeller 212X-16, Ref. 4

The computer program input parameters for each of these propellers are listed in Tables I, II, and III, respectively, as spanwise distributions. A brief discussion of certain of these parameters is in order here to permit a clear understanding of the meaning of each.

The blade pitch angle distribution, α, is the angular orientation of the blade at each radial station relative to the plane of rotation for a specific value of this angle at the 3/4 radius station, α_{75}, which is called the blade collective pitch. In the case of the RAA-240-108 propeller this value of collective pitch is α_{75} = 12 deg (Table I). For both the 240-3A5 and the 212X-16 propellers it is α_{75} = 10 deg (Tables II and III). All three distributions are plotted in Fig. 12. The α distribution is used in the lifting surface portion of the computer program.

The column entitled blade pitch increment distribution, $\Delta\alpha$, is actually the sum of the blade pitch increment angle (relative to the blade pitch angle at the 3/4 radius station) and the zero lift offset angle, or

$$\Delta\alpha = \alpha - \alpha_{75} + \alpha_{0L} \tag{45}$$

This quantity is evaluated at the center of each input element and, accordingly, is tabulated between blade stations. This distribution is used, together with the input value of α_{75}, in the lifting line portion of the computer program to compute the inflow and wake paremeters.

There are two lift-curve slope distributions tabulated for the RAA-240-108 propeller in Table I, and only one each for the other two propellers in Tables II and III. First consider Table I. The values in the column labeled a_1 were taken from the lifting line evaluation of this propeller performed by the Hamilton Standard Division (HSD) (unpublished) and represent what is felt to be a reasonable set of values of the incompressible lift-curve slope distribution. This distribution is plotted as a solid line in Fig. 13. The values in the column labeled a_2 were taken from a curve in Ref. 21 and were modified to have a maximum value not exceeding 2π. The original lift-curve slope distribution from Ref. 21 had very large values of a_2 near the blade hub, in excess of 9. Although values of a near 7 were felt to be acceptable for thick sections (cf. Fig. 38 of Ref. 22), as given by the HSD distribution, it was felt that the original distribution in Ref. 21 was not reasonable, and the values were limited accordingly to the maximum theoretical flat plate value of 2π. Calculations were performed for both of these distributions, and the results will be described below.

In Tables II and III the values of a were again taken from unpublished work by HSD for the 240-3A5 and 212X-16 propellers, and these distributions are found in Figs. 14 and 15, respectively.

Another set of important input quantities to the computer program, the values of the wake velocity parameters k_1 and k_2 (Ref. 5), are found in Table IV. These values were obtained by first running the HSD version (Ref. 4) of the UARL Prescribed Wake program (Ref. 5) for each blade and at each of three values of collective pitch: α_{75} = 12, 14, 16 deg for the RAA-240-108 propeller and α_{75} = 10, 12, 14 deg for both the 240-3A5 and the 212X-16 propellers. The HSD program performs a self-contained iteration that yields values of k_1 and k_2 which are compatible with the predicted thrust, and hence yields a realistic prediction of the velocity field. (Note that values of k_1 and k_2 may also be obtained from the curves in Ref. 4.)

2. PERFORMANCE CALCULATIONS

The input variables described above were introduced into the computer program described in Fig. 10 and in Appendix II. The direct problem mode was implemented in which the blade geometry is given and the circulation distribution and propeller performance are determined. Before the final calculations were made for all three configurations, a grid size sensitivity study was performed for the RAA-240-108 propeller at a collective pitch angle of α_{75} = 14 deg. In this study both the grid size and the location of the chordwise demarcation line between the inboard coarse grid and the outboard fine grid were varied. An "optimum" grid arrangement was determined which appeared to yield nearly the same results as a finer grid but took less time to execute than the finer grid. Details of this study will be found in Appendix III.

Of the three blade configurations chosen for analysis, the RAA-240-108 had the largest amount of measured data, including detailed chordwise pressure measurements at a number of spanwise stations. Unfortunately it also was a poorly documented blade configuration in that virtually no detailed section data were available to Canadair when the propeller was acquired. Nevertheless, because of the large amounts of surface pressure data available for this blade it was widely used in the comparisons between theory and experiment described below.

Figure 16 contains plots of C_T and C_Q versus α_{75} and of C_T versus C_Q for the Canadair RAA-240-108 propeller. The available experimental data from Ref. 21 are shown as circled points from pressure measurements and triangular points from balance measurements. The solid line is the present lifting surface theory using lift-curve slope values, a_1, from the HSD program and the dashed line is the same lifting surface theory using lift-curve slope values, a_2, from Ref. 21 with the restriction that $a_2 \leq 2\pi$. For comparison the lifting line results from the HSD program (Ref. 4) are shown as the dash-dot curves. It should be noted that these plots have non-zero or "false" origins, which tend to exaggerate the differences between the results. It can be seen that the agreement between all three theoretical curves and the experimental measurements is quite good, although the best agreement seems to be between the data and the lifting line results. However, it is important to realize that for the lifting line theory to achieve this agreement it was necessary to include a three-dimensional correction factor as an input item (see Fig. 22 of Ref. 4). In contrast to this, the present lifting surface theory has no three-dimensional input correction factor within the lifting surface portion of the program -- this portion of the program automatically accounts for the three-dimensionality of the flow near the tip.

Another important factor here lies in the spanwise distribution of angle of zero lift used in these calculations. A possibility exists that the values used were approximately 4 deg more negative than they should have been. However, because of poor documentation on this blade it is not possible to verify this possibility. If this is true, then the built-in lifting line subprogram in the current lifting surface program will produce a set of axial velocities that are too large. Experience has shown, during the early phases of this work, that if the axial velocity is too large, the error in the reference surface orientation is such that the thrust is virtually unaffected (cosine of the error angle) but the torque will be overpredicted by a significant amount (sine of the error angle). Hence the overprediction of torque coefficient in the second and third panels of Fig. 16 may stem from just such an error.

Comparable performance plots will be found in Figs. 17 and 18 for the 240-3A5 and 212X-16 propellers, respectively. The reasons for the discrepancies observed in Fig. 17 could not be discovered in the course of this

investigation. In Fig. 18 both lifting surface and lifting line predictions were in good agreement, and although they underpredicted C_T and C_Q when plotted versus α_{75}, the crossplot of C_T versus C_Q showed good trend agreement. As noted before, the use of a false origin tends to exaggerate any lack of agreement between results from different sources, and it is felt that this new theory yields a satisfactory degree of accuracy at this early stage in its development, sufficient to warrant further studies. This assertion is further borne out in the next section which deals with the details of the blade surface pressures.

3. SURFACE PRESSURES

A major advantage of lifting surface theory is its ability to predict details of the local load distribution at any point on the blade surface. In view of the availability of such data on the Canadair RAA-240-108 propeller (Ref. 21) it was possible to evaluate the validity and accuracy of the theory directly. This is a meaningful evaluation because, as stated in the previous section, the most likely source of input error for this propeller will lead only to an error in axial velocity which affects torque much more than it affects thrust. Consequently, the pressure calculations from Eq. (39) will also be relatively unaffected.

Pressure distributions, both chordwise and spanwise, are calculated routinely by the lifting surface program, and computations were made and are examined below for the Canadair RAA-240-108 propeller for three values of collective pitch and for both lift-curve slope distributions listed in Table I. Figures 19, 20, and 21 are plots of the spanwise distribution of ΔC_p for α_{75} = 12, 14, and 16 deg, respectively. In the first of each set the figure labeled a) used the lift-curve slope a_1 from HSD and the figure labeled b) used the lift-curve slope a_2 from Ref. 21 (with the restriction $a_2 \leq 2\pi$). It is seen that the only significant differences in these distributions occur in the aft region of the blade near r/R = 0.85. Everywhere else the distributions are virtually the same. It should be noted that in Fig. 16 it was observed that the lifting surface thrust curves (related to pressure by integration) for these two slopes were essentially the same also, while the torque differed by a significant amount, ascribable only to changes in a and the consequent changes in axial velocity. This is in accordance with the statements made earlier about the relative insensitivity of thrust and the relative sensitivity of torque to changes in axial velocity.

A further appreciation of the ability of the theory to represent the three-dimensional details of the tip loading can be gained by studying Figs. 22, 23, and 24 which are plots of ΔC_p versus chordwise position for the three values of collective pitch. Each figure has four panels for radius ratio values of r/R = 0.80, 0.88, 0.92, and 0.96. Here we have

plotted the lifting surface theory for the two slopes, a_1 and a_2, as a solid line and a dash-dot line. Also on each panel the experimentally measured pressure distribution is plotted. It is seen that, in general, there is very good agreement between theory and experiment for all conditions shown here. There is particularly good agreement near the tip (r/R = 0.92, 0.96) for both α_{75} = 12 and 14 deg. This is significant in that no input values or other artificialities were required to correct for three-dimensional effects. Some deterioration in agreement is observable at α_{75} = 16 deg.

Finally, it should be noted that the spanwise curves of ΔC_p in Figs. 19, 20, and 21 require some interpretation, in that the apparently high inboard loadings are artificial because they arise from division by a small inboard value of the square of the velocity in Eq. (39). The actual pressure difference Δp was calculated by rewriting Eq. (39) in the form

$$\Delta p = \frac{1}{2} \rho V_T^2 \Delta C_p = \frac{T_{i,j} \sec \beta \left(r_j^{(g)}\right)}{A_{i,j}} \qquad (46)$$

and the results are plotted in Figs. 25, 26, and 27 for α_{75} = 12, 14, 16 deg, using a_1 only. This has been done to place these results in proper perspective by displaying the physical load distribution that contributes to the blade thrust.

SECTION V

CONCLUSIONS

The following conclusions were reached in the course of this investigation.

1. The lifting surface theory described herein is capable of predicting the gross performance characteristics of statically operating propellers, either as a direct application (geometry prescribed) or as an indirect application (loading prescribed).

2. The lifting surface theory described herein is also capable of predicting details of the surface pressure distributions.

3. The theory can account for three-dimensional tip effects automatically without the need for artificially inserted three-dimensional tip corrections.

4. The theory can be extended to permit a study of the noise associated with a statically operating propeller.

SECTION VI

RECOMMENDATIONS FOR FURTHER RESEARCH

As with most new theories, the lifting surface formulation described in this report will require additional effort to test its limits and to evaluate its sensitivities to parameter changes. Although one major sensitivity study of the grid geometry has already been carried out (Appendix III) many other such studies must be performed with blade shape, blade twist, section lift coefficient, etc., as the significant parameters to be varied in a systematic manner. In these studies particular care must be taken to ensure that the axial velocity distribution over the blade is reasonable because of its strong influence on the torque prediction.

In the course of this investigation, a major deficiency was the lack of reliable data for use in evaluating the theory. Although pressure and balance data were available (on one blade only) these data were not felt to be completely reliable because the blade sections were not documented. What is needed for future work is a detailed, controlled test program, similar to the test of Ref. 21, with combined surface pressure and balance measurements, but with complete documentation on static blade characteristics (profile shape, section lift and drag, etc.) and on external flow into the rotor disk. Only then can a truly fair test of the theory be made.

At the outset of this investigation an effort was made to incorporate the least complicated version of the UARL lifting line program (Ref. 5) into the lifting surface program. This subprogram is needed to compute the inflow velocities and to set up the orientation of the reference surface for each blade in preparation for subsequent calculations with the lifting surface theory. Two very important input elements here are k_1 and k_2, the wake velocity parameters, which must be compatible with the rotor thrust to ensure a reasonable axial velocity distribution. As used herein, the lifting line program had to be run separately to obtain k_1 and k_2, and then the full lifting surface program was run. Even here complete compatibility was not assured because if the lifting surface thrust was significantly different from the lifting line thrust a correction should have been made to k_1 and k_2. Hence the further refinement of this program should incorporate two internal iterative procedures. First, the self-contained HSD lifting line program (Ref. 4) should be inserted in place of the present lifting line subprogram. This is because the HSD program incorporates an iteration to match lifting line thrust with k_1 and k_2. Second, the entire program should be made iterative such that the final lifting surface thrust should be matched to the k_1 and k_2 values for compatibility. If they are compatible the computation is ended, but if they are not the new thrust value is used to select a new pair of k_1 and k_2 values and the entire procedure is repeated to convergence.

Finally, this theory should be amenable to the prediction of noise for a statically operating propeller. This is particularly important because current and advanced noise theories require information on the distributed loading on the blades and the only two sources of this information are experiment and lifting surface theory. Appendix IV outlines a procedure whereby the present theory could be extended to compute the acoustic pressure field surrounding the propeller.

REFERENCES

1. Goldstein, S.: On the Vortex Theory of Screw Propellers. Proceedings of the Royal Society, Series A, Vol. 123, 1929.

2. Lock, C.: Application of Goldstein's Airscrew Theory to Design. Aeronautical Research Committee Reports and Memoranda 1377, November 1930.

3. Jenney, D. S., J. R. Olson, and A. J. Landgrebe: A Reassessment of Rotor Hovering Performance Prediction Methods. Journal of the American Helicopter Society, Vol. 13, No. 2, April 1968, pp. 1-26.

4. Ladden, R. M. and D. C. Gilmore: Advanced V/STOL Propeller Technology, Vol. II, Static Thrust Prediction Method Development. Technical Report AFFDL-TR-71-88, Vol. II, Air Force Flight Dynamics Laboratory, WPAFB, Ohio, September 1971.

5. Landgrebe, A. J.: An Analytical and Experimental Investigation of Helicopter Rotor Performance and Wake Geometry Characteristics. USAAMRDL Technical Report 71-24, Eustis Directorate, U. S. Army Air Mobility Research and Development Laboratory, Fort Eustis, Virginia, June 1971.

6. Watkins, C. E., H. L. Runyan, and D. S. Woolston: A Systematic Kernel Function Procedure for Determining Aerodynamic Forces on Oscillating or Steady Finite Wings at Subsonic Speeds. NASA Technical Report R-48, 1959.

7. Ludwieg, H. and J. Ginzel: Zur Theorie der Breit-blattschraube. Aerodynamishe Versuchsanstalt, Göttingen, Rept. 44/A/08, 1944.

8. Nelson, D. M.: A Lifting Surface Propeller Design Method for High-Speed Computers. NAVWEPS Report 8442, NOTS, China Lake, California, 1964.

9. Strecheletzky, M.: Hydrodymische Grundlagen zur Berechnung der Schiffsschrauben. Verlag G. Braun, Karlsruhe, 1950.

10. Guilloton, R.: Calcul des vitesses induites en vue du tracé des helices. Schiffstechnik 4, 1957.

11. Kerwin, J. E.: The Solution of Propeller Lifting-Surface Problems by Vortex Lattice Methods. Department of Naval Architecture, Massachusetts Institute of Technology, 1961.

REFERENCES (Continued)

12. Landgrebe, A. J.: An Analytical Method for Predicting Rotor Wake Geometry. AIAA Paper 69-196, Presented at the AIAA/AHS VTOL Research, Design, and Operating Meeting, February 17-19, 1969.

13. Jones, J. P.: Rotor Aerodynamics - Retrospect and Prospect. Paper 1, Aspects of V/STOL Aircraft Development. North Atlantic Treaty Organization, Advisory Group for Aerospace Research and Development, Advisory Report 13, 1967.

14. Peracchio, A. A.: Discussion of the Lifting Line Theory of Propellers. Hamilton Standard Division of United Aircraft, Report HSIR 2451, April 1966.

15. Erickson, J. C. and G. R. Hough: Fluctuating Flow Field of Propeller in Cruise and Static Operation. Journal of Aircraft, Vol. 7, No. 1, January-February 1970.

16. Erickson, J. C., Jr.: Theoretical and Experimental Investigations of V/STOL Propeller Operation in a Static Condition. USAAVLABS Technical Report 69-55, U. S. Army Aviation Materiel Laboratories, Fort Eustis, Virginia, October 1969.

17. Kerwin, J. E.: Linearized Theory for Propellers in Steady Flow. Department of Naval Architecture, Massachusetts Institute of Technology, July 1963.

18. Murray, J. C.: Propeller Lifting Surface Theory Formulation for Zero Advance Ratio. Hamilton Standard Division of United Aircraft, Report HSER 5169, September 1968.

19. Ashley, H. and M. Landahl: Aerodynamics of Wings and Bodies. Addison Wesley, 1965, pp. 132-133.

20. Lerbs, H. W., W. Alef, and K. Albrecht: Numerical Analysis of Propeller Lifting-Surface Theory. Translation #33, David Taylor Model Basin, Washington, D. C. 20007, 1966.

21. Gilmore, D. C.: Measurements of the Surface Pressure Distribution on a Propeller Operating at Zero Advance Ratio. Canadair Report RAA-240, USAF Contract No. F33615-69-C-1720, July 1970.

22. Abbott, I. H., A. E. von Doenhoff, and L. S. Stivers: Summary of Airfoil Data. NACA Report No. 824, 1945.

23. Milne, Thomson, L. M.: Theoretical Aerodynamics. Macmillan, 1958, p. 169.

24. Garrick, I. E. and C. E. Watkins: A Theoretical Study of the Effect of Forward Speed on the Free-Space Sound Pressure Field Around Propellers. Report 1198, NACA 1954.

25. Barry, F. W. and B. Magliozzi: Noise Detectability Prediction Method for Low Tip Speed Propellers. Technical Report AFAPL-TR-71-37, June 1971.

APPENDIX I

DERIVATION OF THE FIELD POINT BOUNDARY CONDITION IN VORTEX LATTICE THEORY

The physical requirement that the fluid does not penetrate the blade surface is given by Eq. (24) and is valid for every point on the blade. In the theoretical numerical model this is replaced by Eq. (29) which is applied at MN field points. The derivation of Eq. (29) is based on the simple algebraic formulas for computing the velocity induced by a straight line vortex filament.

In the case of a straight line vortex filament of strength K located on the line AB (see Fig. 28) the velocity induced at a point O normal to the plane of the paper is given by

$$v = \frac{K}{4\pi h} (\cos \theta_1 + \cos \theta_2) \tag{47}$$

where h is the distance between the point O and the line AB, and the angles θ_1 and θ_2 are the angles that the lines OA and OB make with AB. This formula results from evaluating the Biot-Savart integral (see Ref. 23).

In the vortex lattice formulation the field points are located at the centroids of each elemental area. The induced velocity vector at any field point is found by applying Eq. (47) to each vortex filament. In each of these computations it is seen from Eq. (47) that the contribution of each filament is proportional to the vortex filament strength. The distance h and the angles θ_1 and θ_2 are computed in terms of the coordinates of the points of the lattice. In what follows we will give a derivation of Eq. (29) using Eq. (47).

The Cartesian coordinates of a lattice point (ℓ,m,k) on the kth blade reference surface are denoted by $(x^{(g)}_{\ell,m,k}, y^{(g)}_{\ell,m,k}, z^{(g)}_{\ell,m,k})$ and the Cartesian coordinates of a field point on the first blade reference surface are denoted by $(x^{(f)}_{i,j}, y^{(f)}_{i,j}, z^{(f)}_{i,j})$ where, for example, the x field point coordinate is defined to be located at the centroid of the surrounding four lattice points on the first reference surface, or

$$x^{(f)}_{i,j} = \frac{1}{4}\left(x^{(g)}_{i,j,1} + x^{(g)}_{i+1,j,1} + x^{(g)}_{i,j+1,1} + x^{(g)}_{i+1,j+1,1}\right) \tag{48}$$

with similar equations for $y^{(f)}_{i,j}$ and $z^{(f)}_{i,j}$. We consider a typical radial vortex filament of strength Γ_r located on the line joining the lattice points (ℓ,m,k) and $(\ell,m+1,k)$ on the kth blade reference surface (see Fig. 29). The distance h_r of this filament from the field point $(x^{(f)}_{i,j}, y^{(f)}_{i,j}, z^{(f)}_{i,j})$ is given by

$$h_r = \sqrt{\frac{(Q_{2r}\,P_{1r} - P_{2r}\,Q_{1r})^2 + (R_{2r}\,Q_{1r} - Q_{2r}\,R_{1r})^2 + (R_{2r}\,P_{1r} - P_{2r}\,R_{1r})^2}{P_{1r}^2 + Q_{1r}^2 + R_{1r}^2}} \tag{49}$$

and $\cos\theta_{1r}$, $\cos\theta_{2r}$ can be expressed in the form

$$\cos\,\theta_{1r} = -\frac{P_{2r}\,P_{1r} + Q_{2r}\,Q_{1r} + R_{2r}\,R_{1r}}{\sqrt{(P_{1r}^2 + Q_{1r}^2 + R_{1r}^2)\,(P_{2r}^2 + Q_{2r}^2 + R_{2r}^2)}} \tag{50}$$

$$\cos\,\theta_{2r} = \frac{P_{3r}\,P_{1r} + Q_{3r}\,Q_{1r} + R_{3r}\,R_{1r}}{\sqrt{(P_{1r}^2 + Q_{1r}^2 + R_{1r}^2)\,(P_{3r}^2 + Q_{3r}^2 + R_{3r}^2)}} \tag{51}$$

where

$$P_{1r} = x^{(g)}_{\ell,m,k} - x^{(g)}_{\ell,m+1,k} \tag{52a}$$

$$P_{2r} = x^{(f)}_{i,j} - x^{(g)}_{\ell,m,k} \tag{52b}$$

$$P_{3r} = X^{(f)}_{i,j} - X^{(g)}_{\ell,m+1,k} \tag{52c}$$

$$Q_{1r} = y^{(g)}_{\ell,m,k} - y^{(g)}_{\ell,m+1,k} \tag{53a}$$

$$Q_{2r} = y^{(f)}_{i,j} - y^{(g)}_{\ell,m,k} \tag{53b}$$

$$Q_{3r} = y^{(f)}_{i,j} - y^{(g)}_{\ell,m+1,k} \tag{53c}$$

$$R_{1r} = Z^{(g)}_{\ell,m,k} - Z^{(g)}_{\ell,m+1,k} \tag{54a}$$

$$R_{2r} = Z^{(f)}_{i,j} - Z^{(g)}_{\ell,m,k} \tag{54b}$$

$$R_{3r} = Z^{(f)}_{i,j} - Z^{(g)}_{\ell,m+1,k} \tag{54c}$$

The unit vector $\vec{i}_r$ normal to the plane passing through the field point on the first blade and the points (ℓ,m,k) and $(\ell,m+1,k)$ at the ends of the vortex filament on the kth blade is given by

$$\vec{i}_r = \frac{Q_{2r} R_{3r} - R_{2r} Q_{3r} \;,\quad R_{2r} P_{3r} - P_{2r} R_{3r} \;,\quad P_{2r} Q_{3r} - P_{3r} Q_{2r}}{\sqrt{(P_{2r}^2 + Q_{2r}^2 + R_{2r}^2)(P_{3r}^2 + Q_{3r}^2 + R_{3r}^2) - (P_{2r} P_{3r} + Q_{2r} Q_{3r} + R_{2r} R_{3r})^2}} \tag{55}$$

The velocity induced at the field point $(x_{i,j}^{(f)}, y_{i,j}^{(f)}, z_{i,j}^{(f)})$ by the radial vortex filament of strength $\Gamma_{r_{\ell,m}}^{\ell,m+1}$ which is located on the line joining the lattice points (ℓ,m,k) and $(\ell,m+1,k)$ on the kth blade reference surface will be denoted by $(u_{kx}^{(rb)}, u_{ky}^{(rb)}, u_{kz}^{(rb)})$ and is given by

$$\left(u_{kx}^{(rb)}, u_{ky}^{(rb)}, u_{kz}^{(rb)}\right) = \frac{\Gamma_{r_{\ell,m}}^{\ell,m+1}}{4\pi h_r} (\cos\theta_{1r} + \cos\theta_{2r})\, \vec{i}_r \tag{56}$$

In the case of a chordwise vortex filament of strength $\Gamma_{s_{\ell,m}}^{\ell+1,m}$ which is located on the line joining the lattice points (ℓ,m,k) and $(\ell+1,m,k)$ on the kth blade reference surface the corresponding induced velocity is denoted by $(u_{kx}^{(sb)}, u_{ky}^{(sb)}, u_{kz}^{(sb)})$ and is given by

$$(u_{kx}^{(sb)}, u_{ky}^{(sb)}, u_{kz}^{(sb)}) = \frac{\Gamma_{s_{\ell,m}}^{\ell+1,m}}{4\pi h_s} (\cos\theta_{1s} + \cos\theta_{2s})\, \vec{i}_s \tag{57}$$

where

$$\cos\theta_{1s} = -\frac{P_{2s} P_{1s} + Q_{2s} Q_{1s} + R_{2s} R_{1s}}{\sqrt{(P_{1s}^2 + Q_{1s}^2 + R_{1s}^2)(P_{2s}^2 + Q_{2s}^2 + R_{2s}^2)}} \tag{58}$$

$$\cos \theta_{2s} = \frac{P_{3s} P_{1s} + Q_{3s} Q_{1s} + R_{3s} R_{1s}}{\sqrt{(P_{1s}^2 + Q_{1s}^2 + R_{1s}^2)(P_{3s}^2 + Q_{3s}^2 + R_{3s}^2)}} \tag{59}$$

$$h_s = \sqrt{\frac{(Q_{2s}P_{1s} - P_{2s}Q_{1s})^2 + (R_{2s}Q_{1s} - Q_{2s}R_{1s})^2 + (R_{2s}P_{1s} - P_{2s}R_{1s})^2}{P_{1s}^2 + Q_{1s}^2 + R_{1s}^2}} \tag{60}$$

$$P_{1s} = x^{(g)}_{\ell,m,k} - x^{(g)}_{\ell+1,m,k} \tag{61a}$$

$$P_{2s} = x^{(f)}_{i,j} - x^{(g)}_{\ell,m,k} \tag{61b}$$

$$P_{3s} = x^{(f)}_{i,j} - x^{(g)}_{\ell+1,m,k} \tag{61c}$$

$$Q_{1s} = y^{(g)}_{\ell,m,k} - y^{(g)}_{\ell+1,m,k} \tag{62a}$$

$$Q_{2s} = y^{(f)}_{i,j} - y^{(g)}_{\ell,m,k} \tag{62b}$$

$$Q_{3s} = y_{i,j}^{(f)} - y_{\ell+1,m,k}^{(g)} \tag{62c}$$

$$R_{1s} = z_{\ell,m,k}^{(g)} - z_{\ell+1,m,k}^{(g)} \tag{63a}$$

$$R_{2s} = z_{i,j}^{(f)} - z_{\ell,m,k}^{(g)} \tag{63b}$$

$$R_{3s} = z_{i,j}^{(f)} - z_{\ell+1,m,k}^{(g)} \tag{63c}$$

The unit vector $\vec{i}_\xi$ is defined in a similar manner as $\vec{i}_r$ and is normal to the plane through the field point on the first blade reference surface and the points (ℓ,m,k) and $(\ell+1,m,k)$ on the kth blade reference surface.

The total velocity induced by all the radial and chordwise vortex filaments at the field point $(x_{i,j}^{(f)}, y_{i,j}^{(f)}, z_{i,j}^{(f)})$ will be denoted by $(u_x^{(b)}, u_y^{(b)}, u_z^{(b)})$ and is given by

$$(u_x^{(b)}, u_y^{(b)}, u_z^{(b)}) = \sum_{k=1}^{N_B} \sum_{m=1}^{N} \sum_{\ell=1}^{M} \left\{ (u_{kx}^{(rb)}, u_{ky}^{(rb)}, u_{kz}^{(rb)}) + (u_{kx}^{(sb)}, u_{ky}^{(sb)}, u_{kz}^{(sb)}) \right\} + \sum_{k=1}^{N_B} \sum_{\ell=1}^{M} (u_{kx}^{(sh)}, u_{ky}^{(sh)}, u_{kz}^{(sb)})_{m=N+1} \tag{64}$$

In cylindrical coordinates the velocity induced at a field point is given by

$$(u_x^{(b)}, u_r^{(b)}, u_\theta^{(b)}) = (u_x^{(b)}, \; u_y^{(b)} \cos \theta_{i,j}^{(f)} + u_z^{(b)} \sin \theta_{i,j}^{(f)}, \; u_z^{(b)} \cos \theta_{i,j}^{(f)} - u_y^{(b)} \sin \theta_{i,j}^{(f)}) \tag{65}$$

where $(x_{i,j}^{(f)}, r_{i,j}^{(f)}, \theta_{i,j}^{(f)})$ are the cylindrical coordinates of the field points. The velocity component normal to the blade reference surface will be denoted by $u_n^{(b)}$ and is given by

$$u_n^{(b)} = u_x^{(b)} \cos \beta_j - u_\theta^{(b)} \sin \beta_j \tag{66}$$

where β_j is the value of β at the radial location $r = r_{i,j}^{(f)}$. The normal velocity induced by the trailing vortex system at the field point is denoted by $u_n^{(t)}$ and is given by

$$u_n^{(t)} = \sum_{m=1}^{N+1} C_t^{(m)} \Gamma_t^{(m)} \tag{67}$$

where $\Gamma_t^{(m)}$ denotes the strength of the trailing vortex filaments and $C_t^{(m)}$ is a coefficient which depends on the wake vortex geometry only. The UARL lifting line program for statically operating rotors is used to compute $u_n^{(t)}$ (see Ref. 5).

The total normal velocity induced at the field point by the complete vortex system comprising the blades and the wake is denoted by u_n and is given by

$$u_n = u_n^{(t)} + u_n^{(b)} \tag{68}$$

The right-hand side of Eq. (67) will be a linear function of $\Gamma_{r_{\ell,m}}^{\ell,m+1}$, $\Gamma_{s_{\ell,m}}^{\ell+1,m}$, and $\Gamma_t^{(m)}$. After a simple rearrangement of the terms in the equation the total normal velocity induced at the field point can be written in the form

$$u_n = \sum_{\ell=1}^{M+1} \sum_{m=1}^{N} C_r^{(\ell,m)} \Gamma_{r_{\ell,m}}^{\ell,m+1} + \sum_{\ell=1}^{M} \sum_{m=1}^{N+1} C_s^{(\ell,m)} \Gamma_{s_{\ell,m}}^{\ell+1,m} + \sum_{m=1}^{N+1} C_t^{(m)} \Gamma_t^{(m)} \tag{69}$$

where the coefficients $C_r^{(\ell,m)}$, $C_s^{(\ell,m)}$, and $C_t^{(m)}$ are dependent on the vortex geometry only. In the right-hand side of Eq. (24) the term $(dn/ds)_{ML}$ can be replaced by δ where δ is the angle that the mean line makes with the chord in the (s,n) plane (see Fig. 7). The field point boundary condition expressed by Eq. (24) will now have the form

$$\sum_{\ell=1}^{M+1} \sum_{m=1}^{N} C_r^{(\ell,m)} \Gamma_{r_{\ell,m}}^{\ell,m+1} + \sum_{\ell=1}^{M} \sum_{m=1}^{N+1} C_s^{(\ell,m)} \Gamma_{s_{\ell,m}}^{\ell+1,m} + \sum_{m=1}^{N+1} C_t^{(m)} \Gamma_t^{(m)} = V_s (\alpha + \delta) \tag{70}$$

which was stated earlier in the main body of the report in Eq. (29).

APPENDIX II

USER'S MANUAL

In this Appendix the details of the UARL lifting surface program will be discussed. Descriptions are given of the input formats, the output formats and the interactions between the various subprograms, in that order. A key feature of the input format used here is the ability of the user to run multiple cases with a minimum of changes in the input data. This is also discussed below.

1. BASIC INPUT

Each case defined by the input data set to the program must contain three important components in the following order: a title card, the LOADER format input items and a multiple case control card. The title card for each case contains a one card title (columns 1-72) which describes the case.

The basic input format is in the LOADER format (specified by subroutine LADDER). The input items are assigned location numbers within a storage array. Using the subroutine LADDER an input item may be changed simply by specifying the location number and input item value on a card following the card on which the original value for the item was located. In addition, items which are unchanged between consecutive cases need not be repeated in the input for the successive cases. The LOADER format is as follows:

LL L DATA(L) DATA(L+1) ... DATA(L+LL-1)

where: LL is the word count; i.e., the number of data items on a card (Columns 1 and 2, fixed point, right adjusted).

L is the location number of the first data item on the card (Col. 3-6, fixed point, right adjusted).

DATA represents the various input item values on the card (Col. 7-18, 19-30, 31-42, 43-54, 55-66; floating point numbers).

The location numbers, program symbols, and description of each input item are given below.

LOCATION	PROGRAM SYMBOL	PROGRAM INPUT LABEL	DESCRIPTION OF INPUT ITEM
1	OMGR	TIP SPEED	Propeller tip speed, fps. Product of the propeller rotational velocity and the propeller radius (ft).
2	BL	NO. OF BLADES	Number of blades.
3	REV	NO. OF WAKE REVS	Number of wake revolutions. Maximum value of REV is 10.0.
4	DPSI	AZIMUTH INCREMENT	Azimuth increment, deg. This input item defines the length of the trailing vortex segments used in the wake model. The minimum value of DPSI is 15.0 deg. A typical value is 30.0 deg.
5	SOUND	SPEED OF SOUND	Speed of sound, fps. This input item is used in the calculation of local Mach number.
6	THETA1	LINEAR TWIST	Blade linear twist rate, deg. This input item is used to calculate the blade built-in pitch distribution, and is normally negative to indicate decreased built-in pitch angles at the blade tip (See THET75 below).
7	THET75	COLLECTIVE PITCH	Blade collective pitch at the blade 75 percent radial station, deg. This item is used in conjunction with THETA1 to calculate the blade pitch distribution at the segment centers of the input radial stations. The formula used in computing pitch is THETA(r/R) = THET75 + THETA1* (r/R) - 0.75) + DTHETA where r/R is dimensionless blade radial station and DTHETA is defined below (location 35-54).
8-34	CURVE	MACH NUMBER, LIFT CURVE SLOPE	Combinations of Mach number (CMACH) and lift curve slope (ALIFT) to define airfoil lift characteristics used in UARL lifting-line subprogram

			for statically operating rotors. The sequence of input Mach numbers is followed by the corresponding sequence of lift curve slopes (the Mach numbers are arranged in a monotonically increasing sequence starting with zero).
35-54	DTHETA	BLADE PITCH INCREMENT	= $\alpha - \alpha_{75} + \alpha_{0L}$ where $\alpha - \alpha_{75}$ is the geometric pitch increment at the blade radial segment centers and α_{0L} is the α intercept, measured in degrees, of the lift curve.
55	TOL	CONVERGENCE TOLERANCE	Tolerance for Gauss-Seidel iteration. This parameter usually has the value 0.00001.
57	STNS	NO. OF BLADE STATIONS	Number of input radial stations. Maximum value of STNS = 20.0.
58-84	ACURVE	MACH NO., ALPHA MAX	Combinations of Mach number (CMACH) and stall angle of attack (ALPMAX) to define the maximum section lift coefficients used in UARL lifting-line program for statically operating rotors. The maximum (stalled) lift coefficient for each section is equal to the product of the lift curve slope and the stall angle of attack corresponding to the section Mach number. The sequence of input Mach numbers is followed by the corresponding sequence of stall angle of attack values (the Mach numbers are input in a monotonically increasing sequence starting with zero).
85	PROBPR	DIRECT PROBLEM INDIRECT PROBLEM	Problem selection parameter. PROBPR = 0.0 for direct problem, PROBPR = 1.0 for indirect problem.

86	BLDTYP	CONTINUOUS CASE, DISCONTINUOUS CASE	Blade type. T = 0.0 - discontinuous blade perimeter slope. T = 1.0 - continuous blade perimeter slope.
87	EBG		Accuracy parameter used in interpolation algorithm to determine aerodynamic tip in the case T = 1.0. Usually EBG = 0.1.
88	EV	LEADING EDGE PARAMETER	Leading edge parameter defining distance of leading edge from leading vortex filament. Measured in feet.
89	RTR	DEMARCATION LINE	Radial distance of demarcation line separating the blade tip region from the inboard region. Measured in feet.
90	XN1G	INBOARD CHORD SEGMENTS	Number of radial segments in the computation grid from hub to demarcation line.
91	XN2G	OUTBOARD CHORD SEGMENTS	Number of radial segments in the computation grid from demarcation line to tip.
92	XMLG	LEADING CIRCUMFERENTIAL SEGMENTS	Number of chordwise segments in the computation grid from leading edge to reference line.
93	XMTG	TRAILING CIRCUMFERENTIAL SEGMENTS	Number of chordwise segments in the computation grid from trailing edge to reference line.
94	XL		Number of points of discontinuity in blade perimeter slope minus one. Case T = 0.0 only.
95-104	XMG1		Number of radial segments in the computation grid from the demarcation line to the radial location of the first discontinuity, from the radial location of the first

			discontinuity to the radial location of the second discontinuity, ... and from the radial location of the last discontinuity to the radial location of the tip. Case T = 0.0 only.
105-124	R	BLADE RADIUS	Radial coordinate, in feet, of the input grid.
125-144	SL	LEADING EDGE	Leading edge chord distance, in feet, at the radial stations of the input grid.
145-164	ST	TRAILING EDGE	Trailing edge chord distance, in feet, at the radial stations of the input grid.
165	XN1		Number of tip region points along leading edge.
166	XN2		Number of tip region points along trailing edge.
167-186	RTIP	BLADE RADIUS	Radial coordinates of tip region points in feet. The sequence of tip coordinate points starts at the demarcation line on the leading edge and proceeds around the perimeter of the tip region to the demarcation line on the trailing edge.
187-206	STIP	CHORD MEASURE	Chord distance, in feet, of tip region points from the reference line. Corresponding sequence to RTIP coordinates.
207	XM1		Number of chordwise input points for leading edge region local angle of attack distribution.
208	XM2		Number of chordwise input points for trailing edge local region angle of attack distribution.

209-228	ALPHA	BLADE PITCH ANGLE	Pitch angle in degrees defined at input radial stations. Case PROBPR = 0.0 only.
229-428	CAMB		Local blade slope distribution at points of input grid. Case PROBPR = 0.0 only.
429-599	GAMRX		Circulation strengths of radial vortex filaments located on computation grid. Case PROBPR = 1.0 only.
601	XNPT		Number of Mach number-lift curve slope combinations. This number must be the same as the Mach number -ALPMAX combinations.
602	XIOPT		Option for the vortex sheet boundary within a wake azimuth of 360/BL and the blade (floating point). Normally set XIOPT = 1 to establish a parabolic vortex sheet boundary through (1) the origin of the outermost vortex sheet filament at the blade, (2) the rolled up tip filament coordinates at an azimuth of 360/BL and the tip vortex boundary. If XIOPT = 0, a linear vortex sheet is established between (1) and (2) above.
603	A	A	Curve fit constant, A, in the tip vortex radial coordinate equation.
604	XAMBDA	LAMBDA	Curve fit constant, XAMBDA, in the tip vortex radial coordinate equation.
605	PHINPO	VORTEX SHEET (R = 0), PHI3	Wave azimuth angle, PHINPO, that separates the axial velocity regions AK20 and AK30 for the vortex sheet extension to $\bar{r} = r/R = 1$, deg (see Fig. 30).

606	PHINP1	VORTEX SHEET (R = 1), PHI3	Wake azimuth angle, PHINP1, that separates the axial velocity regions AK21 and AK31 for the vortex sheet extension to r/R = 1, deg (see Fig. 30).
610	AK1T	TIP FILAMENTS, K1	Axial velocity of the tip vortex between the blade and the passage of the following blade at wake azimuth 360/BL (nondimensionalized by blade tip speed).
611	AK2T	TIP FILAMENTS, K2	Axial velocity of the tip vortex after the passage of the following blade at the wake azimuth 360/BL (nondimensionalized by blade tip speed).
612	AK10	VORTEX SHEET (R = 0), K1	Axial velocity of the vortex sheet extension to the center of rotation in the wake azimuth region between the blade and the passage of the following blade at the wake azimuth 360/BL (nondimensionalized by blade tip speed).
613	AK20	VORTEX SHEET (R = 0), K2	Axial velocity of the vortex sheet extension to the center of rotation in the wake azimuth region between the passage of the following blade at the wake azimuth 360/BL and the wake azimuth PHINP0 (nondimensionalized by blade tip speed).
614	AK30	VORTEX SHEET (R = 0), K3	Axial velocity of the vortex sheet extension to the center of rotation following the wake azimuth PHINP0 (nondimensionalized by tip speed).
615	AK11	VORTEX SHEET (R = 1), K1	Axial velocity of the vortex sheet extension to $\bar{r}$ = r/R = 1 in the wake azimuth region between the blade and the passage of the following blade at the wake azimuth 360/BL (nondimensionalized by blade tip speed).

616	AK21	VORTEX SHEET (R = 1), K2	Axial velocity of the vortex sheet extension to $\bar{r} = r/R = 1$ in the wake azimuth region between the passage of the following blade at the wake azimuth 360/BL and the wake azimuth PHINP1 (nondimensionalized by blade tip speed).
617	AK31	VORTEX SHEET (R = 1), K3	Axial velocity of the vortex sheet extension to $\bar{r} = r/R = 1$ following the wake azimuth PHINP1 (nondimensionalized by blade tip speed).
619	TRUNCT		Angle of roll-up of tip vortex filaments with respect to the blade, deg. Tip vortex filaments beyond this wake azimuth angle are all assigned coordinates equivalent to the outermost tip filament, thereby simulating the roll-up of the tip vorticity into a concentrated tip vortex. TRUNCT/DPSI must be an integer. A typical value of TRUNCT is 30.0. If no roll-up is desired set TRUNCT = 0.0.
620	ROLLUP		Starting value of number of filaments to roll-up in tip vortex (at roll-up angle TRUNCT).
621	CDDATA		Starting at location 621 the number of Mach number curves is input followed by the value of the first Mach number and the number of pairs of points for that Mach number curve. Following these input items the values of the angle of attack are input in a monotonically increasing sequence, followed by the corresponding sequence of values of drag coefficient. For the next set of curves we start again by inputting the number of pairs of points, the Mach number value, and proceed as before until the data is exhausted.

1221	PRNTX	These parameters are used for additional printout. Set PRNTX = 1.0 for additional printout. Normally PRNTX = 0.0. See further information on PRNTX array at the end of this Appendix.
600	CASE	This is an option control for multiple cases. CASE = 1.0 implies that additional cases follow; CASE = 0.0 or blank implies that there are no further cases. In all cases card columns 1 and 2 contain -1.

2. DESCRIPTION OF PROGRAM PRINTOUT

The program printout is broken into three major divisions. The first is the printout of pertinent program input parameters. The second is the printout of important computation parameters. The third is the printout of performance parameters. The following list provides a supplemental description of the program output. The list follows the order of the actual program output.

PROGRAM TITLE AND CASE TITLE

PROGRAM INPUT LABEL

PRINTOUT OF IMPORTANT INPUT PARAMETERS TO PROGRAM (For a complete printout of input items set PRNTX (9) = 1.0)

MESSAGES PERTAINING TO CONVERGENCE OF LIFTING LINE VORTICITY CALCULATION

PROGRAM OUTPUT LABEL AND ADDITIONAL DESCRIPTION OF OUTPUT ITEM

SPANWISE INPUT REFERENCE STATION (in percent)

AXIAL VELOCITY COMPONENT AT INPUT REFERENCE STATIONS (computed with UARL lifting line program)

CIRCUMFERENTIAL VELOCITY COMPONENT AT INPUT REFERENCE STATIONS (computed with UARL lifting line program)

RADIAL VELOCITY COMPONENT AT INPUT REFERENCE STATIONS (computed with UARL lifting line program)

TIP RADIAL VELOCITY (computed with UARL lifting line program)

PHI CALCULATED AT STATION R PHI = $\tan^{-1}(V_R/V_T)$

AXIAL VELOCITY AT TIP STATIONS (computed with UARL lifting line program)

CIRCUMFERENTIAL VELOCITY AT TIP STATIONS (computed with UARL lifting line program)

Y-TIP COORDINATE (of tip stations)

Z-TIP COORDINATE (of tip stations)

COSINE OF THETA

THETA-RADIANS

BETA-RADIANS BETA = $\tan^{-1}(V_A/V_T)$

PHI CALCULATED AT Y AND Z TIP COORDINATES

DISTANCE ALONG REFERENCE LINE (of aerodynamic tip)

AXIAL DISTANCE (of aerodynamic tip)

ANGLE IN THETA DIRECTION (of aerodynamic tip)

DEMARCATION LINE OF TIP GRID AREA Radial distance of demarcation line from axis of reference

REFERENCE LINE STATION Radial coordinates of points of computation grid

CHORD GRID Chordwise distances from reference line of points of computation grid

X-COORDINATE (Axial coordinate of computation grid)

ANGLE THETA Circumferential coordinates of points of computation grid

RADIAL STATION Radial coordinates of field points

CHORD DISTANCE Chordwise distances from reference line of field points

AXIAL DISTANCE Axial coordinates of field points

ANGLE THETA Circumferential coordinates of field points

Y-COORDINATE (of field points - Cartesian coordinates)

Z-COORDINATE (of field points - Cartesian coordinates)

INPUT ANGLE OF ATTACK DISTRIBUTION in radians

ANGLE OF ATTACK DISTRIBUTION AT FIELD DATA POINTS

MESSAGES PERTAINING TO CONVERGENCE OF LIFTING SURFACE VORTICITY CALCULATION

RADIAL COMPONENTS OF VORTICITY Circulation strengths of radial vortex filaments

CIRCUMFERENTIAL COMPONENTS OF VORTICITY Circulation strengths of chordwise vortex filaments

PRESSURE DISTRIBUTION Distribution of pressure difference over blade surface

PRESSURE DISTRIBUTION - CHORD CORRECTION Distribution of pressure difference over blade surface with chordwise compressibility correction

PRESSURE DISTRIBUTION - STREAM CORRECTION Distribution of pressure difference across blade surface with streamwise compressibility correction

DELTA CP CALCULATION - INCOMPRESSIBLE Distribution of coefficient of pressure difference across blade surface with no correction for compressibility

DELTA CP CALCULATION - CHORD CORRECTION Distribution of coefficient of pressure difference across blade surface with chordwise compressibility correction

DELTA CP CALCULATION - STREAM CORRECTION Distribution of coefficient of pressure difference across blade surface with streamwise compressibility correction

THRUST PER BLADE, LBS

INDUCED TORQUE PER BLADE, FT-LBS

THRUST, LBS

COEFFICIENT OF THRUST

INDUCED TORQUE, FT-LBS

POWER, FT-LBS/SEC

COEFFICIENT OF POWER

HORSEPOWER

FIGURE OF MERIT

PROFILE TORQUE, FT-LBS

TOTAL TORQUE, FT-LBS

COEFFICIENT OF TORQUE

3. COMPUTER SYSTEM INFORMATION AND PROGRAM STRUCTURE

The UARL Lifting Surface Program is written in FORTRAN IV computer language for use on the C.D.C. 6600 computer. The program requires 240 K octal words of storage allocation.

The structure of the program is schematically represented in the overlay diagram of Fig. 31. The complexity of the calculations has necessitated using a modular approach to structuring the program. The first module (0,0) contains the initial routine (MAIN) and assorted general purpose routines that are used by the modules in the overlays. The function of the second module (1,0) is the calculation of the components of velocity (VELCAL) and the lattice grid (GRIDCL) and it contains other necessary subroutines. The third module (2,0) contains the vorticity calculation subroutine (VORLAT) and other subroutines necessary for this calculation. The last module (3,0) contains the performance calculation subroutines that are controlled by one major subroutine (PERFRM). Note that the "submodules" (1,1) and (1,2) are regarded as parts of module (1,0), and similarly (2,1), (2,2), and (2,3) are regarded as parts of module (2,0). A brief description of each subroutine is presented below.

INITIAL PROGRAM MAIN - This routine controls the flow of the entire program calculations.

SUBROUTINE TIMEPR - This subroutine calls the system routine SECOND which obtains the time traps and prints them out at the end of each case.

SUBROUTINE COEXTR - This subroutine does a linear extrapolation of input data for a specified end point of the curve.

SUBROUTINE XNTERP - This subroutine returns an interpolated curve value and its slope, given the abscissa and the curve data. The interpolation scheme uses a modified parabolic technique. A minimum of four coordinates of data points are required before the subroutine can be properly used.

SUBROUTINE LADDER - This subroutine reads in the LOADER format input data. See program input for a detailed account of the card format.

PROGRAM VELCAL - This program controls the calculation of the velocity components and the Lifting Surface Lattice Grid. The velocity components are calculated from a blade induced velocity distribution due to a lifting line.

SUBROUTINE GRIDCL - This subroutine calculates the aerodynamic tip of the propeller and uses this result to calculate the Lifting Surface Lattice Grid.

SUBROUTINE SUBSEQ - This subroutine calculates a strictly monotonic sequence from a given input sequence such that all elements of the sequence are less than or equal to an input tip value.

SUBROUTINE EXTRAP - This subroutine performs a double parabolic interpolation on given input curves.

SUBROUTINE GASEI2 - This subroutine solves the system of equations that define the lifting line vorticity field using a modified Gauss-Seidel technique. When the percentage difference of the sums of two successive solutions is within a given tolerance, convergence is indicated and the solution stops.

PROGRAM WAKEC2 - This program calculates the final wake coordinates (axial and radial) used in the lifting line calculation of the velocities.

SUBROUTINE RWZWA2 - This subroutine calculates the initial set of coordinates that define the wake of the lifting line.

PROGRAM GCOEF2 - This program calculates the geometric coefficients associated with the lifting line wake from the wake coordinates.

PROGRAM VORLAT - This program calculates either the camber distribution of a particular propeller or its vorticity field depending on the value of the problem parameter. A subsidiary calculation is the creation of the field data coordinates.

FUNCTION FLDPT - This function returns a mean coordinate, given four corner coordinates.

SUBROUTINE DISCAL - This subroutine computes important parameters necessary for the calculation of the perpendicular distance between a point and a line.

PROGRAM WAKECL - This program calculates the final wake coordinates (axial and radial) used in the lifting surface calculation of the velocities.

SUBROUTINE RWZW - This subroutine calculates the initial set of coordinates that define the wake of the lifting surface.

PROGRAM GCOEFF - This program calculates the geometric coefficients associated with the lifting surface wake from the wake coordinates.

PROGRAM GAUSEI - This subroutine solves the system of equations that define the lifting surface vorticity field using a modified Gauss-Seidel technique. The same convergence as GAUSEI2 is used in this routine.

PROGRAM PERFRM - This program controls the calculation and printout of the performance parameters.

FUNCTION SIMINI - This function is a general purpose integration routine that uses Simpson's 1/3 rule.

FUNCTION FEVAL - This function calculates an integrand used in the SIMINI integration routine.

FUNCTION INTERP - This function performs a bivariate quasi-parabolic interpolation of drag data, given a particular angle of attack and Mach number.

4. DESCRIPTION OF PRNTX ARRAY

There are 13 variables in the PRNTX Array.

(1) Circulation calculated using the UARL lifting line program (GASEI2).

(2) Wake calculation coefficient printout (RWZWA2).

(3) Circulations calculated for Lifting Surface (GAUSEI).

(4) Wake coordinates for lifting line calculation of velocity (WAKEC2).

(5) Printout of geometric coefficients, final circulations, and velocities at segment centers (VELCAL).

(6) Printout of wake coefficients for lifting surface (RWZW).

(7) Wake coordinates for lifting surface wake (WAKECL).

(8) Additional performance printout (PERFRM).

(9) All input (LIFTSR).

(10) Additional grid coordinate printout (GRIDCL).

(11) (a) Input coordinate grid (VORLAT).

(b) Last psuedo field data coordinate used for interpolation (VORLAT).

(c) Geometric coefficients associated with wake of propeller.

(d) Vector coefficients associated with blade vorticity field and component parameters.

(12) (a) Modified coefficients. $\sum_i a_i \Gamma_r + \sum_i b_i \Gamma_s \Longrightarrow \sum a_i' \Gamma_r$ (VORLAT)

(b) Augmented matrix.

(c) Maximum circulations allowed in iteration scheme.

(d) Dependent parameters.

(13) (a) Residue printout.

(b) Blade induced velocities u_r, u_s (VORLAT).

APPENDIX III

GRID SIZE SENSITIVITY

In the course of this investigation it was found that the predicted propeller performance is dependent to a greater or lesser degree on the geometry and size of the computation grid. It is axiomatic that the results of any numerical computation are valid only if they are independent of the locations of the grid points leading to their evaluation. Hence, an examination was made of this dependence and on the sensitivity of the results of the computation to variations in grid geometry. At the conclusion of this sensitivity study a grid geometry was chosen to have the coarsest possible grid which yielded results consistent with computations from finer grids. This procedure is described below.

The blade vortex-lattice configuration used herein is shown schematically in Fig. 8. A more detailed version of this lattice system is shown in Fig. 32. Here the blade has been idealized to a rectangular planform, and no wake filaments are included. In the chordwise direction the midchord line separates the five-segment forward portion from the four-segment aft portion. In other words, there are a total of 10 chordwise grid points, 6 (including the midchord) in the forward half and 4 in the rear half. This arrangement, which was maintained for the entire study, provided a slightly finer mesh over the leading-edge region. In the spanwise direction a variable number and location of grid points could be used, up to a maximum of 20. Provision has been made in the computer program for the user to choose the location of the demarcation line and the number of segments inboard and outboard of this demarcation line. In Fig. 32 there were 4 inboard segments, 5 outboard segments, and the demarcation line was located at $r/R = 0.8$. A notation can be devised here, in terms of grid points, which will be useful in the work that follows. In this figure the spanwise grid can be completely defined by specifying the station number of the demarcation line, 5, the radius ratio at that point, 0.8, and the total number of grid points, 10, and the notation for this case is $5\text{-}(.8)_{10}$. A schematic illustration of all of the grid configurations analyzed is shown in Fig. 33. The circled points represent grid locations and the vertical line for each grid system represents the demarcation line. At the left of each grid system is the notation described above.

Some initial runs of the Canadair RAA-240-108 propeller were made for the grid systems $5\text{-}(.8)_{10}$ and $5\text{-}(.7)_{10}$. These computations were carried out at a collective pitch of $\alpha_{75} = 14$ deg for the incompressible lift-curve slope distribution a_2 listed in Table I. The trends, as shown in Fig. 34, were very revealing in that for a specific chordwise location the predicted spanwise distribution of pressure difference coefficient, ΔC_p, for each

grid system differed from the other chiefly at the demarcation line. Changes were also seen in the predicted coefficients of thrust and torque as the demarcation line was shifted for this 10 x 10 grid system. Hence, it was decided to run the entire series of grid systems shown in Fig. 33.

The results of this study are summarized in Fig. 35 in which C_T and C_Q are plotted versus the station number of the demarcation line. The study concentrated primarily on the case in which the demarcation line was located at 60% span (circled points) and a trend curve was drawn through these points which shows that the thrust, in particular, has a tendency to converge as station number increases. For constant demarcation line location, an increase in station number is equivalent to increasing the density of the grid (see Fig. 33). Hence we have the reasonable result that a sufficiently dense grid will yield convergent results. For comparison, horizontal bands have been included in Fig. 35 to indicate the range of experimental data for this operating condition. However, increasing the density of the outboard grid appears to have a detrimental effect, as seen by the circle, square, and triangular point plotted at station 8. These are, respectively, configurations $8\text{-}(.6)_{16}$, $8\text{-}(.7)_{16}$, and $8\text{-}(.8)_{16}$, and it is seen in Fig. 33 that the third configuration has twice the grid density over the outboard 80% of the span as the first. Thus it appears that we have the further restriction that we need a sufficiently dense grid that is moderately balanced between inboard coarse and outboard fine grids. In view of the close agreement between the $8\text{-}(0.6)_{16}$ and the $10\text{-}(.6)_{20}$ grid configurations, the former was chosen for all other runs since it represents the least computer time for reasonable accuracy.

APPENDIX IV

APPLICATION OF LIFTING SURFACE THEORY TO NOISE PREDICTION FOR STATICALLY OPERATING PROPELLERS

The continuing emphasis on reducing the noise from aircraft requires that the radiated noise field of an aircraft be considered in its design. In predicting the noise field of a statically operating propeller the accuracy with which the disturbance pressure distribution in the near and far fields is computed depends strongly on the aerodynamic blade loads. In this connection the lifting surface theory for statically operating propellers provides an appropriate method for computing the distributed aerodynamic blade loads.

The noise from a statically operating propeller can be divided into three categories: loading noise, thickness noise, and vortex noise. We will study the first case only in which the disturbance pressures are due directly to the blade aerodynamic loading. To an observer rotating in a reference frame fixed to the rotating propeller the N_B blades produce a steady disturbance pressure field which has N_B peaks around the circumference. To a stationary observer the disturbance pressure field of any one blade is rotating with the propeller at Ω radians per second and the disturbance pressure field at the observer due to all N_B blades oscillates with a fundamental frequency of $N_B \Omega/2\pi$ cps. This oscillating pressure field is the harmonic rotational noise due to blade loading and may be Fourier analyzed to determine the pressure amplitude of each harmonic of the fundamental frequency $N_B \Omega/2\pi$ cps (see Ref. 24).

The existing formulations that treat the propeller loading noise prediction problem are based on an array of non-steady point forces in the propeller disk representing the blade thrust and torque forces (Ref. 25). The non-steady point forces are distributed over the entire propeller disk. They are zero everywhere except at the local, instantaneous projection of the blades on the disk. Therefore each force acts as a series of pulses with a fundamental frequency of $N_B \Omega/2\pi$ cps and a pulse width proportional to the blade chord. The assumptions usually made are (a) that the blade loading is constant over the chord or (b) the thrust and torque are distributed over a zero blade width (see Refs. 24 and 25). This latter assumption implies a Dirac delta function behavior in the blade loading. Expressions are derived in Ref. 24 for the pressure field at a field point for the mth harmonic. The pressure is broken up into two parts, namely, that due to thrust forces and that due to torque forces. The respective equations for pressure due to thrust force p_T and pressure due to torque forces p_Q for any given harmonic, m, have the following form (see Ref. 24)

$$p_T = \frac{1}{4\pi^2} \int_0^R \int_0^{2\pi} \frac{dT}{dr} e^{im N_B (\Omega t - \theta)} \frac{\partial}{\partial x} \left(\frac{e^{-i\sigma m N_B \Omega / c}}{\sigma} \right) d\theta \, dr \qquad (71)$$

$$p_Q = \frac{1}{4\pi^2} \int_0^R \int_0^{2\pi} \frac{1}{r} \frac{dQ}{dr} e^{im N_B (\Omega t - \theta)} \frac{1}{r} \frac{\partial}{\partial \theta} \left(\frac{e^{-i\sigma m N_B \Omega / c}}{\sigma} \right) d\theta \, dr \qquad (72)$$

where σ is the distance between the blade and the external field point and c is the speed of sound. The formulas given in Eqs. (71) and (72) provide the relationship between p_T, p_Q and dT/dr, dQ/dr. The functions dT/dr and dQ/dr depend on r only and are valid only for constant chordwise pressure loading on the blade.

In the general case of non-constant pressure loading, equations corresponding to Eqs. (71) and (72) can be derived for p_T and p_Q. The formulation is similar to that of Garrick and Watkins in Ref. 24 and will be given in what follows.

In the derivation of the lifting surface theory the basic frame of reference was a Cartesian set of axes which were fixed on the rotating blades. In the formulation of the noise prediction method, however, it is more convenient to use a fixed Cartesian frame of reference (see Fig. 36). The propeller disk is oriented so that the axis passing through the center of the disk coincides with the x-axis and the propeller rotates in the yz plane with positive values of x corresponding to points behind the propeller disk in the wake. The propeller will be rotating clockwise with angular velocity Ω as seen by an observer upstream of the propeller looking aft toward the wake. Each element of the propeller is acted on by the surface pressure distribution and this may be resolved into a thrust force in the direction of the x-axis and a tangential force associated with the torque. The points of application of these forces are imagined to lie in a single plane designated as the propeller disk.

The reaction of the propeller that is exerted on the fluid medium against the thrust and torque forces will, at any instant, be replaced by fixed periodic forces acting at the propeller disk. We consider an element of the propeller at a distance r from the x-axis; let dr be its radial length and $rd\theta$ its width measured in the projection onto the plane of rotation. The force per unit area acting on this element at an instant of time t will be given by $\Delta p(r, \theta_T(r) - \theta_L(r) - \Omega t)$ where this quantity

represents the instantantaneous pressure difference across the blade at the point $(r, \theta_T(r) - \theta_L(r) - \Omega t)$. This can be found from the lifting surface theory for a statically operating propeller. The force per unit area Δp can be resolved into two forces, one in the axial direction, $-\Delta p \cos\beta$, and the other in the circumferential direction, $\Delta p \sin\beta$, where β is the angle defining the blade reference surface. This angle β is found from the UARL lifting-line program for statically operating rotors.

The elemental area of the disk with coordinates (r, θ) will experience a periodic force which can be expanded in a Fourier series. The forces $\Delta p \cos\beta$ and $-\Delta p \sin\beta$ act on the fluid during the time interval τ_1, given by

$$\tau_1 = \frac{\ell(r) \cos\beta}{r\Omega} \tag{73}$$

During the time interval τ_1 the element of the propeller disk at (r, θ) will be eclipsed by the blade and this eclipse will occur again at time $t = \tau_2 = 2\pi/N_B\Omega$ when the leading edge of the next blade reaches the element. The forces $\Delta p \cos\beta$ and $-\Delta p \sin\beta$ then can be represented by F_1 and F_2 where

$$F_1 = \begin{cases} \Delta p(r, \theta_T(r) - \theta_L(r) - \Omega t)\cos\beta, & 0 < t < \tau_1 \\ 0, & \tau_1 < t < \tau_2 \end{cases} \tag{74}$$

$$F_2 = \begin{cases} -\Delta p(r, \theta_T(r) - \theta_L(r) - \Omega t)\sin\beta, & 0 < t < \tau_1 \\ 0, & \tau_1 < t < \tau_2 \end{cases} \tag{75}$$

The functions F_1 and F_2 can be expanded in Fourier series of the form

$$F_1(t) = A_0 + \sum_{m=1}^{\infty} A_m(r,\theta)\cos mN_B(\Omega t - \theta) + \sum_{m=1}^{\infty} B_m(r,\theta)\sin mN_B(\Omega t - \theta) \tag{76}$$

$$F_2(t) = \bar{A}_0 + \sum_{m=1}^{\infty} \bar{A}_m(r,\theta)\cos mN_B\Omega t + \sum_{m=1}^{\infty} \bar{B}_m(r,\theta)\sin mN_B\Omega t \tag{77}$$

where

$$A_m = \frac{\Omega}{\pi} \int_0^{\frac{2\pi}{\Omega}} F_1(t) \cos mN_B \Omega t \, dt \tag{78}$$

$$B_m = \frac{\Omega}{\pi} \int_0^{\frac{2\pi}{\Omega}} F_1(t) \sin mN_B \Omega t \, dt \tag{79}$$

$$\bar{A}_m = \frac{\Omega}{\pi} \int_0^{\frac{2\pi}{\Omega}} F_2(t) \cos mN_B \Omega t \, dt \tag{80}$$

$$\bar{B}_m = \frac{\Omega}{\pi} \int_0^{\frac{2\pi}{\Omega}} F_2(t) \sin mN_B \Omega t \, dt \tag{81}$$

The pressure at any field point (x,y,z) associated with external periodic forces $Ae^{i\omega t}$ and $Be^{i\omega t}$ acting at the point (x_1,y_1,z_1) in the axial and circumferential directions is given in Ref. 25 by

$$f_1 = -\frac{A}{4\pi} \frac{\partial}{\partial x} \left[e^{i\omega\left(t - \frac{\bar{s}}{c}\right)} \right] \tag{82}$$

and

$$f_2 = -\frac{B}{4\pi} \frac{1}{r} \frac{\partial}{\partial \theta} \left[e^{i\omega\left(t - \frac{\bar{s}}{c}\right)} \right] \tag{83}$$

respectively, where

$$\bar{s} = \sqrt{(x - x_1)^2 + (y - y_1)^2 + (z - z_1)^2} \tag{84}$$

and ω is the frequency of the oscillating force. The general expressions for $F_1(t)$ and $F_2(t)$ can be written in a form which is convenient for the application of Eqs. (82) and (83). We have

$$F_1(t) = \text{REAL}\left\{C_0 + \sum_{m=1}^{\infty} C_m(r,\theta)\, e^{imN_B(\Omega t - \theta)}\right\} \tag{85}$$

$$F_2(t) = \text{REAL}\left\{\bar{C}_0 + \sum_{m=1}^{\infty} \bar{C}_m(r,\theta)\, e^{imN_B(\Omega t - \theta)}\right\} \tag{86}$$

where

$$C_0 = A_0 \tag{87}$$

$$\bar{C}_0 = \bar{A}_0 \tag{88}$$

$$C_m = A_m - i\, B_m \tag{89}$$

and

$$\bar{C}_m = \bar{A}_m - i\, \bar{B}_m \tag{90}$$

The axial and circumferential forces acting on the fluid at the element $rdrd\theta$ of the disk can be written, for any given harmonic m, in the form

$$- C_m\, e^{imN_B(\Omega t - \theta)}\, rdrd\,\theta \tag{91}$$

and

$$- \bar{C}_m\, e^{imN_B(\Omega t - \theta)}\, rdrd\,\theta \tag{92}$$

respectively. The differential pressures at any field point (x,y,z) due to these forces are given by dp_T and dp_Q respectively where

$$dp_T = -\frac{\perp}{4\pi}\, C_m\, e^{imN_B(\Omega t - \theta)}\, rdrd\,\theta\, \frac{\partial}{\partial x}\left[e^{-imN_B\,\Omega\,\frac{\bar{s}}{c}}\right] \tag{93}$$

and

$$dp_Q = -\frac{1}{4\pi}\,\bar{C}_m\, e^{imN_B(\Omega t-\theta)}\, dr\,d\theta\,\frac{\partial}{\partial\theta}\left[e^{-imN_B\Omega\frac{\bar{s}}{c}}\right] \tag{94}$$

The total oscillating pressure p for any given harmonic m is obtained from Eqs. (93) and (94) as the sum of the pressures due to thrust forces p_T and the sum of the pressures due to torque forces p_Q. We have

$$p = p_T + p_Q \tag{95}$$

where

$$p_T = \frac{1}{4\pi}\int_0^R\int_0^{2\pi} C_m e^{imN_B(\Omega t-\theta)}\frac{\partial}{\partial x}\left[e^{-imN_B\Omega\frac{\bar{s}}{c}}\right] r\,dr\,d\theta \tag{96}$$

and

$$p_Q = \frac{1}{4\pi}\int_0^R\int_0^{2\pi} \bar{C}_m\, e^{imN_B(\Omega t-\theta)}\frac{\partial}{\partial\theta}\left[e^{-imN_B\Omega\frac{\bar{s}}{c}}\right] dr\,d\theta \tag{97}$$

With a knowledge of Δp the coefficients C_m and $\bar{C}_m$ can be found and the acoustic pressure field due to blade loading can be found from Eqs. (95), (96), and (97).

TABLE I

Parameter Values for Canadair Propeller RAA-240-108

(Hartzell Model 10178)
(Input Quantities)

Number of Blades = 4
Hub Radius = 0.45 ft
Tip Radius = 3.00 ft
Tip Speed = 757 ft/sec

Blade Station	Blade Radius r (ft)	Radius Ratio r/R	Blade Chord ℓ (ft)	Blade Pitch Angle[1] α (deg)	Blade Pitch Increment[2] $\Delta\alpha$ (deg)	Incompressible Lift Curve Slope, a_1[3] (rad^{-1})	Incompressible Lift Curve Slope, a_2[4] (rad^{-1})
1	0.45	0.15	0.272	39.27		1.90	6.28
2	1.05	0.35	0.444	30.18	24.43	5.87	6.28
3	1.65	0.55	0.574	19.88	17.22	7.00	6.28
4	2.25	0.75	0.624	12.00	8.80	7.09	4.59
5	2.40	0.80	0.630	10.49	5.39	7.25	4.48
6	2.55	0.85	0.632	9.58	3.18	6.51	3.51
7	2.70	0.90	0.638	7.76	2.32	5.12	3.47
8	2.85	0.95	0.646	6.55	0.76	3.02	2.13
9	2.94	0.98	0.648	5.33	-4.06	1.52	1.49
10	3.00	1.00	0.652	5.03	-5.54	0.51	1.51

(Continued)

TABLE I - Continued

Notes:

(1) α is the blade pitch angle relative to the plane of rotation for a collective pitch at the 3/4 radius station of α_{75} = 12 deg. This distribution is used in the lifting surface portion of the computer program.

(2) $\Delta\alpha$ is the sum of the blade pitch increment angle relative to the blade pitch angle at the 3/4 radius station and the zero lift offset angle. It is introduced at the center of each input segment (note the position of each tabular value). This distribution is used in the lifting line portion of the computer program to compute the inflow and wake parameters.

(3) Lift curve slope from the Hamilton Standard evaluation of this propeller blade (see Fig. 13).

(4) Lift curve slope from Canadair report, Ref. 21, with the restriction that $(dC_L/d\alpha)_{i.c} \leq 2\pi$ (see Fig. 13).

TABLE II

Parameter Values for Canadair Propeller 240-3A5

(Input Quantities)

Number of Blades = 4
Hub Radius = 0.375 ft
Tip Radius = 2.500 ft
Tip Speed = 850 ft/sec

Blade Station	Blade Radius r (ft)	Radius Ratio r/R	Blade Chord ℓ(ft)	Blade Pitch Angle(1) α(deg)	Blade Pitch Increment(2) $\Delta\alpha$(deg)	Incompressible Lift Curve Slope, a (rad^{-1})
1	0.375	0.150	0.320	47.50	28.40	3.34
2	0.781	0.313	0.320	29.50	15.82	6.60
3	1.188	0.475	0.320	18.50	7.83	7.47
4	1.594	0.637	0.320	12.50	4.29	7.90
5	2.000	0.800	0.320	9.50	2.90	8.29
6	2.100	0.840	0.320	8.00	0.44	7.73
7	2.200	0.880	0.320	5.00	-3.02	6.94
8	2.300	0.920	0.320	0.50	-8.47	5.42
9	2.400	0.960	0.320	-5.00	-12.46	3.27
10	2.500	1.000	0.320	-7.00		0.60

Notes:

(1) See Note(1) on Table I
(2) See Note(2) on Table I

TABLE III

Parameter Values for HSD Propeller 212X-16

(Input Quantities)

Number of Blades = 4
Hub Radius = 0.375 ft
Tip Radius = 2.500 ft
Tip Speed = 850 ft/sec

Blade Station	Blade Radius r (ft)	Radius Ratio r/R	Blade Chord ℓ (ft)	Blade Pitch Angle(1) α(deg)	Blade Pitch Increment(2) $\Delta\alpha$(deg)	Incompressible Lift Curve Slope, a (rad^{-1})
1	0.375	0.150	0.580	37.00	22.50	5.40
2	0.781	0.313	0.572	28.50	14.44	6.74
3	1.188	0.475	0.564	20.60	9.00	7.01
4	1.594	0.637	0.550	14.00	3.25	6.96
5	2.000	0.800	0.524	8.25	0.34	7.11
6	2.100	0.840	0.516	7.00	-0.59	6.68
7	2.200	0.880	0.500	6.00	-1.89	5.97
8	2.300	0.920	0.490	5.00	-2.69	4.77
9	2.400	0.960	0.474	4.00	-2.51	2.98
10	2.500	1.000	0.456	3.50		0.50

Notes:

(1) See Note (1) on Table I
(2) See Note (2) on Table I

TABLE IV

Wake Velocity Parameters

Propeller	α_{75}	k_1	k_2
RAA-240-108	12	-0.0349	-0.1169
	14	-0.0480	-0.1300
	16	-0.0603	-0.1418
240-3A5	10	-0.0214	-0.1454
	12	-0.0331	-0.1570
	14	-0.0428	-0.1664
212X-16	10	-0.0212	-0.1027
	12	-0.0442	-0.1262
	14	-0.0587	-0.1403

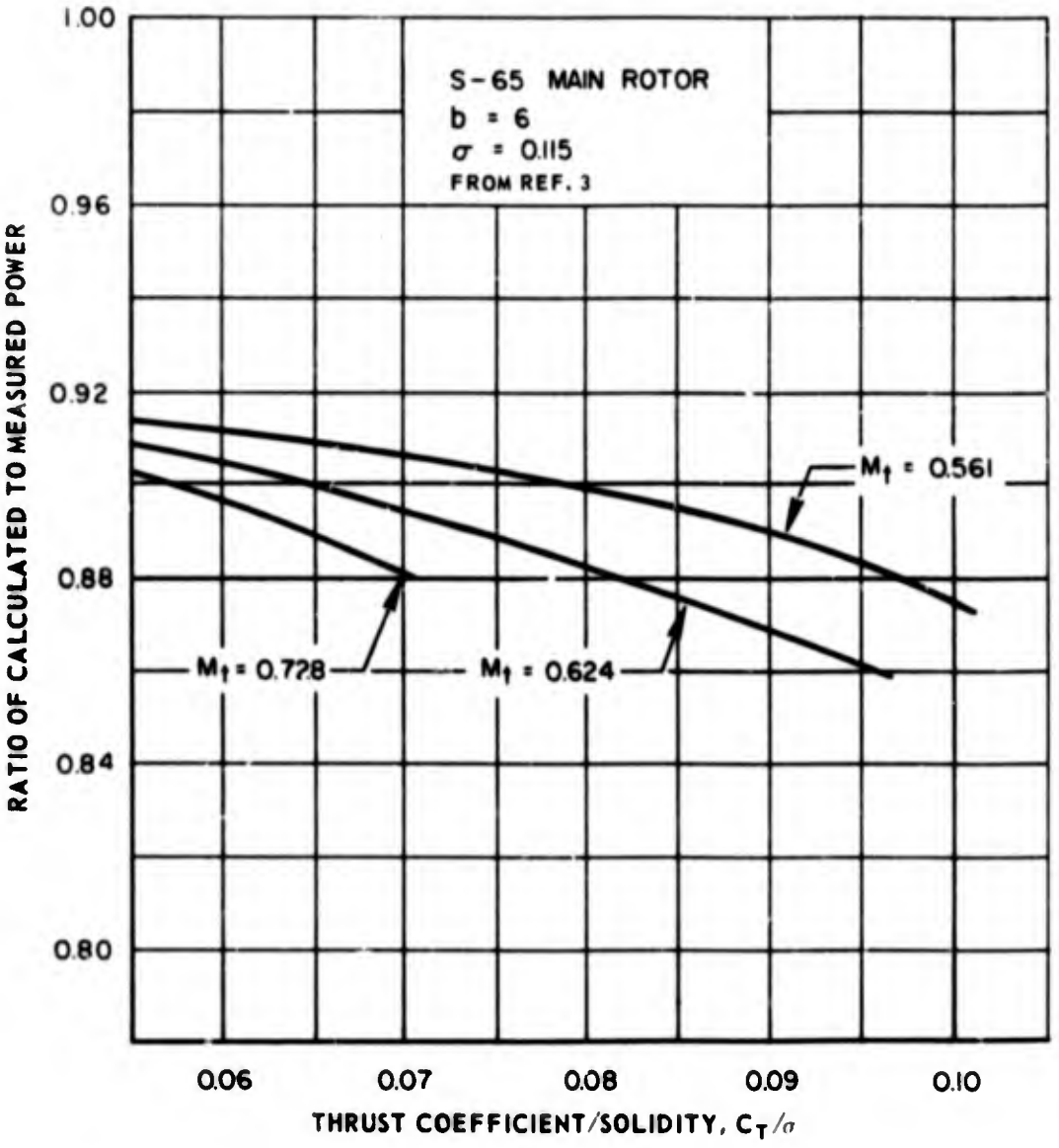

FIGURE 1. SENSITIVITY OF PREDICTED STATIC PERFORMANCE TO TIP MACH NUMBER – GOLDSTEIN–LOCK METHOD

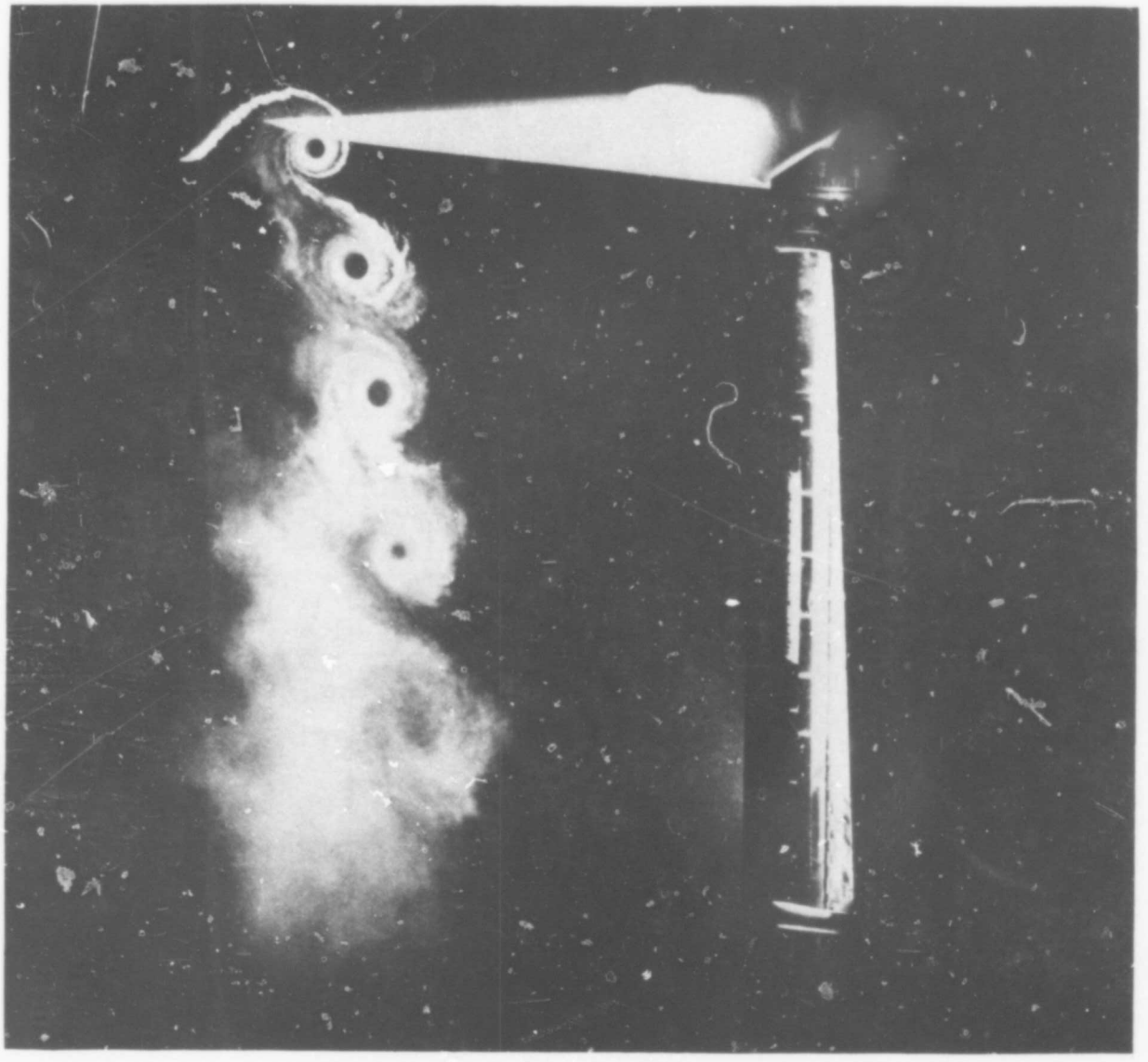

FIGURE 2. SMOKE PICTURE OF TIP VORTEX (FROM REF. 4)

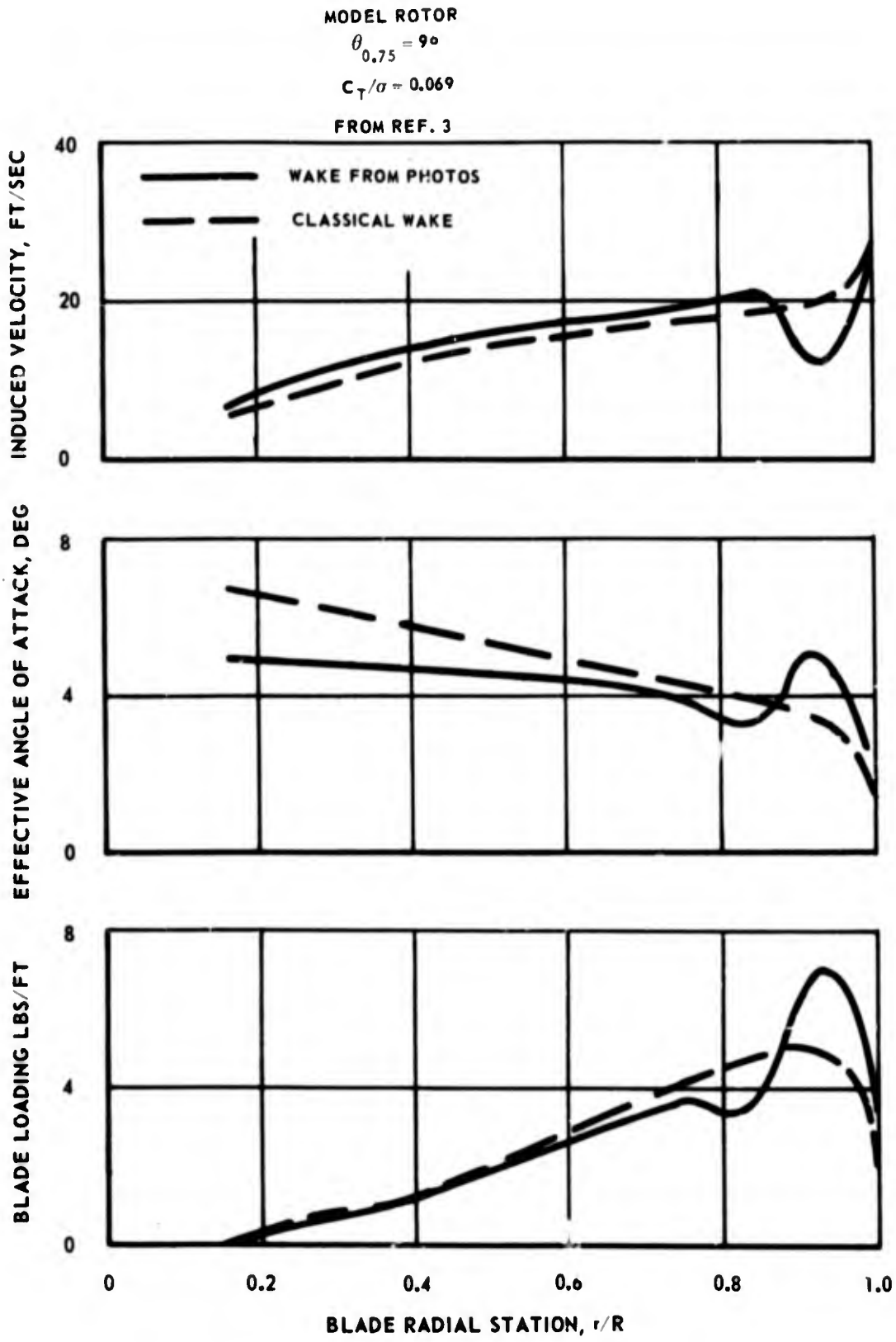

FIGURE 3. THEORETICAL DISTRIBUTIONS

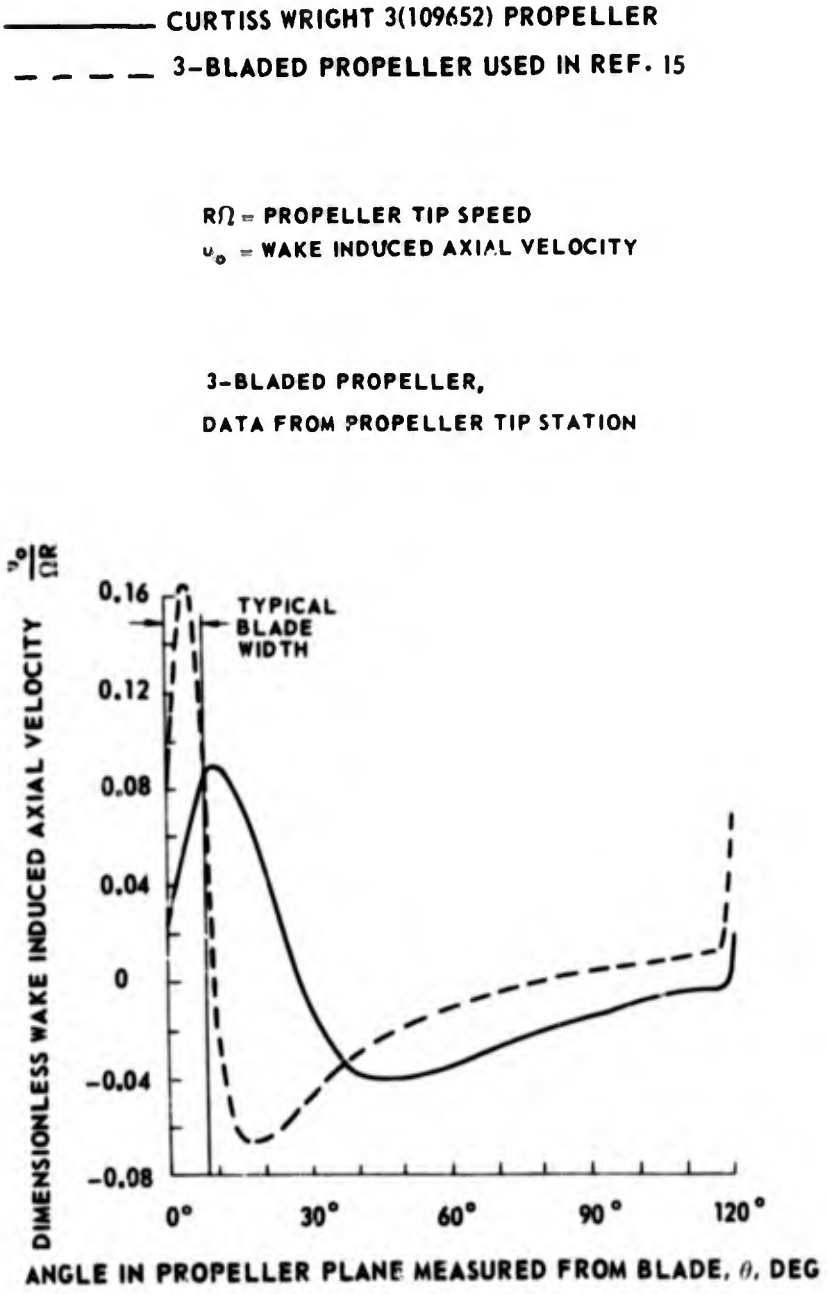

FIGURE 4. WAKE INDUCED AXIAL VELOCITY IN PROPELLER PLANE FOR TWO CIRCULATION DISTRIBUTIONS TYPICAL OF 3-BLADED PROPELLERS

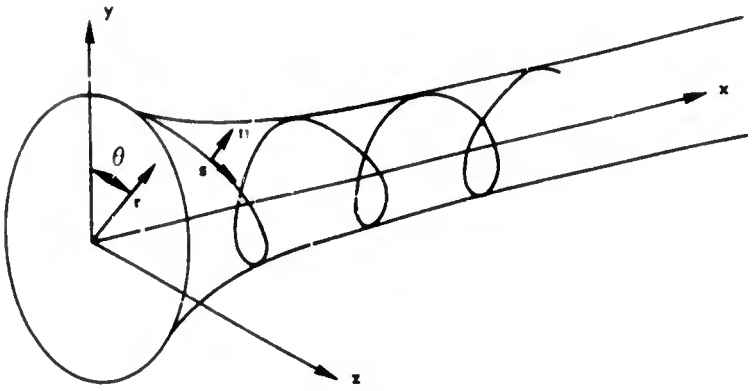

a. COORDINATE SYSTEMS

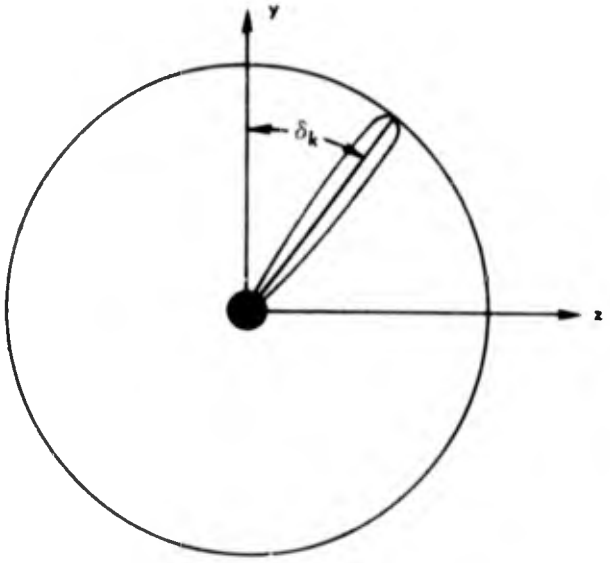

b. AZIMUTHAL LOCATION OF k^{th} BLADE

FIGURE 5. SYSTEM COORDINATES

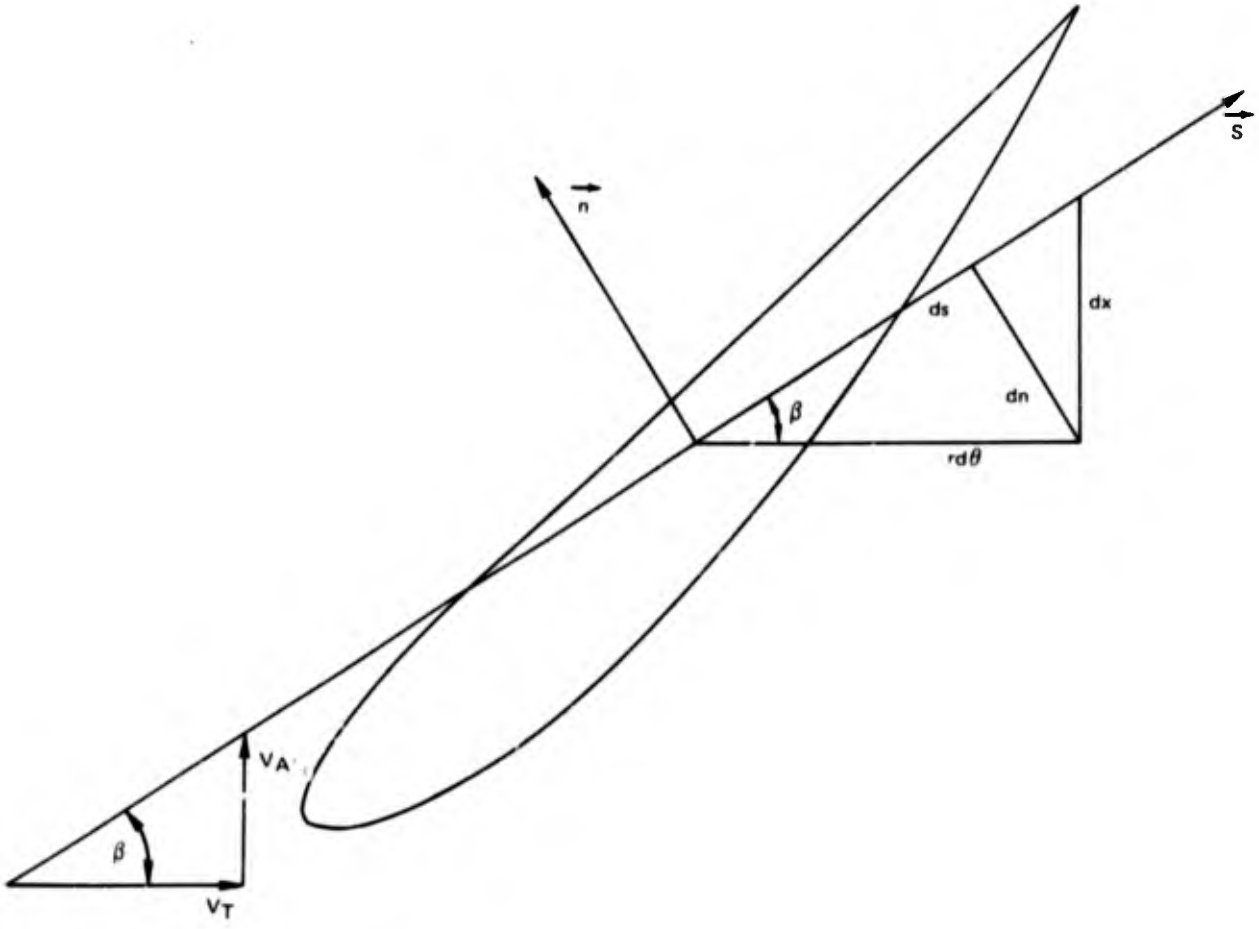

FIGURE 6. ORTHOGONAL CURVILINEAR COORDINATES AT A BLADE SECTION

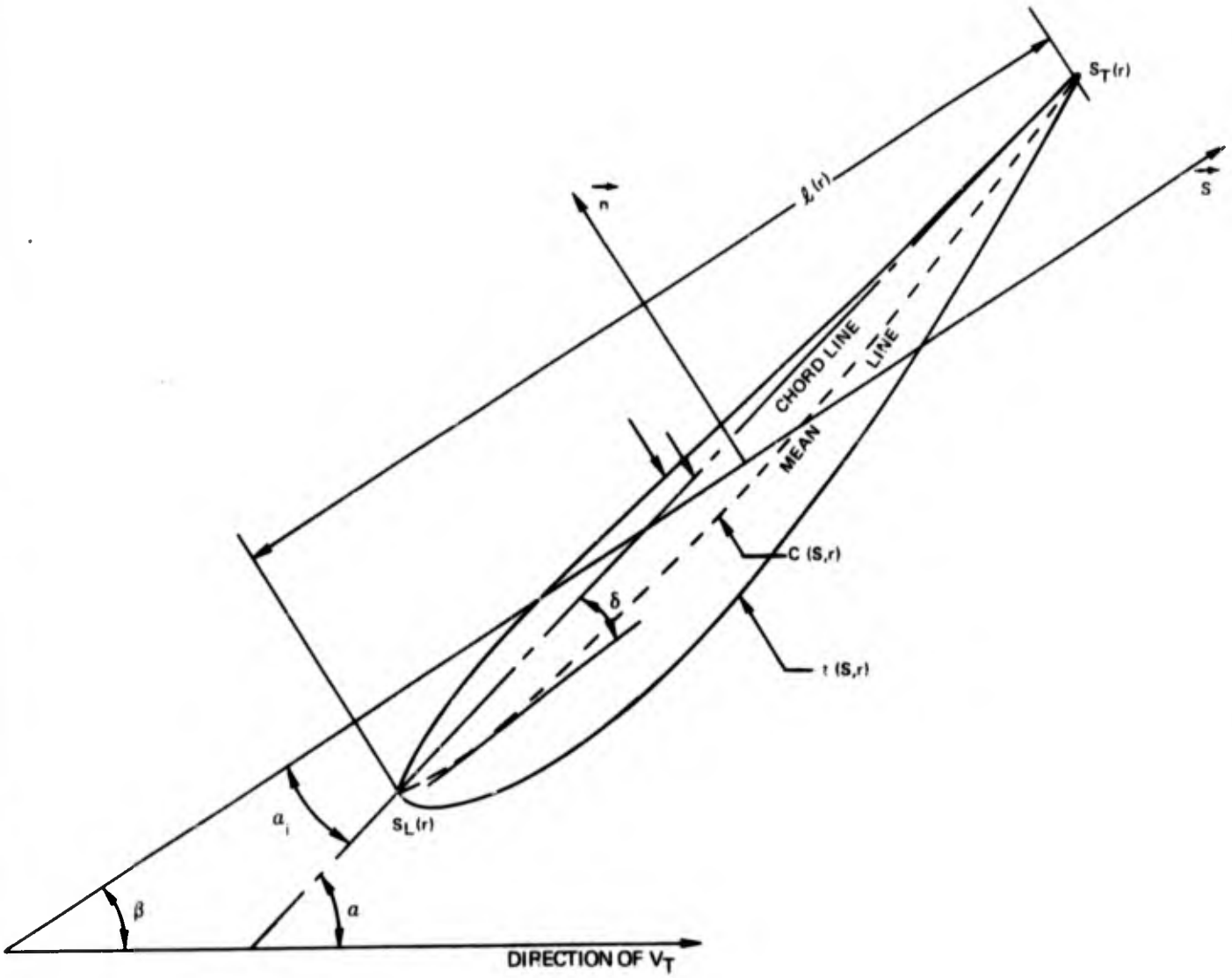

NOTE THAT $a = a_i + \beta$

NOTE FURTHER THAT a, THE BLADE PITCH ANGLE, IS INDEPENDENT OF THE VELOCITY FIELD.

FIGURE 7. BLADE SECTION PARAMETERS

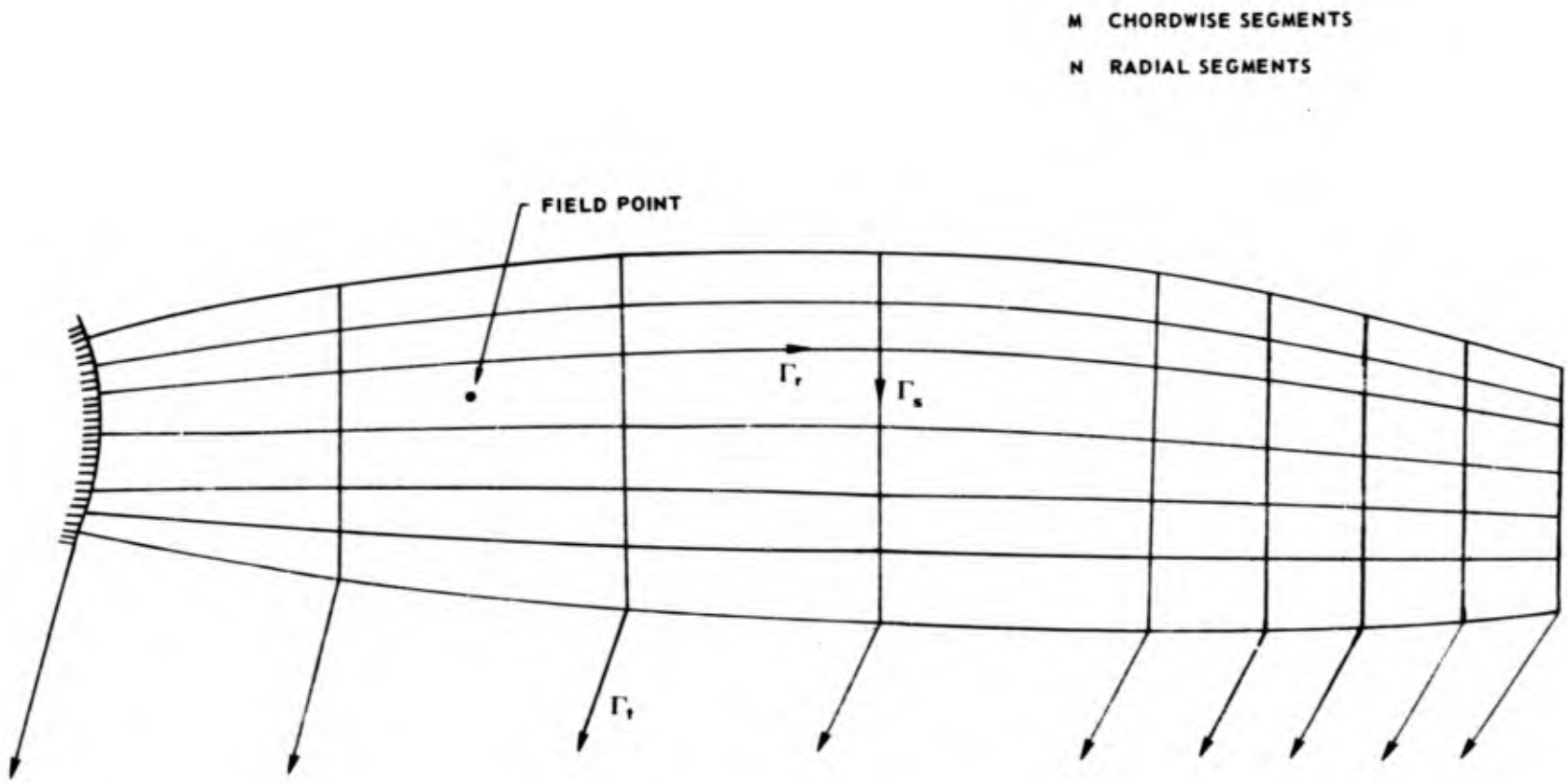

FIGURE 8. BLADE–WAKE LATTICE CONFIGURATION

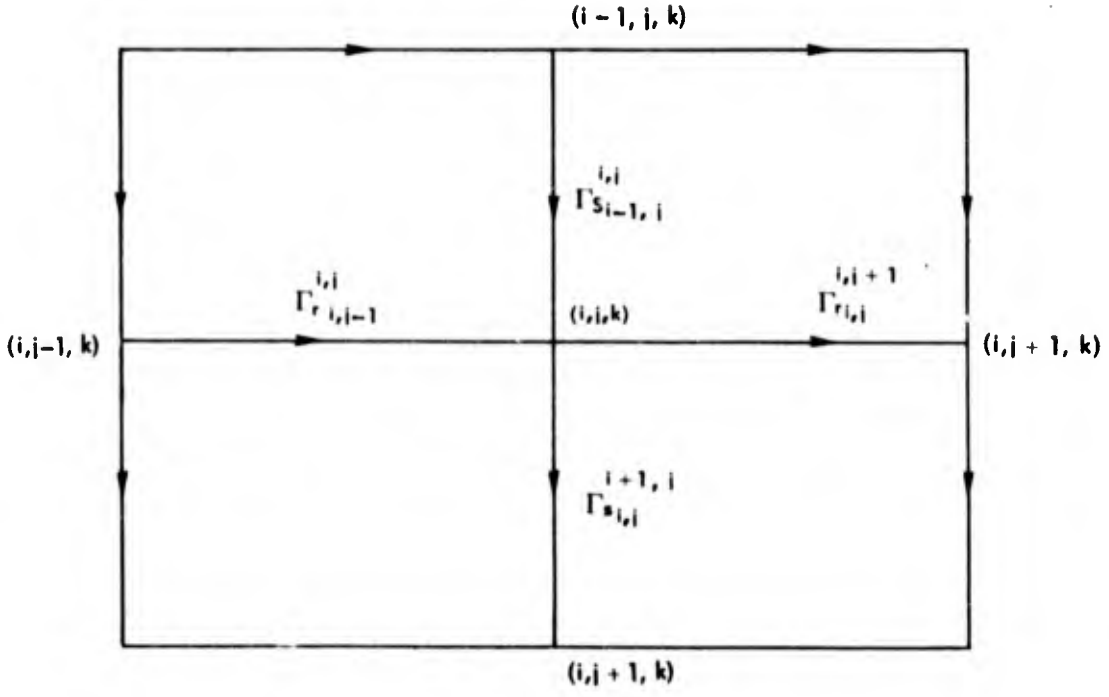

FIGURE 9. VORTEX FILAMENT CONFIGURATION AT AN INTERIOR LATTICE POINT (i, j, k) ON THE kth BLADE

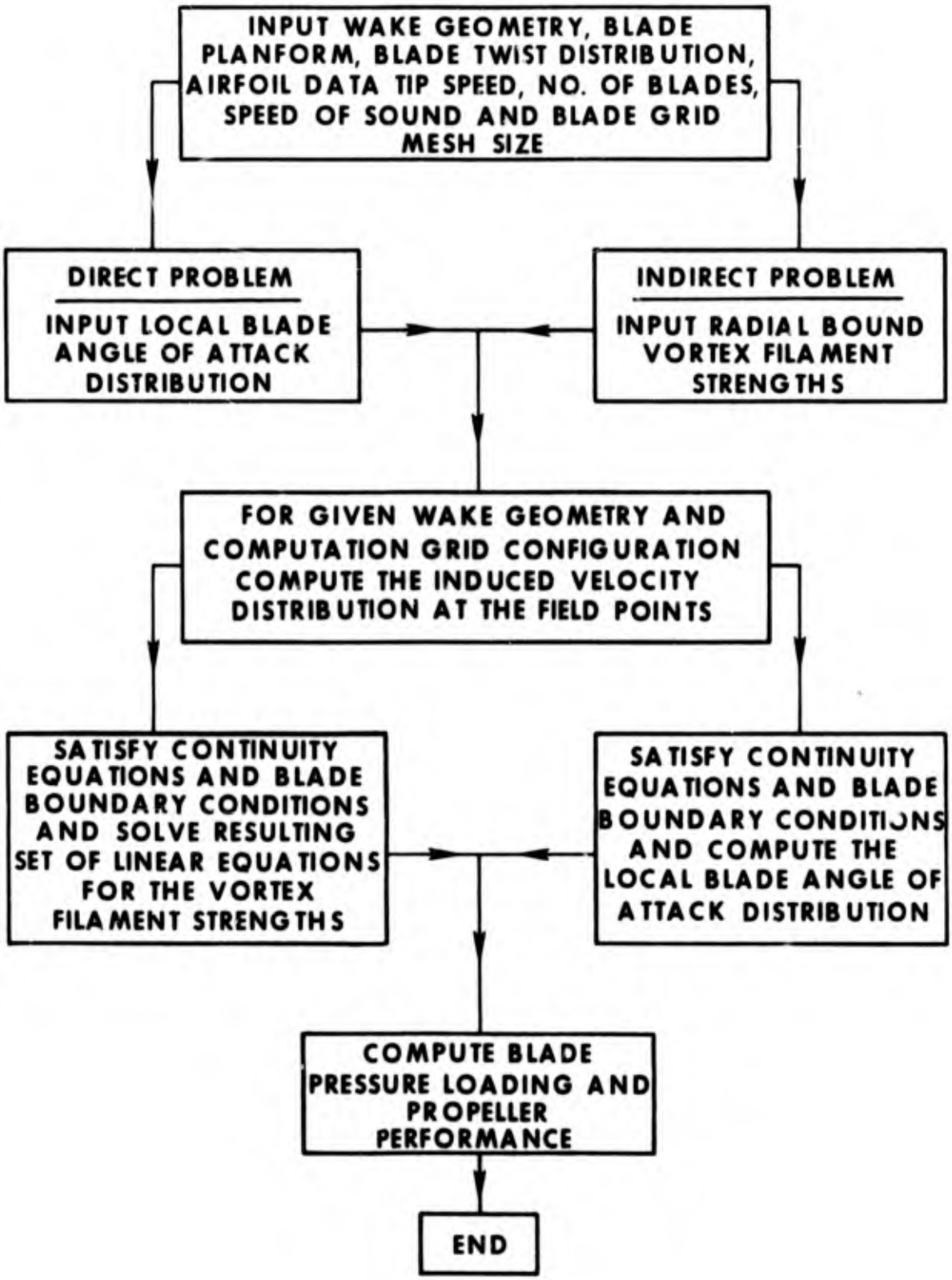

FIGURE 10. FLOW CHART FOR LIFTING SURFACE PROGRAM

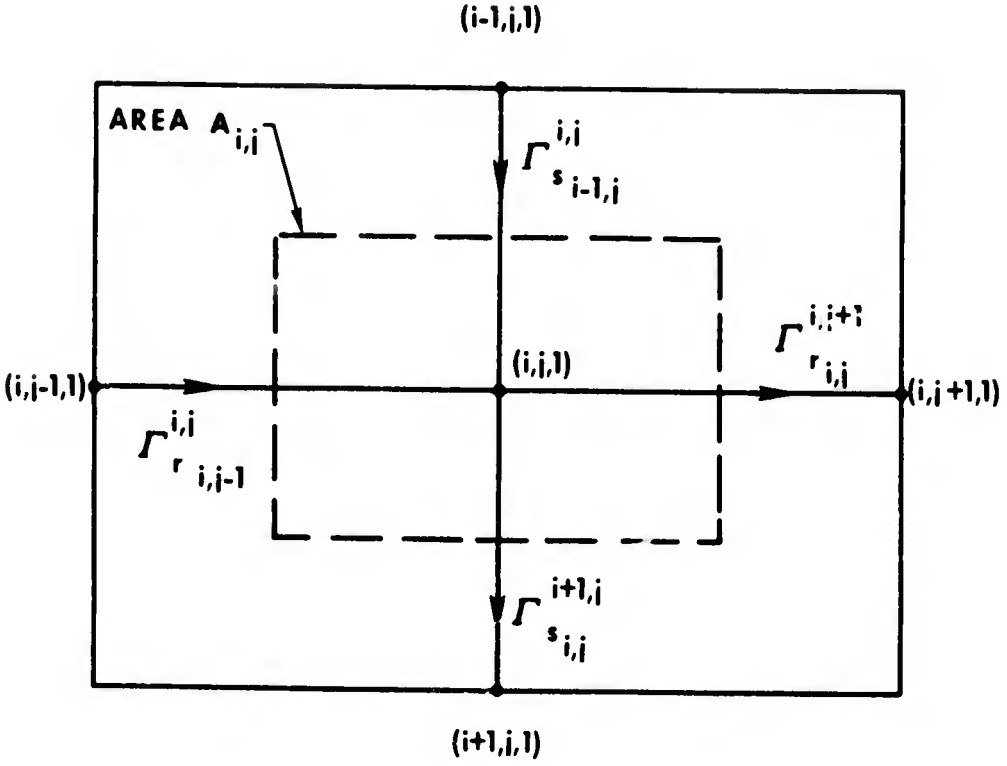

FIGURE 11. INTERIOR LATTICE POINT AND ASSOCIATED AREA FOR PRESSURE LOADING COMPUTATION

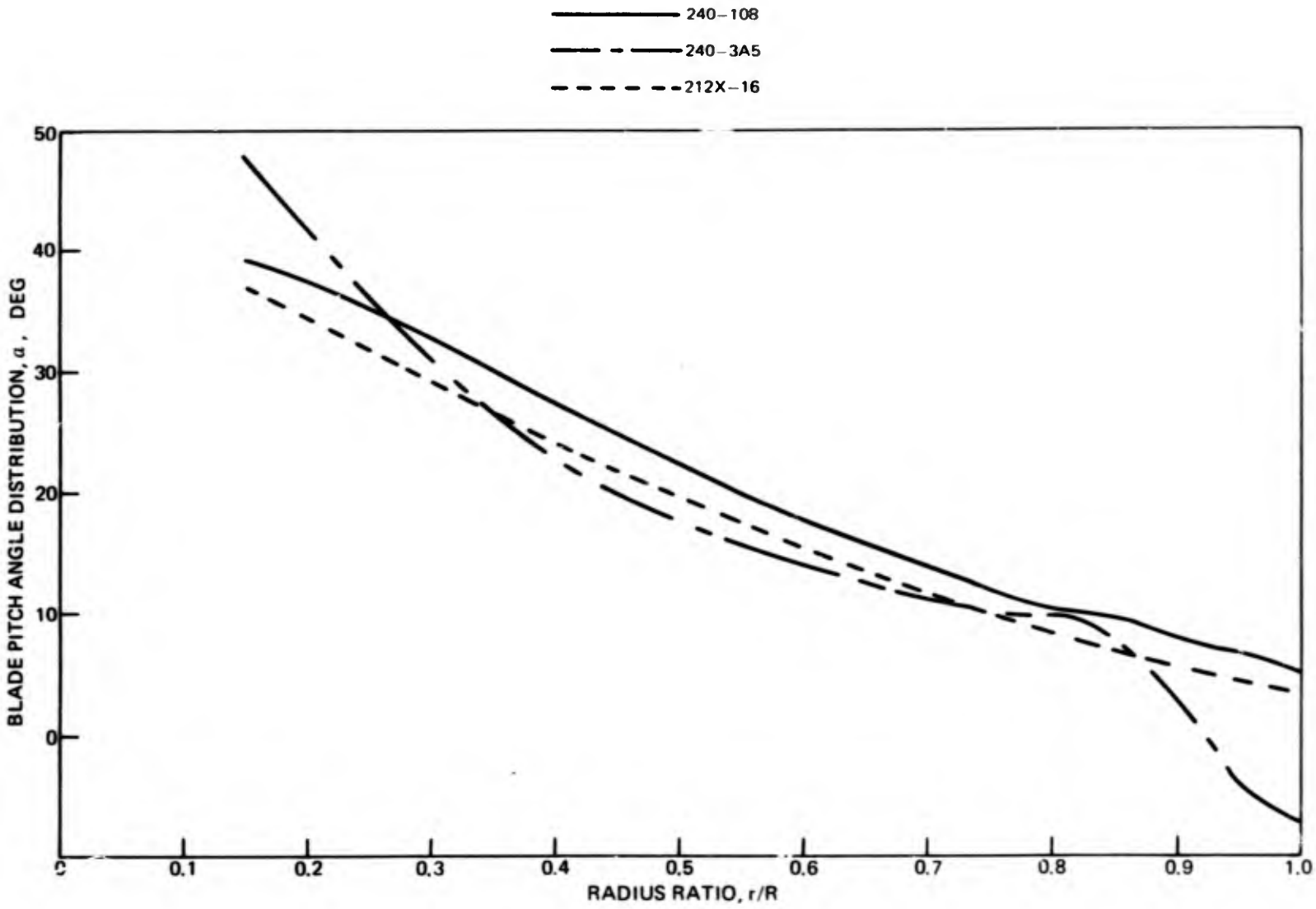

FIGURE 12. BLADE PITCH ANGLE SPANWISE DISTRIBUTION

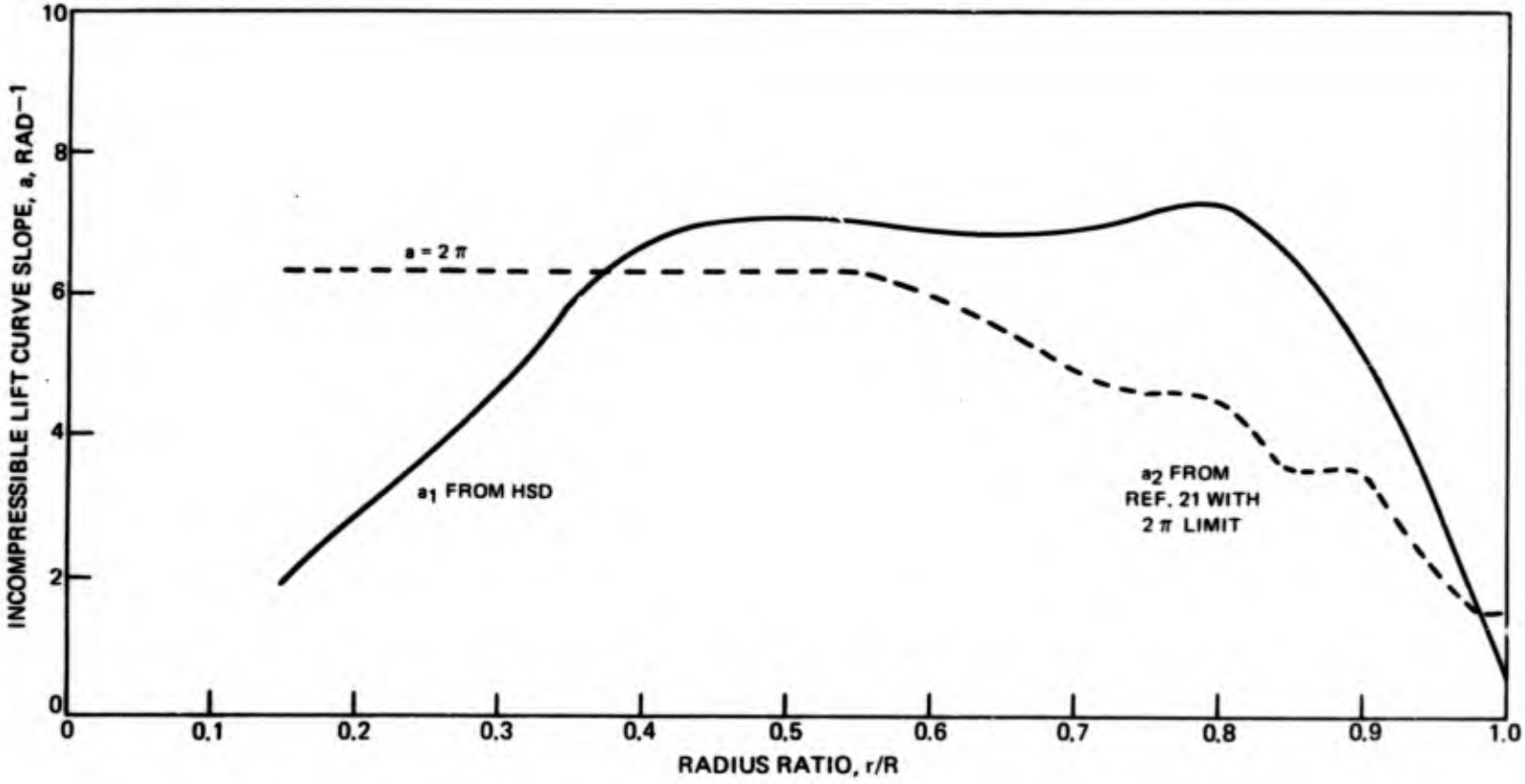

FIGURE 13. INCOMPRESSIBLE LIFT CURVE SLOPE DISTRIBUTION FOR CANADAIR PROPELLER RAA–240–108

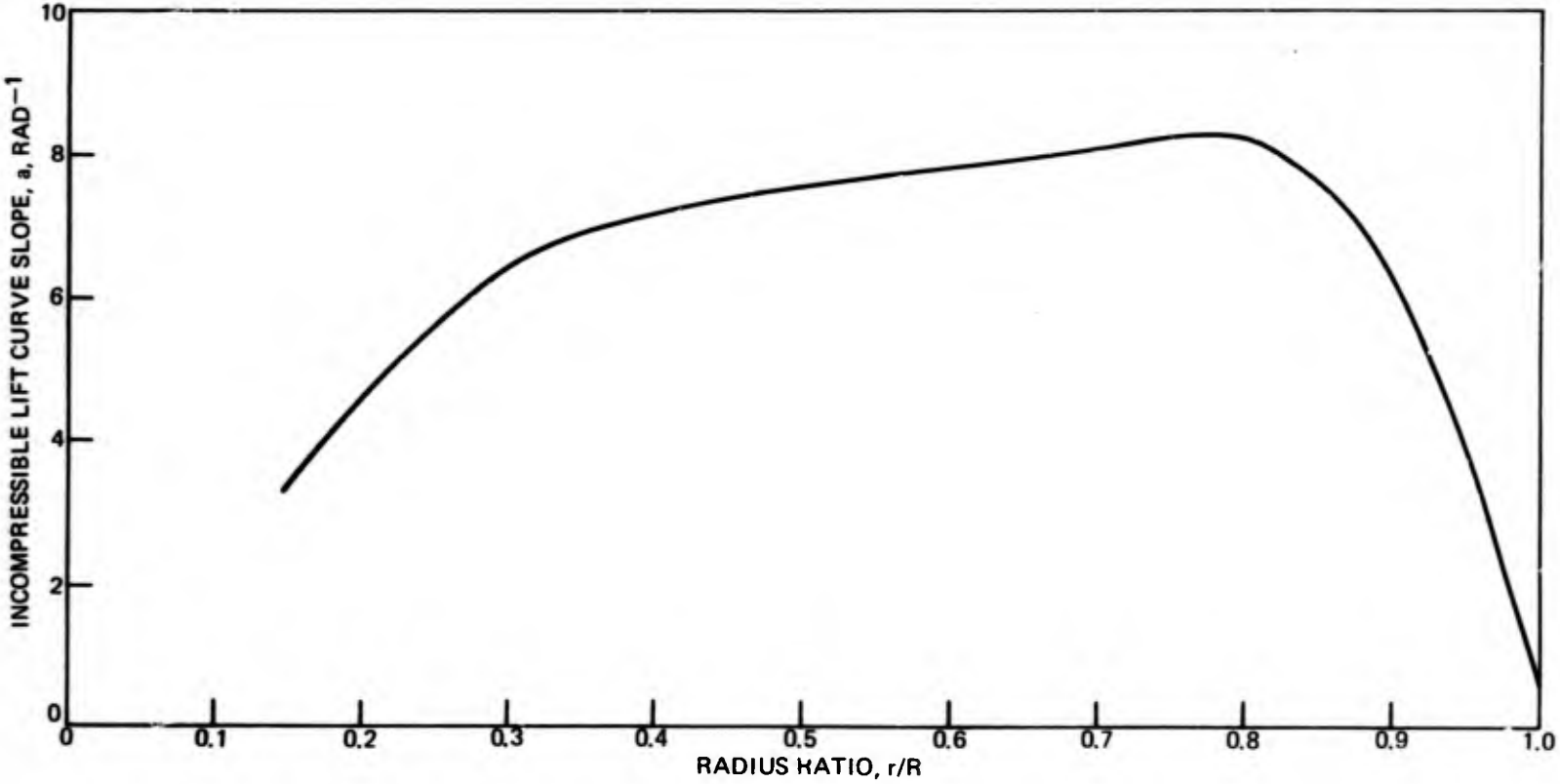

FIGURE 14. INCOMPRESSIBLE LIFT CURVE SLOPE DISTRIBUTION FOR CANADAIR PROPELLER 240–3A5

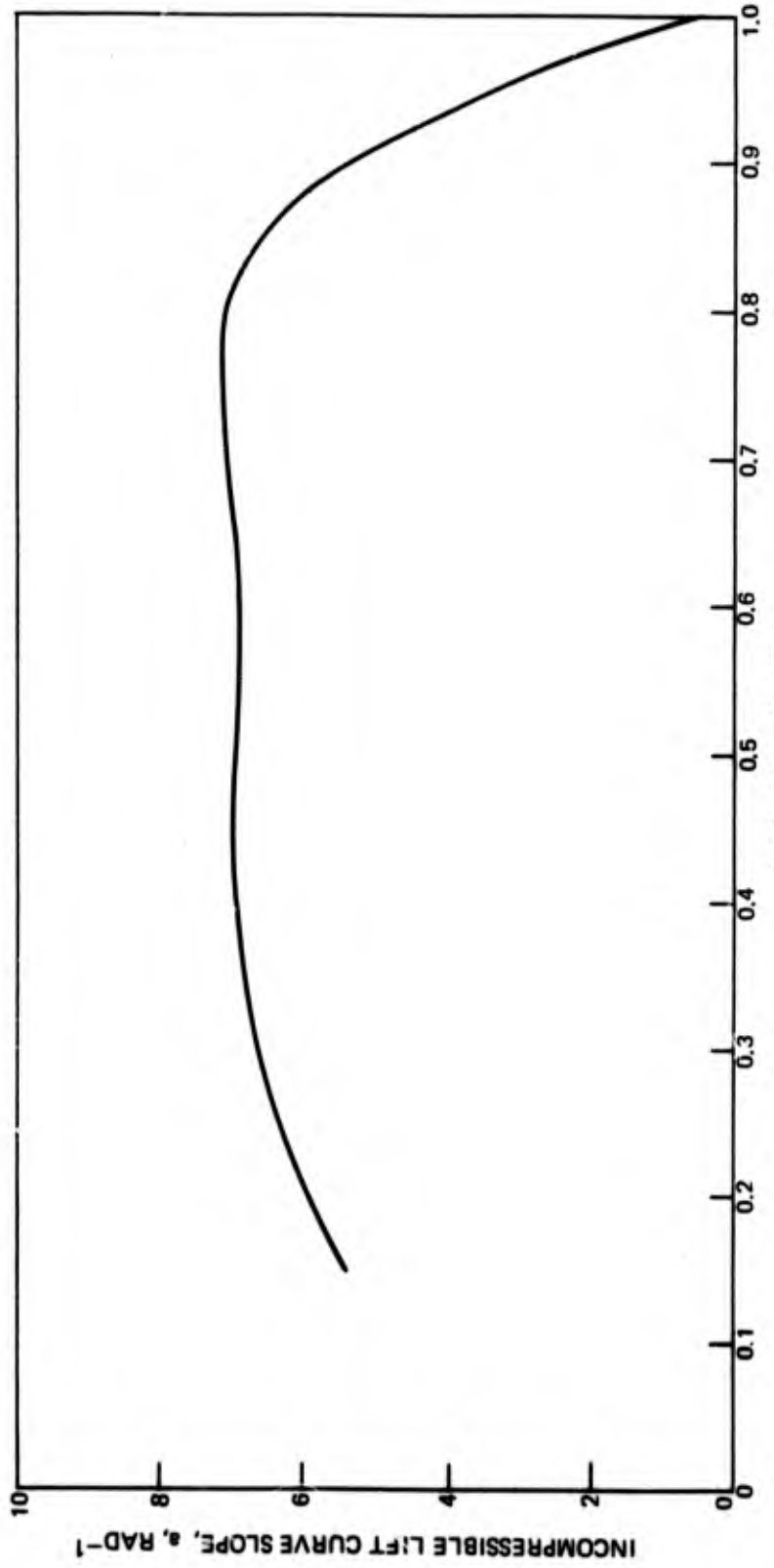

FIGURE 15. INCOMPRESSIBLE LIFT CURVE SLOPE DISTRIBUTION FOR HSD PROPELLER 212X–16

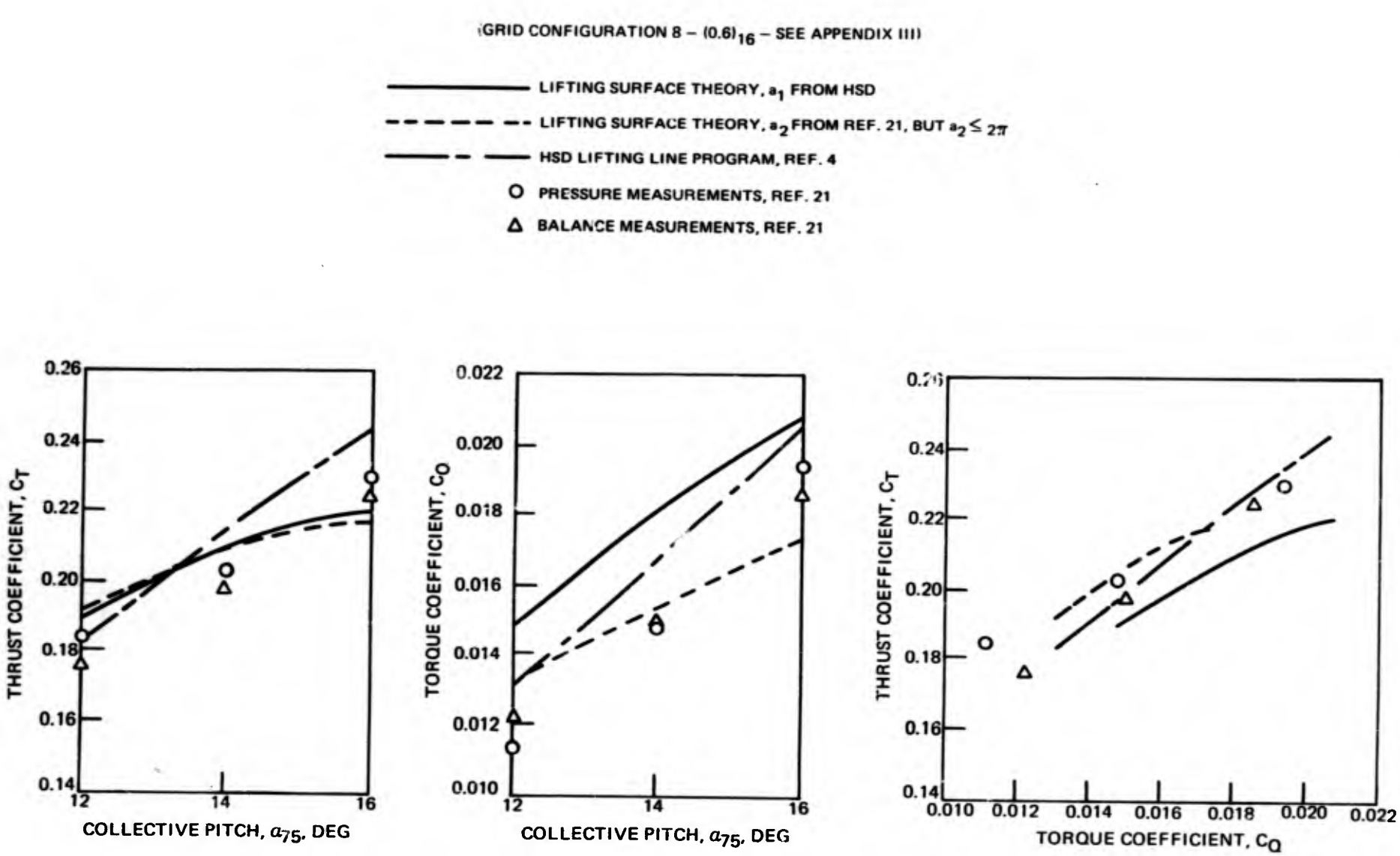

FIGURE 16. PERFORMANCE CALCULATIONS FOR THE CANADAIR RAA–240–108 PROPELLER

(GRID CONFIGURATION 8 – $(0.6)_{16}$ – SEE APPENDIX III)

LIFTING SURFACE THEORY, a FROM HSD

HSD LIFTING LINE PROGRAM, REF. 4

△ BALANCE MEASUREMENTS, REF. 4

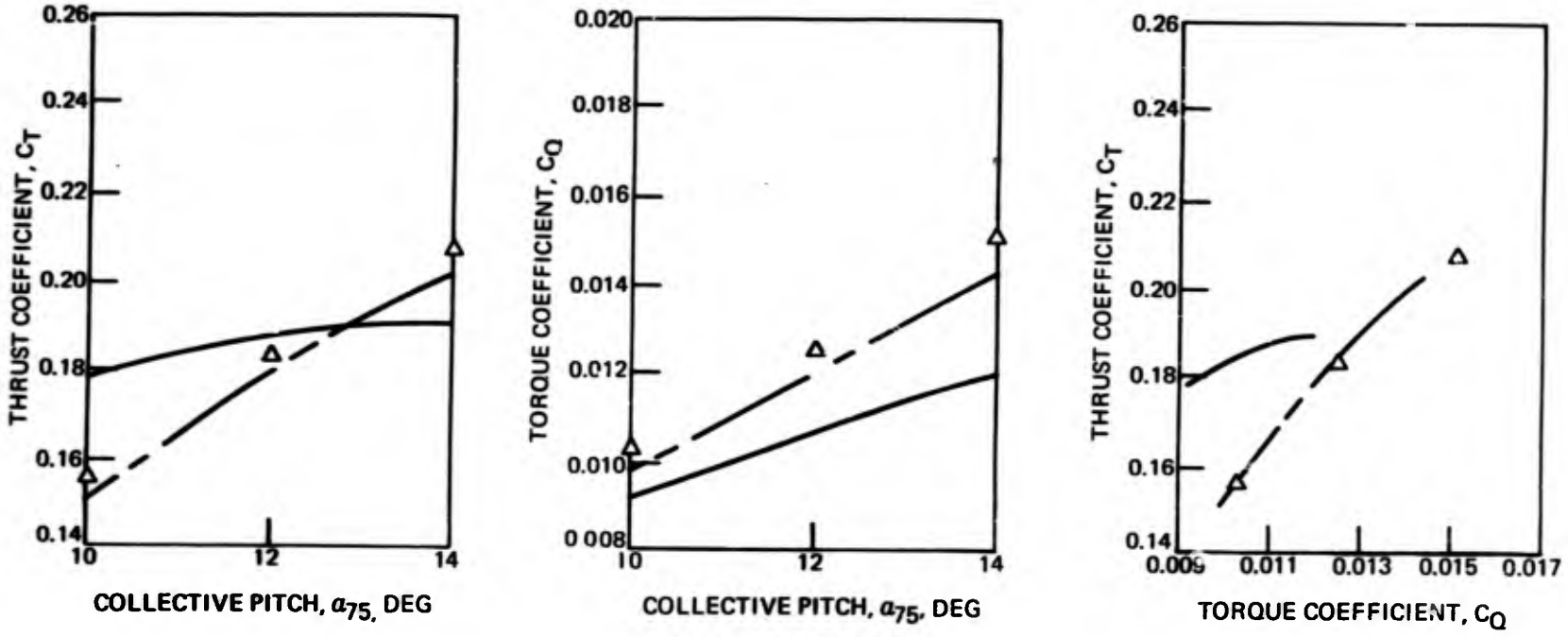

FIGURE 17. PERFORMANCE CALCULATIONS FOR THE CANADAIR 240–3A5 PROPELLER

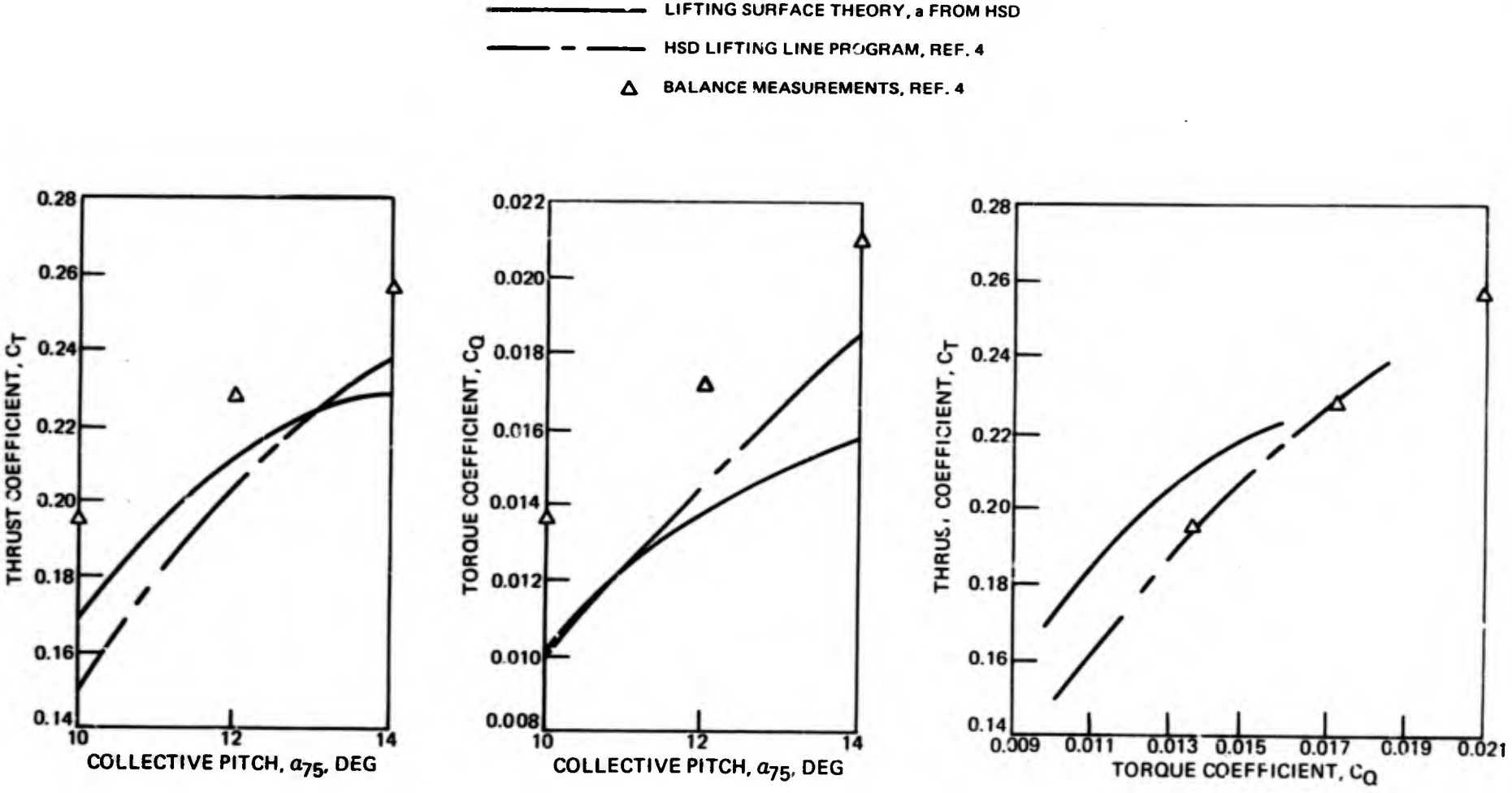

FIGURE 18. PERFORMANCE CALCULATIONS FOR THE HSD 212X–16 PROPELLER

a) LIFT CURVE SLOPE a, FROM HSD

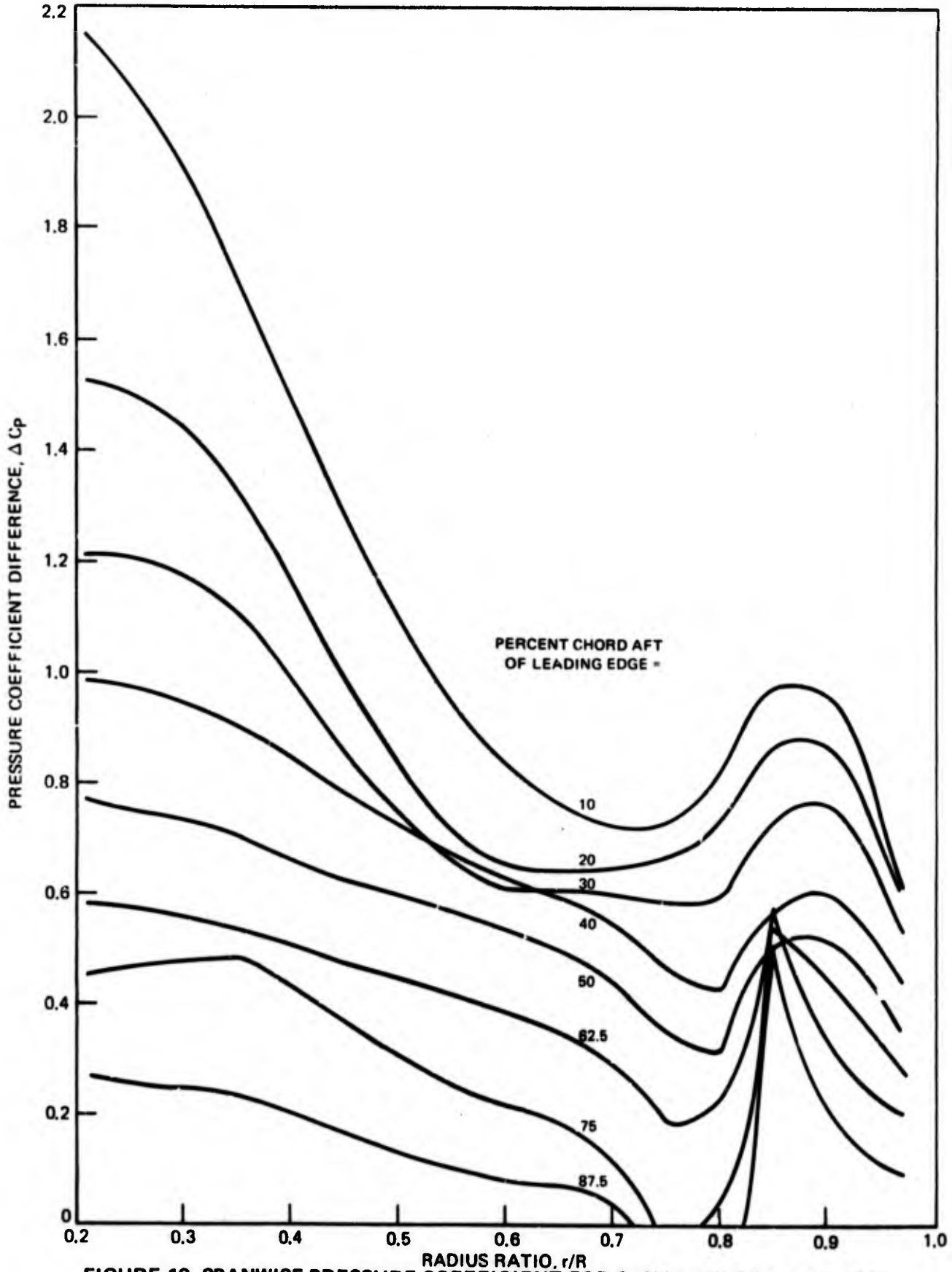

FIGURE 19. SPANWISE PRESSURE COEFFICIENT FOR CANADAIR RAA–240–108 PROPELLER AT α_{75} = 12 DEG

b) LIFT CURVE SLOPE a_2 FROM REF. 21 BUT $a_2 \leq 2\pi$

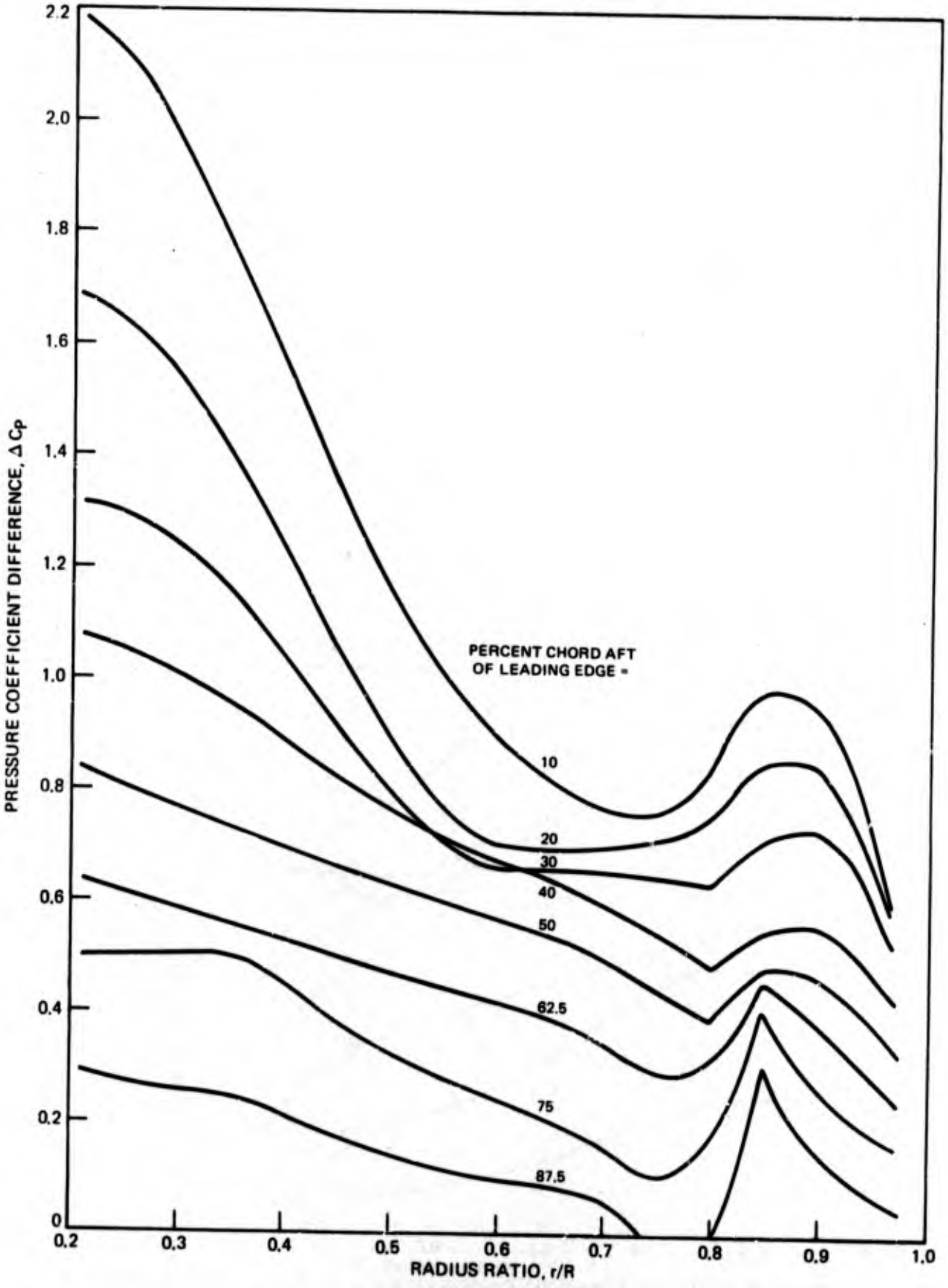

FIGURE 19. CONTINUED

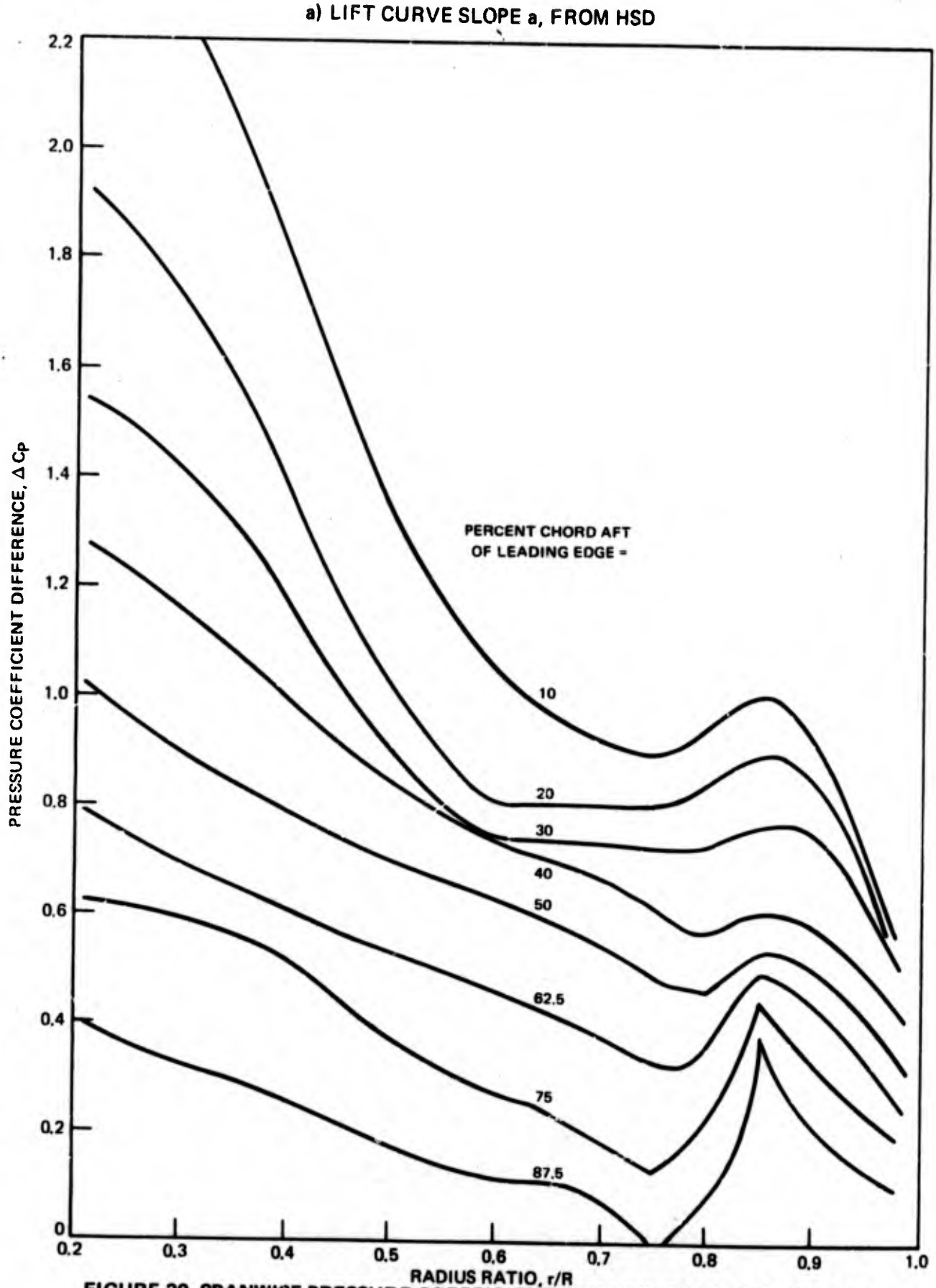

FIGURE 20. SPANWISE PRESSURE COEFFICIENT FOR CANADAIR RAA–240–108 PROPELLER α_{75} = 14 DEG

b) LIFT CURVE SLOPE a_2 FROM REF. 21 BUT $a_2 \leq 2\pi$

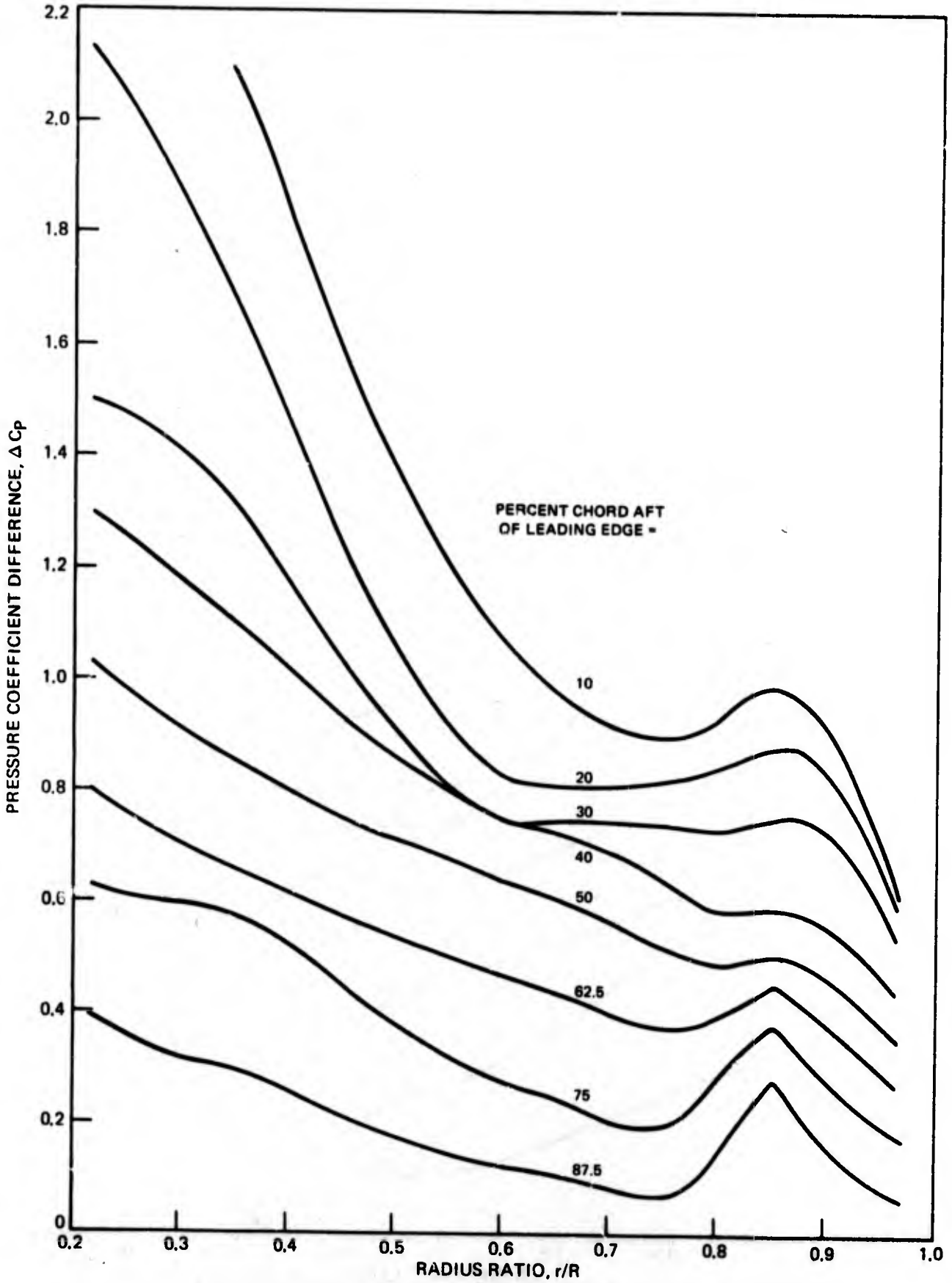

FIGURE 20. CONTINUED

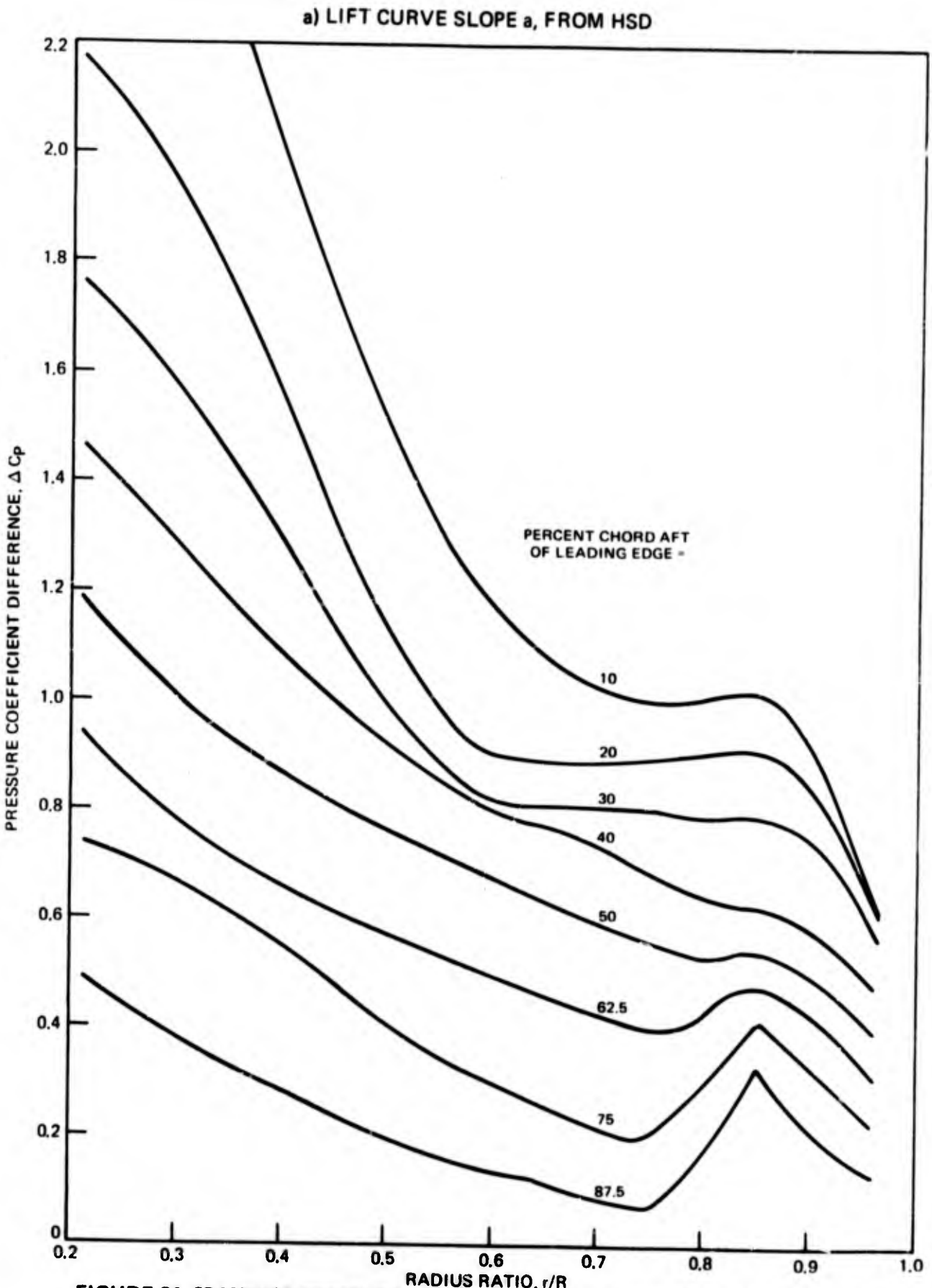

FIGURE 21. SPANWISE PRESSURE COEFFICIENT FOR CANADAIR RAA–240–108 PROPELLER AT α_{75} = 16 DEG

b) LIFT CURVE SLOPE a_2 FROM REF. 21 BUT $a_2 \leq 2\pi$

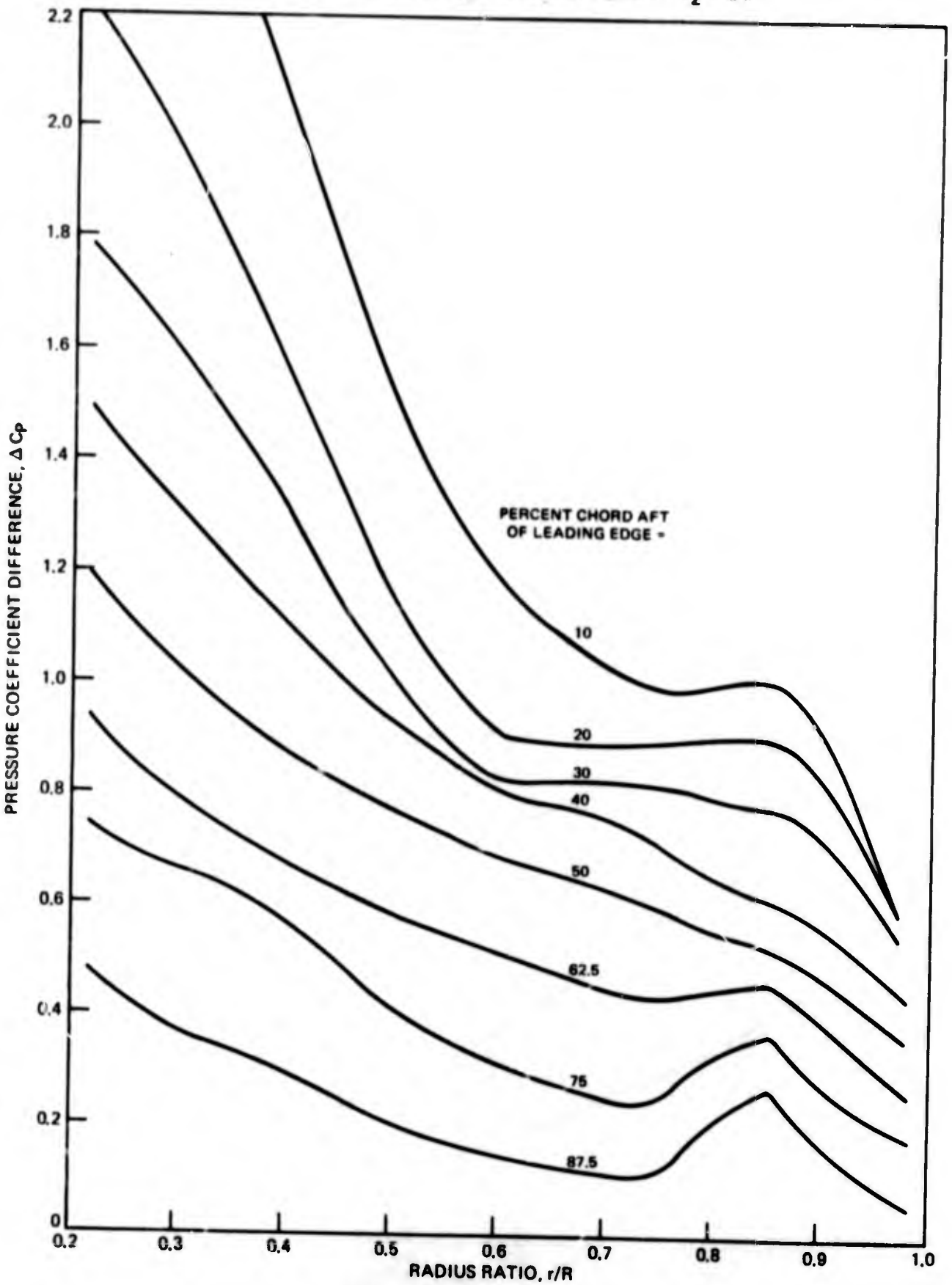

FIGURE 21. CONTINUED

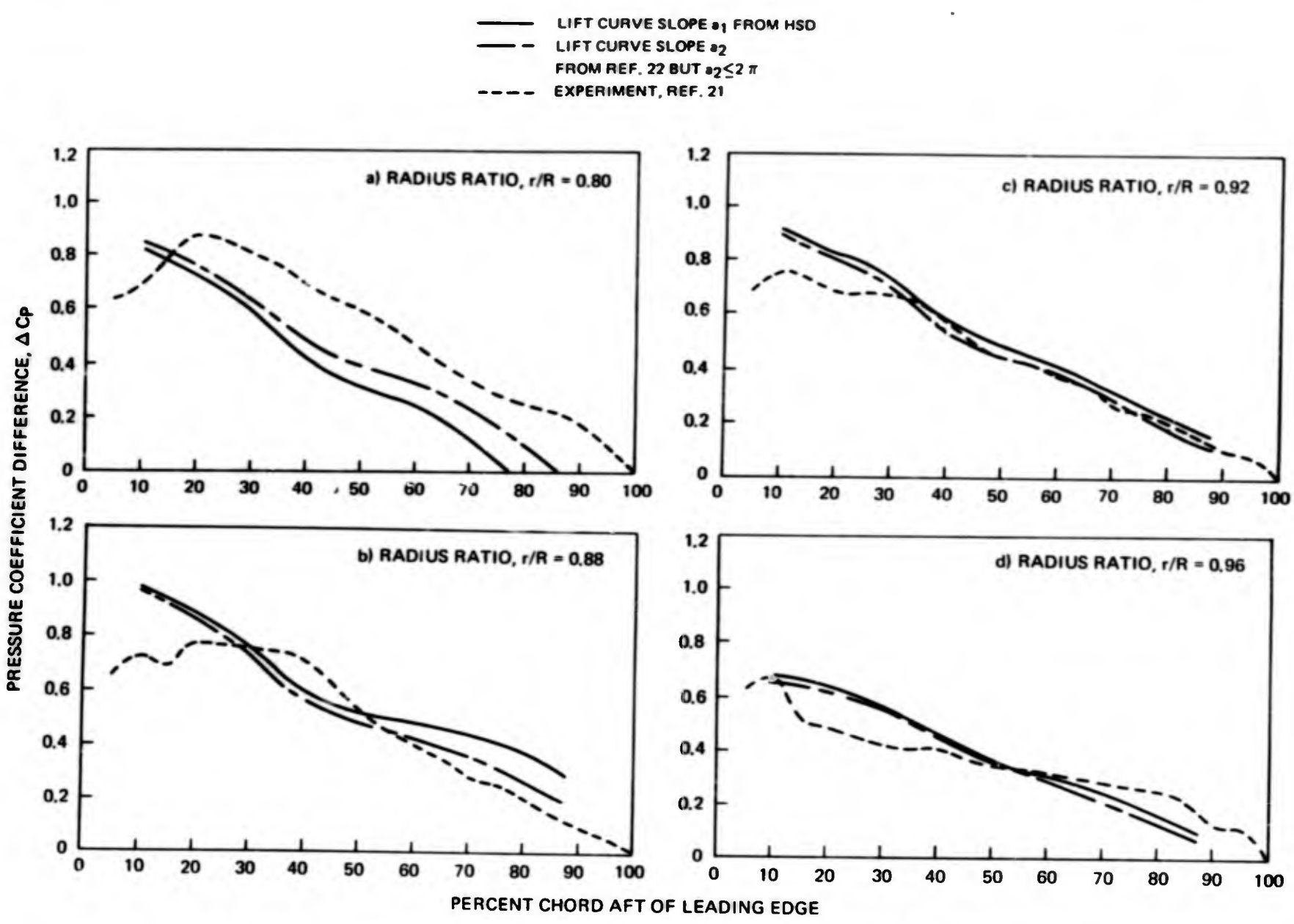

FIGURE 22. CHORDWISE PRESSURE COEFFICIENT FOR CANADAIR RAA–240–108 PROPELLER AT α_{75} = 12 DEG

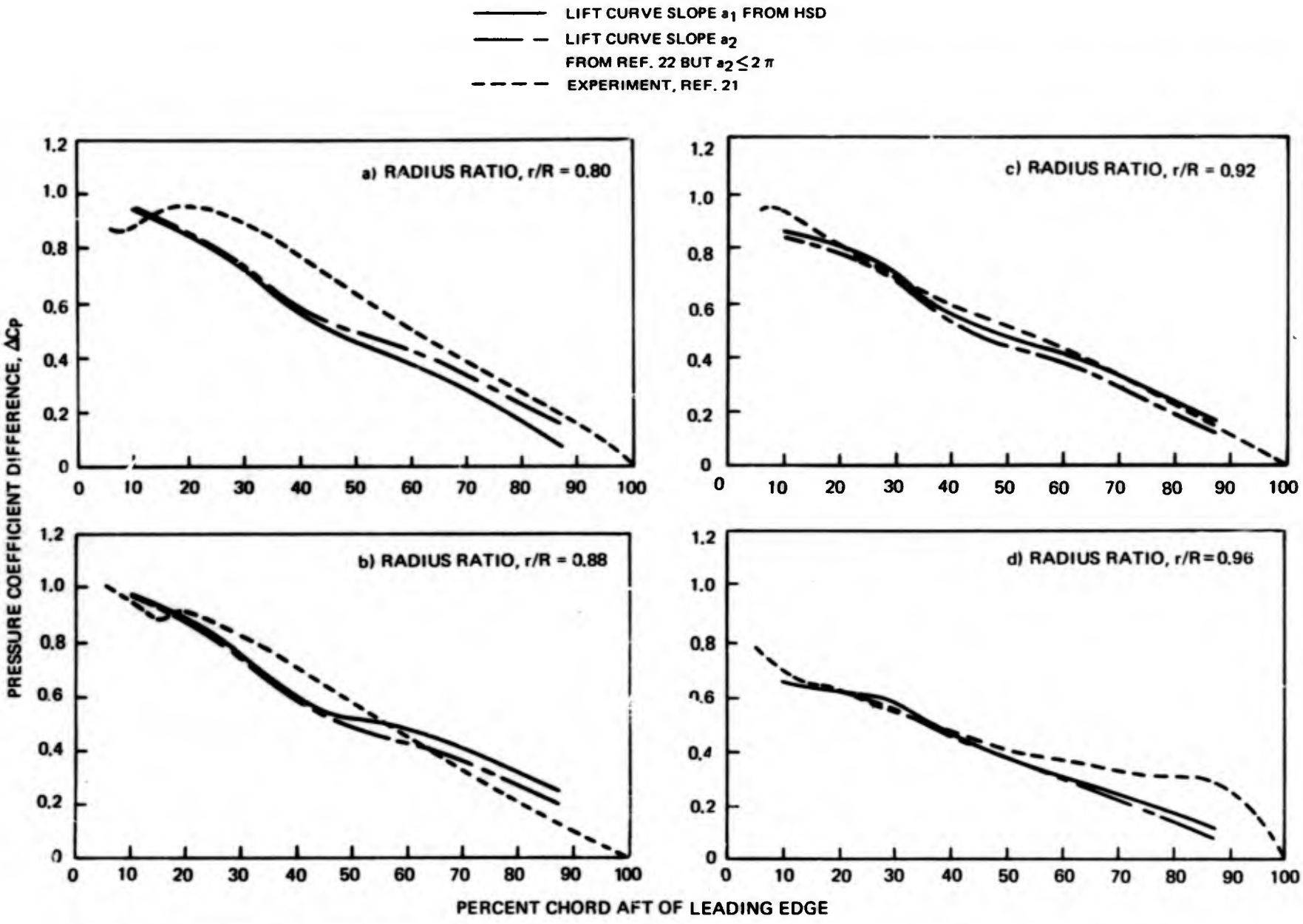

FIGURE 23. CHORDWISE PRESSURE COEFFICIENT FOR CANADAIR RAA–240–108 PROPELLER AT α_{75} = 14 DEG

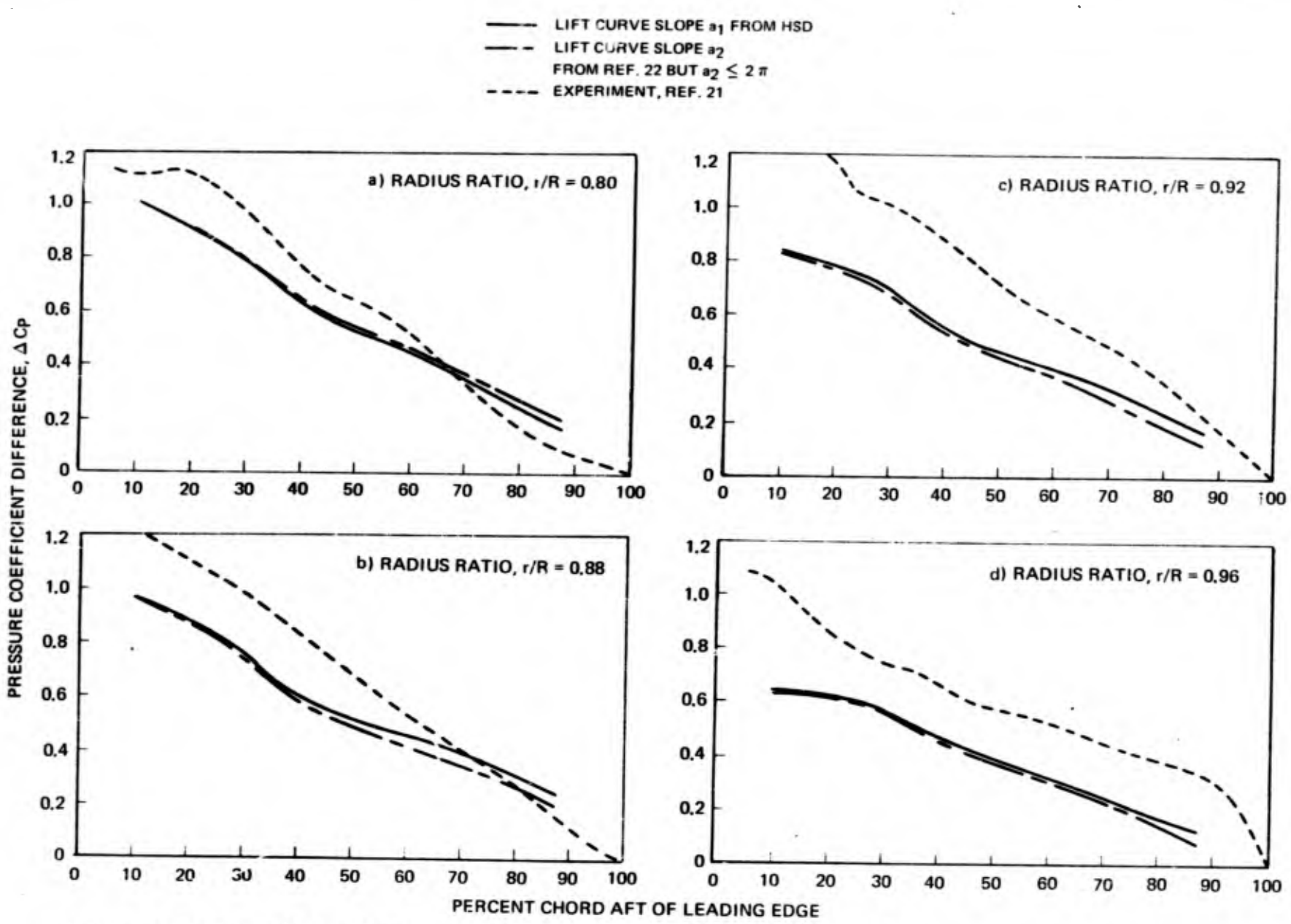

FIGURE 24. CHORDWISE PRESSURE COEFFICIENT FOR CANADAIR RAA–240–108 PROPELLER AT α_{75} = 16 DEG

LIFT CURVE SLOPE a_1 FROM HSD

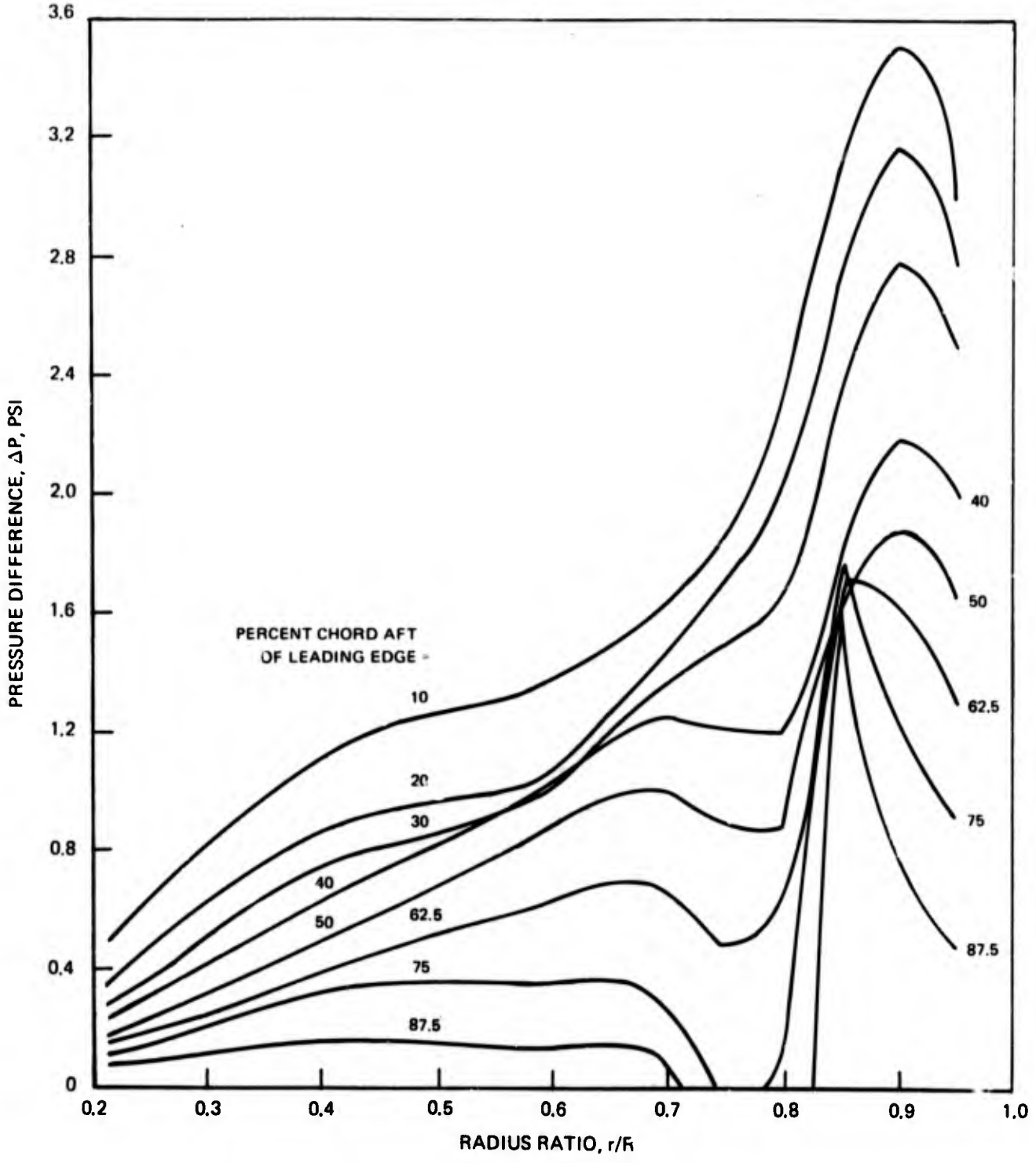

FIGURE 25. SPANWISE PRESSURE DIFFERENCE FOR CANADAIR RAA–240–108 PROPELLER AT α_{75} = 12 DEG

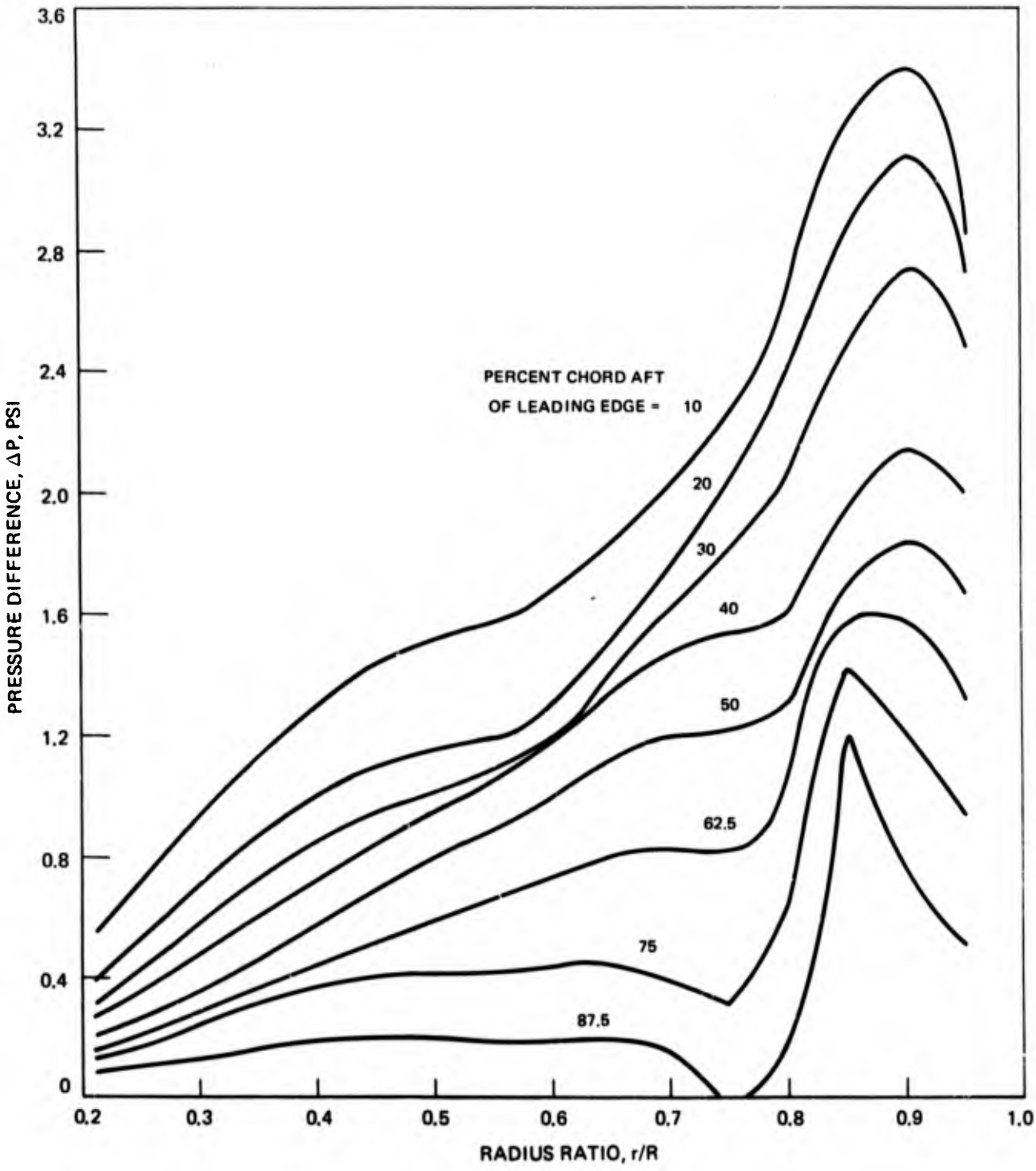

FIGURE 26. SPANWISE PRESSURE DIFFERENCE FOR CANADAIR RAA–240–108 PROPELLER AT α_{75} = 14 DEG

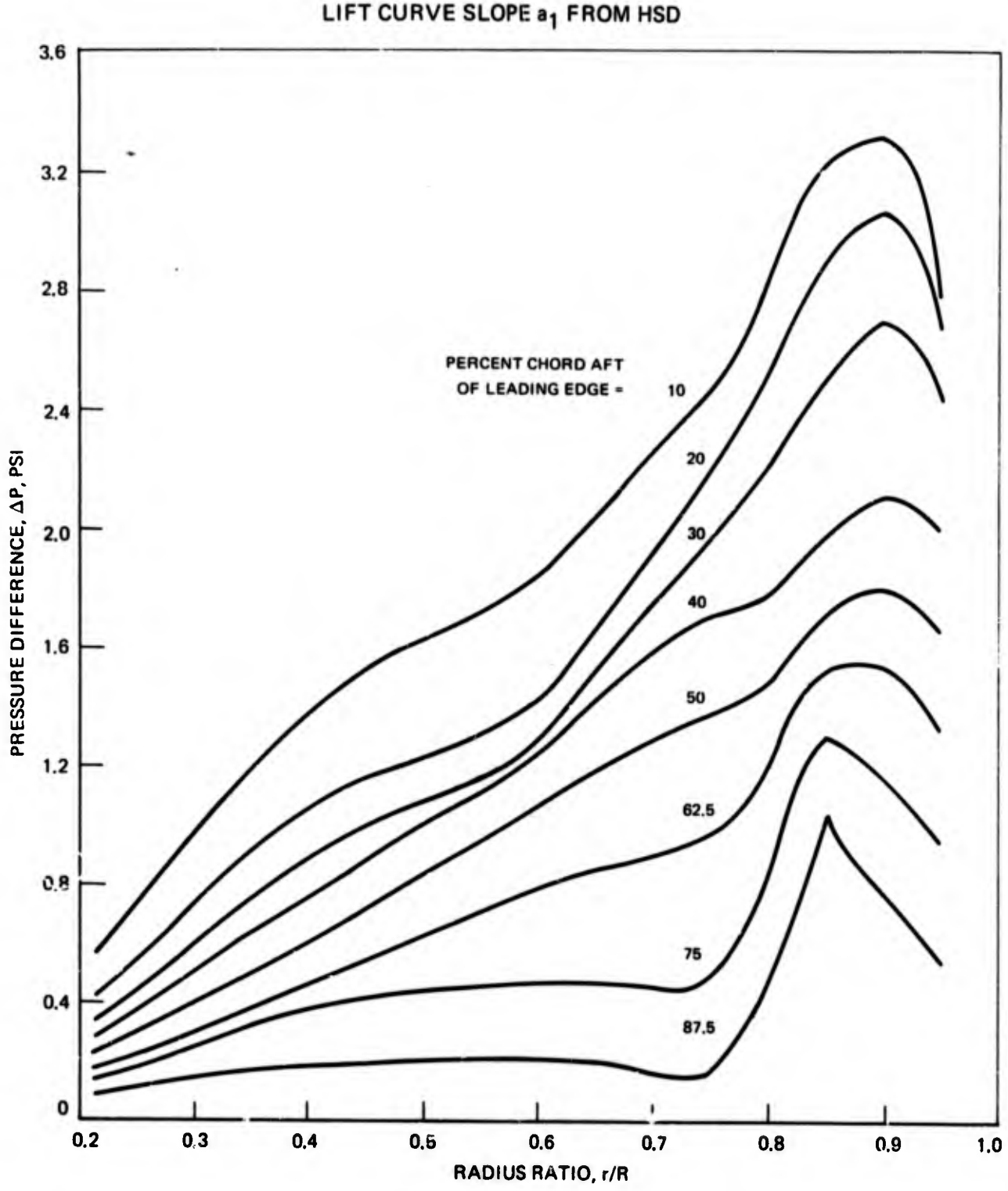

FIGURE 27. SPANWISE PRESSURE DIFFERENCE FOR CANADAIR RAA–240–108 PROPELLER AT α_{75} = 16 DEG

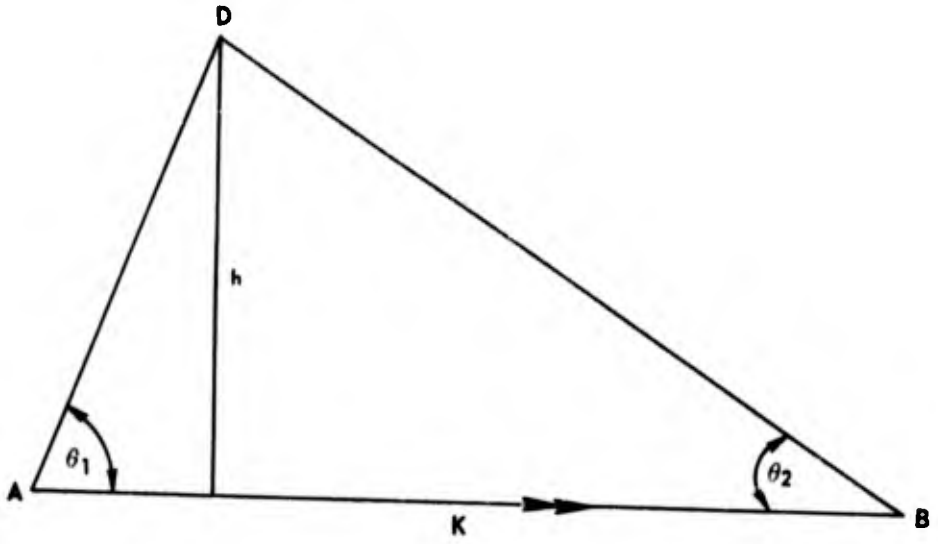

FIGURE 28. VORTEX FILAMENT OF STRENGTH K

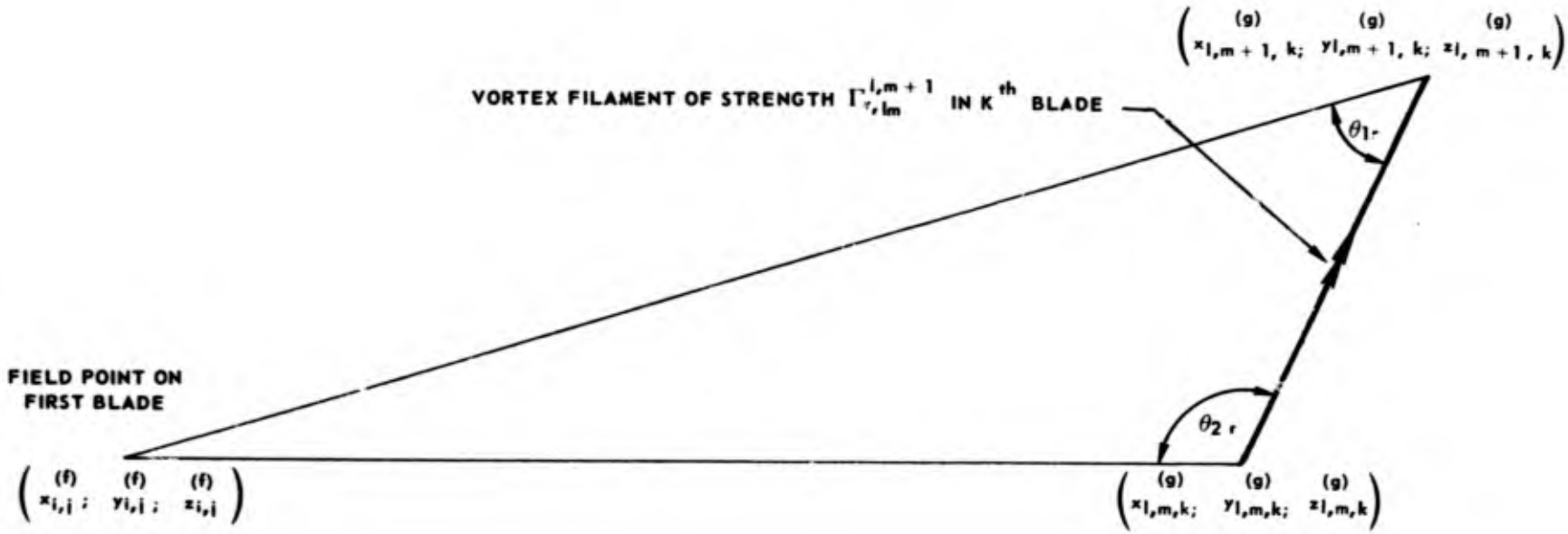

FIGURE 29. GEOMETRY OF VORTEX FILAMENT ON kth BLADE AND FIELD POINT ON FIRST BLADE

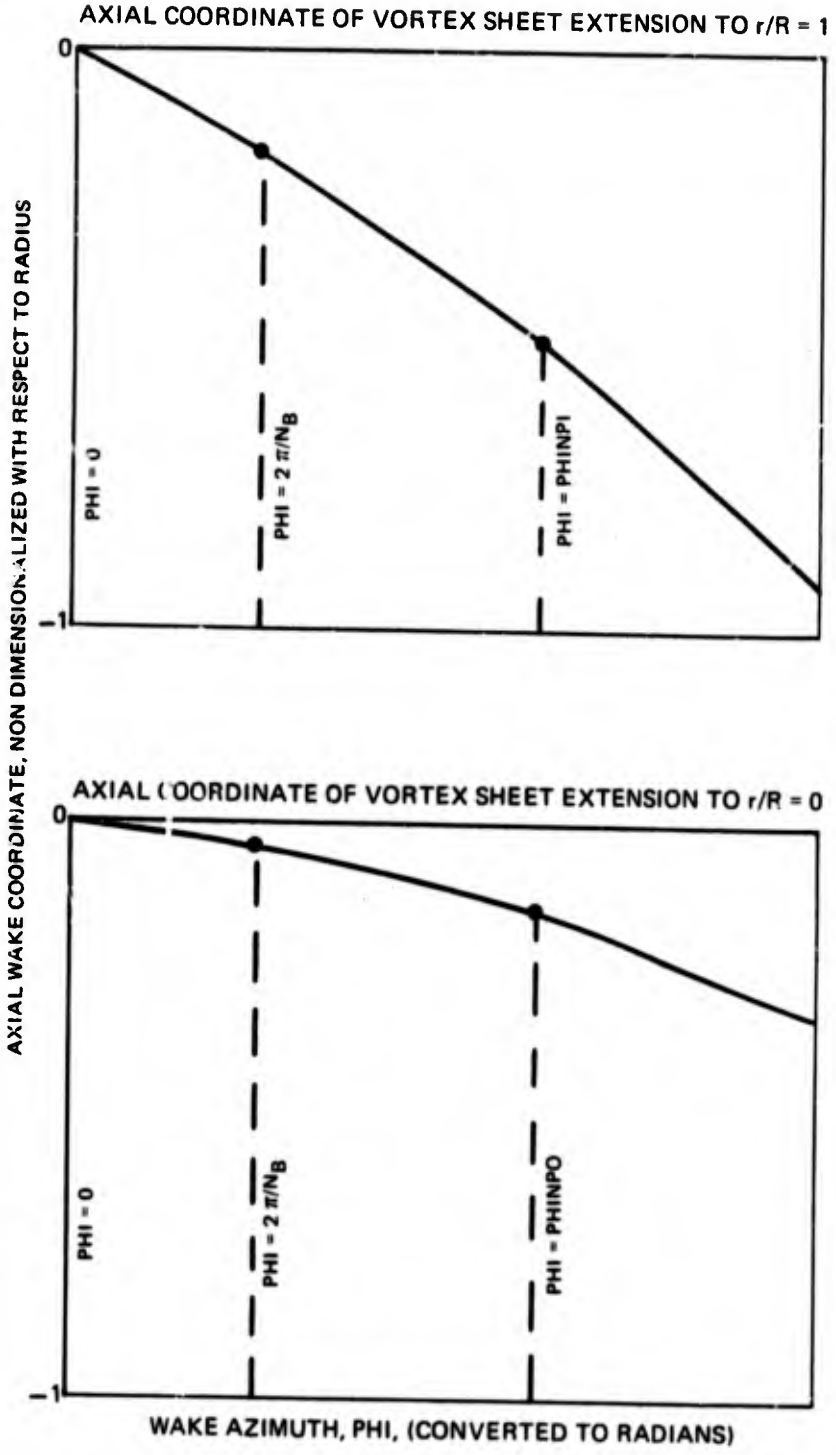

FIGURE 30. VORTEX SHEET PARAMETERS

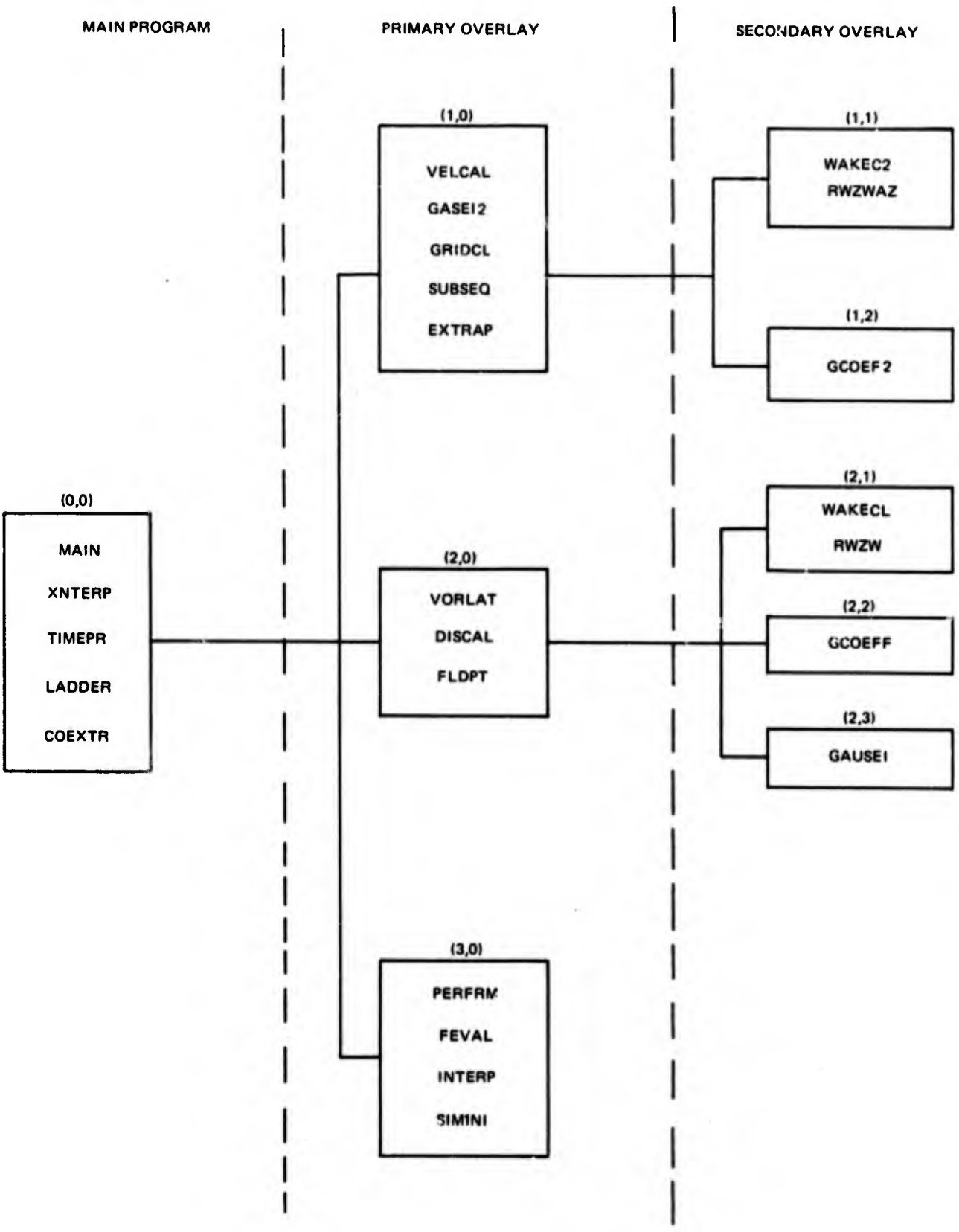

FIGURE 31. COMPUTER PROGRAM OVERLAY SCHEMATIC

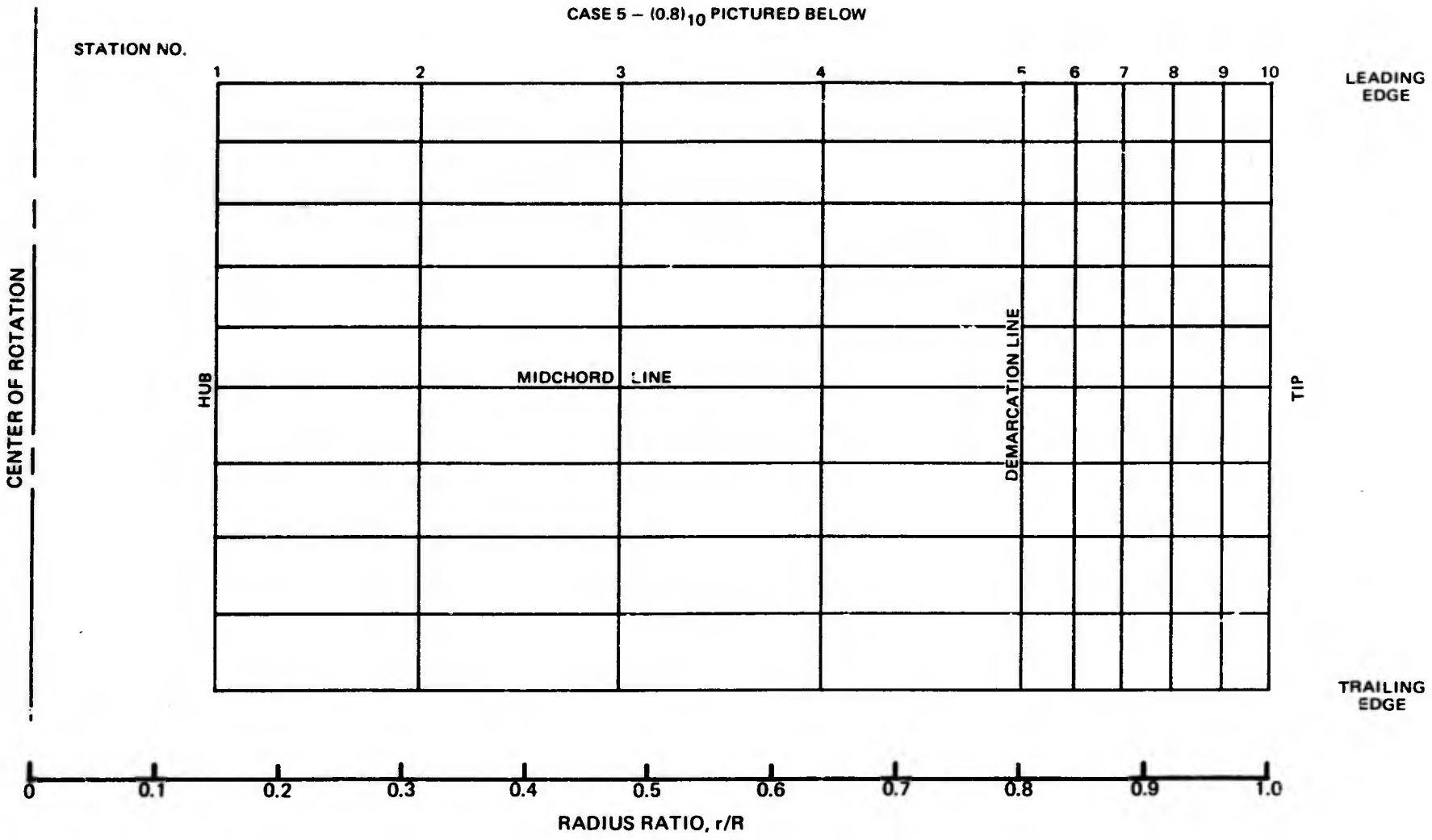

FIGURE 32. PLANFORM GRID NOMENCLATURE

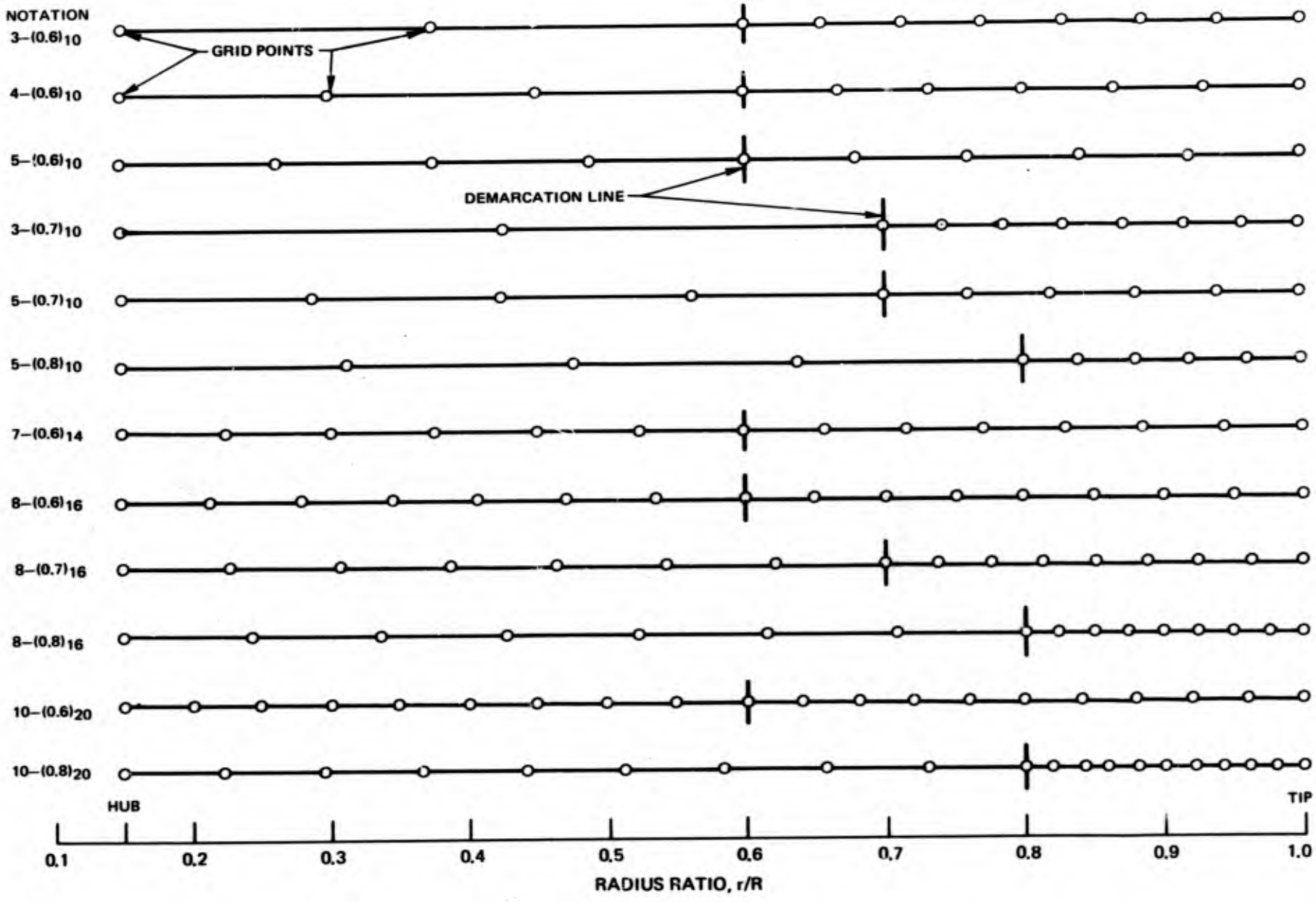

FIGURE 33. SPANWISE GRIDS USED IN SENSITIVITY STUDY

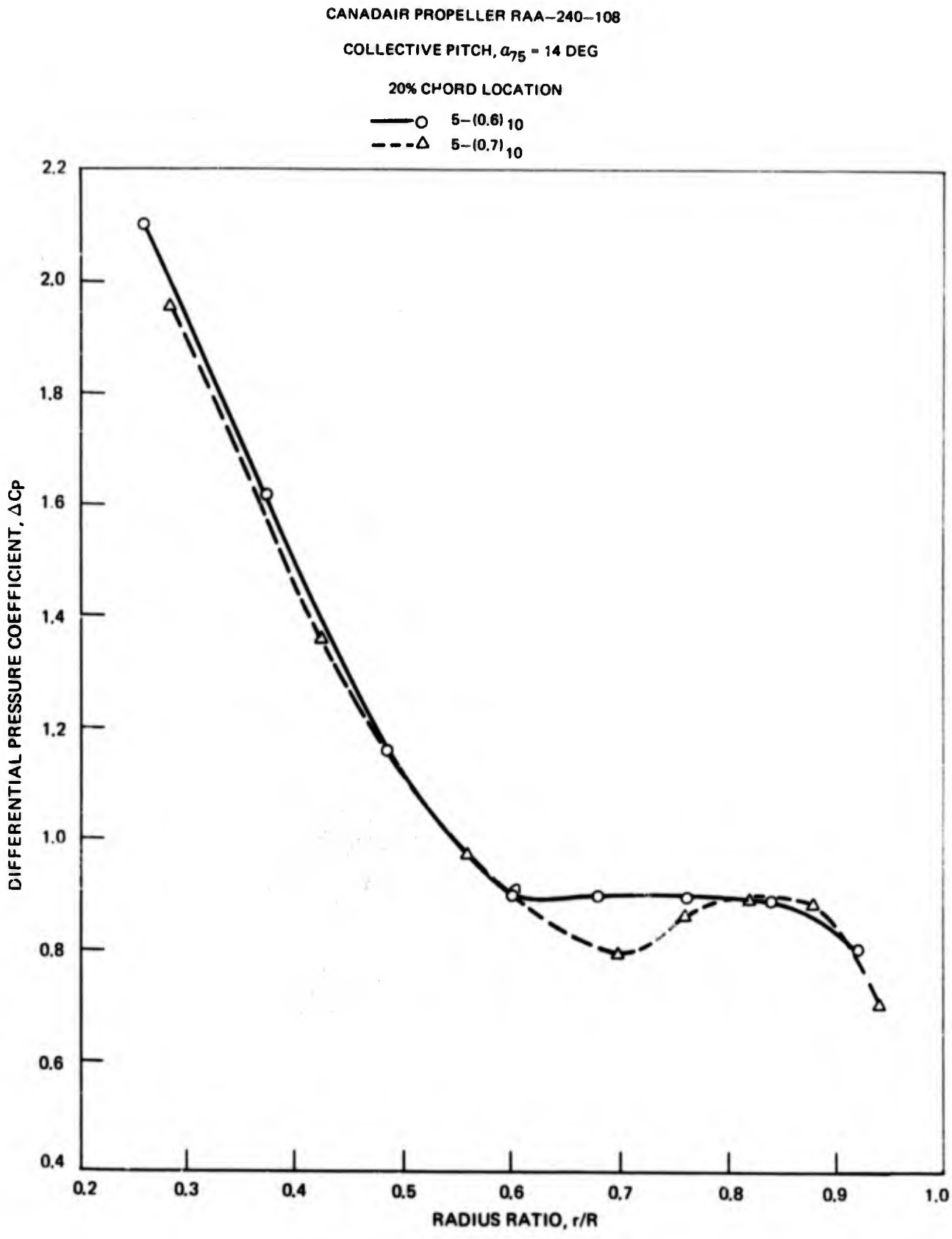

FIGURE 34. EFFECTS OF GRID CHANGES ON SPANWISE PRESSURE DISTRIBUTION

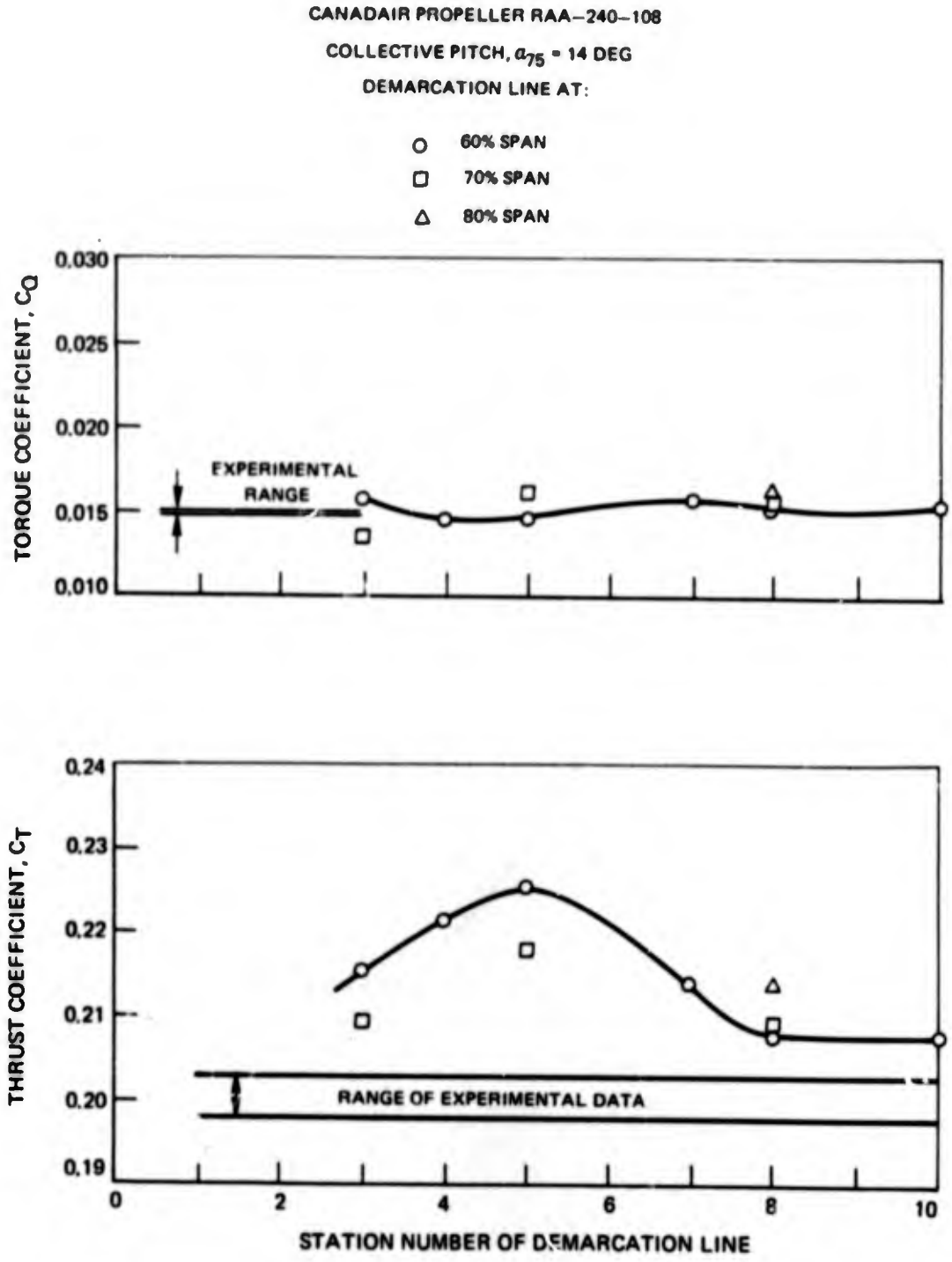

FIGURE 35. EFFECTS OF GRID CHANGES ON INTEGRATED THRUST AND TORQUE

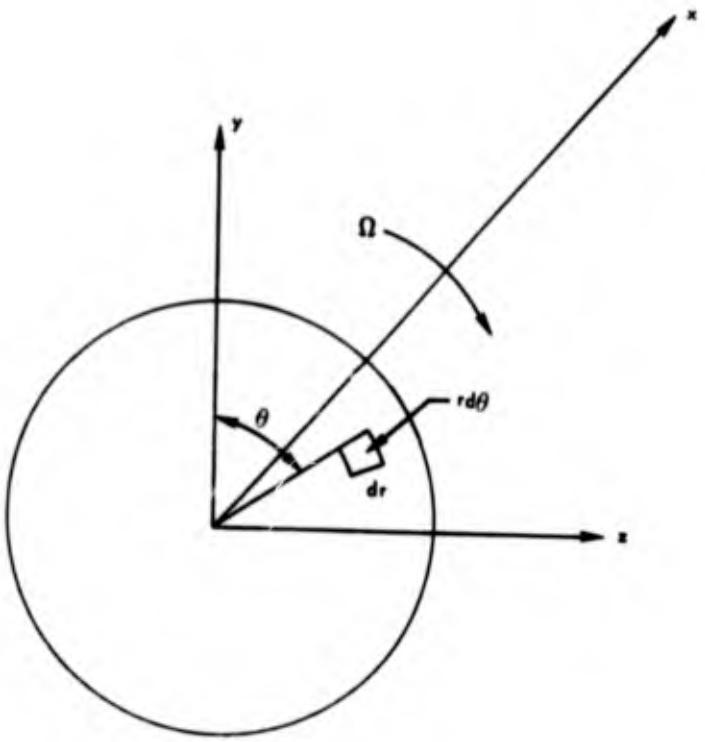

FIGURE 36. PROPELLER DISK AND COORDINATE SYSTEM FOR ACOUSTIC PREDICTION